

The MOPYS project: A survey of 70 planets in search of extended He I and H atmospheres

No evidence of enhanced evaporation in young planets

J. Orell-Miquel^{1,2}, F. Murgas^{1,2}, E. Pallé^{1,2}, M. Mallorquín^{1,2}, M. López-Puertas³, M. Lampón³, J. Sanz-Forcada⁴, L. Nortmann⁵, S. Czesla⁶, E. Nagel⁵, I. Ribas^{7,8}, M. Stangret⁹, J. Livingston^{10,11,12}, E. Knudstrup^{13,14}, S. H. Albrecht¹⁴, I. Carleo^{1,2}, J. A. Caballero⁴, F. Dai^{15,16,17}, E. Esparza-Borges^{1,2}, A. Fukui^{18,1}, K. Heng¹⁹, Th. Henning²⁰, T. Kagetani²¹, F. Lesjak⁵, J. P. de Leon²¹, D. Montes²², G. Morello^{13,1}, N. Narita^{18,10,1}, A. Quirrenbach²³, P. J. Amado³, A. Reiners⁵, A. Schweitzer²⁴, and J. I. Vico Linares²⁵

(Affiliations can be found after the references)

Received 31 January 2024 / Accepted 30 May 2024

ABSTRACT

During the first billion years of their life, exoplanet atmospheres are modified by different atmospheric escape phenomena that can strongly affect the shape and morphology of the exoplanet itself. These processes can be studied with Ly α , H α , and/or He I triplet observations. We present high-resolution spectroscopy observations from CARMENES and GIARPS checking for He I and H α signals in 20 exoplanetary atmospheres: V1298 Tau c, K2-100 b, HD 63433 b, HD 63433 c, HD 73583 b, HD 73583 c, K2-77 b, TOI-2076 b, TOI-2048 b, HD 235088 b, TOI-1807 b, TOI-1136 d, TOI-1268 b, TOI-1683 b, TOI-2018 b, MASCARA-2 b, WASP-189 b, TOI-2046 b, TOI-1431 b, and HAT-P-57 b. We report two new high-resolution spectroscopy He I detections for TOI-1268 b and TOI-2018 b, and a H α detection for TOI-1136 d. Furthermore, we detect hints of He I for HD 63433 b, and H α for HD 73583 b and c, which need to be confirmed. The aim of the Measuring Out-flows in Planets orbiting Young Stars (MOPYS) project is to understand the evaporating phenomena and test their predictions from the current observations. We compiled a list of 70 exoplanets with He I and/or H α observations, from this work and the literature, and we considered the He I and H α results as proxy for atmospheric escape. Our principal results are that 0.1–1 Gyr planets do not exhibit more He I or H α detections than older planets, and evaporation signals are more frequent for planets orbiting ~ 1 –3 Gyr stars. We provide new constraints to the cosmic shoreline, the empirical division between rocky planets and planets with atmosphere, by using the evaporation detections and we explore the capabilities of a new dimensionless parameter, $R_{\text{He}}/R_{\text{Hill}}$, to explain the He I triplet detections. Furthermore, we present a statistically significant upper boundary for the He I triplet detections in the T_{eq} versus ρ_p parameter space. Planets located above that boundary are unlikely to show He I absorption signals.

Key words. techniques: photometric – techniques: spectroscopic – planets and satellites: atmospheres – planets and satellites: gaseous planets – planets and satellites: physical evolution

1. Introduction

NOTE: This accepted version of the manuscript has a different numbering of figures, tables and appendices than the published version. Please refer to the published version for proper referencing.

Along with their stars, planets evolve and change over time. During their early stages of formation, in particular, they undergo severe changes in their physical and orbital properties due to internal and external forces (Baruteau et al. 2016). Exoplanets form embedded in the protoplanetary disc, from where they can accrete H and He, which are the major constituents of their gaseous envelopes (Guenther et al. 2023). Following the disc dispersion in ~ 1 –10 Myr (Haisch et al. 2001; Hernández et al. 2007; Baruteau et al. 2016), different phenomena occur favouring the mass-loss processes in the planetary atmospheres: i) the gas disc dissipates leaving the exoplanet and its H/He-rich atmosphere exposed to the direct radiation of the host star (Fedele et al. 2010; Barenfeld et al. 2016; Dawson & Johnson 2018); ii) stars are more active and have their highest levels of X-ray and extreme ultraviolet (XUV, 1–912 Å) energy irradiation until ~ 100 Myr (Jackson et al. 2012); iii) exoplanets are undergoing

contraction and cooling processes until ~ 1 Gyr (Ginzburg et al. 2016, 2018; Gupta & Schlichting 2020); iv) initial gas envelopes tend to be inflated by internal and external heat, resulting in more extended atmospheres (Sanz-Forcada et al. 2011; Owen & Wu 2016, and references therein); and v) the XUV radiation supports the population of metastable He I (Sanz-Forcada & Dupree 2008). Therefore, at this stage of the system’s evolution the conditions are optimal for detecting the young primordial extended atmospheres.

Photo-evaporation processes are stronger when they are driven by X-ray radiation, which is more significant during the saturated luminosity state (from $\lesssim 100$ Myr until ~ 1 Gyr for late spectral types; Jackson et al. 2012). After this timescale, photo-evaporation is mainly driven, progressively, by the extreme ultraviolet (EUV, 100–912 Å) flux, and its effects on the exoplanet atmosphere are less significant (Sanz-Forcada et al. 2011; Owen & Jackson 2012; Owen & Wu 2013). Furthermore, atmospheric escape can also be driven by the heat released from the cooling core of the planet. This mechanism, called core-powered evaporation, plays an important role, and this process can act approximately on gigayear timescales (Ginzburg et al. 2016, 2018; Gupta & Schlichting 2020).

Both escape mechanisms have some overlap in time and may act simultaneously in shaping the final atmosphere of mature exoplanets. In this context, the study of planets at the early stages of evolution is crucial for a better comprehension of the different processes, and to prove theory predictions, such as planet formation and migration, giant planets' gas accretion, or escape of the primary atmospheres of rocky-core planets with gas envelopes (e.g. Baruteau et al. 2016; Owen & Wu 2017; Dawson & Johnson 2018). In particular, core-powered and photo-evaporation processes have been suggested to explain the formation of the radius gap in the small ($1-4 R_{\oplus}$) planets radius distribution (e.g. Fulton et al. 2017; Fulton & Petigura 2018; Van Eylen et al. 2018, 2021), although formation and migration mechanisms have also been proposed to explain the valley (Luque & Pallé 2022).

Exoplanets can also experience atmospheric mass loss during their later lifetime because photo-evaporation and core-powered mechanisms can act at longer timescales than $\sim 0.1-1$ Gyr, but at reduced total mass-loss rates (Sanz-Forcada et al. 2011; Owen & Jackson 2012). According to stellar and planetary evolution models and assuming that high mass-loss rates are easier to detect, the number of evaporation detections should be higher in the <100 Myr period, where the X-ray photo-evaporation and core-powered mechanisms act together (Sanz-Forcada et al. 2011; Owen & Wu 2013; Ginzburg et al. 2016). After ~ 1 Gyr, the number of detections should decrease as the core-powered atmospheric escape is weakening during the first few gigayears (Ginzburg et al. 2016, 2018). As a rough approximation, we should expect a plateau of atmospheric mass-loss detections after the approximately gigayear timescale. At the time photo-evaporation is mainly driven by the EUV flux (Sanz-Forcada et al. 2011), the planet properties are already fixed. For gas giants and Jupiter-mass planets, the impact of this late-evaporation on the planet mass is close to null (Owen & Wu 2013), while for low-mass planets only small changes in their masses are expected (Lopez et al. 2012; Owen & Jackson 2012; Owen & Wu 2013). Therefore, the detection of hydrodynamic escape in old planets (≥ 1 Gyr) may not imply a significant change in their total mass and it may have no evolutionary consequences. Hydrodynamic escape by Roche lobe overflow can be considered an exception (see e.g. Koskinen et al. 2022). The middle atmosphere of extremely close-in planets (with orbital periods of ≤ 1 d) extends to the Roche lobe due to the stellar gravitational tide, producing a very strong atmospheric mass-loss rate. The Roche lobe mechanism can be assumed stellar-age independent, and may not introduce a detectable change in the number of detections across stellar age.

The study of atmospheric escape in exoplanet atmospheres is mainly performed with the observations of three evaporation tracers: the H Lyman- α line ($Ly\alpha$) at 1216 \AA at ultraviolet (UV) wavelengths, the H Balmer- α line ($H\alpha$) at 6564 \AA at optical wavelengths, and the He I triplet at 10833 \AA at near-infrared (NIR) wavelengths. All the wavelengths in this work are referenced in a vacuum.

The $Ly\alpha$ was the first line used for probing evaporating atmospheres, when Vidal-Madjar et al. (2003) detected its absorption in the upper atmosphere of HD 209458 b. However, the $Ly\alpha$ line has some limitations. First, UV observations cannot be carried out from ground-based facilities, relegating its study to space observations with the *Hubble Space Telescope* (HST) instrument Space Telescope Imaging Spectrograph (STIS). Second, $Ly\alpha$ is strongly affected by the interstellar medium extinction, limiting its observation to only the closest stars, due to their large relative motions. Finally, the H in the upper layers of Earth's atmosphere

(geocorona) have $Ly\alpha$ emission. In practice, the core of the $Ly\alpha$ line cannot be observed, and only the broad wings of the line are accessible. This has led to a very limited number of planetary atmospheres being accessible to $Ly\alpha$ observations.

The $H\alpha$ line was used by Yan & Henning (2018) to prove the evaporation of KELT-9 b's atmosphere. The core and wings of this optical line can be observed from space, but also from ground-based facilities, allowing line profile characterisation when high-resolution spectrographs are used. However, the $H\alpha$ line has some caveats as well: relatively low mass-loss rates can produce large $Ly\alpha$ absorption signals, while remaining undetected in $H\alpha$ (e.g. GJ 436 b, Kulow et al. 2014; Ehrenreich et al. 2015; Cauley et al. 2017); stellar lines in the visible are more sensitive to stellar activity than those in the NIR (e.g. H Paschen lines and He I triplet), making their analysis very challenging in the presence of such activity (Fuhrmeister et al. 2020; Palle et al. 2020b; Howard et al. 2023).

The He I triplet was proposed by Seager & Sasselov (2000), and later modelled by Oklopčić & Hirata (2018), as an alternative to search for evidence of atmospheric escape in the NIR. The first detections came almost simultaneously from ground- and space-based observations (Spake et al. 2018; Nortmann et al. 2018; Allart et al. 2018). Moreover, ground-based high-resolution spectroscopy observations allowed several physical parameters to be retrieved from line profile fitting (Lampón et al. 2020, 2021b,a, 2023). Since stellar lines in the NIR are less sensitive to stellar activity (but not exempted from it; e.g. Spake et al. 2018; Salz et al. 2018) than the optical lines, the He I triplet is a good tracer to explore young exoplanet atmospheres.

Unfortunately, the He I triplet has some disadvantages too. First, there are telluric absorption and emission lines surrounding the NIR triplet wavelengths that can overlap with the planet signal depending on the observing epoch. Second, the He I ionisation wavelength cutoff ($\lambda \leq 504 \text{ \AA}$) is lower than that of H I ($\lambda \leq 912 \text{ \AA}$). Finally, the lifetime of the helium metastable state is ~ 2.2 h (Drake 1971), and a strong and constant XUV irradiation is needed to maintain the helium metastable state population detectable (Sanz-Forcada & Dupree 2008).

This work presents the first results of the Measuring Outflows in Planets orbiting Young Stars (MOPYS) survey. The MOPYS project's aim is to provide observational constraints to the timescales of atmospheric evolution and mass loss processes, and test the predictions of planetary evolution models by comparing them to the evaporation tracers observations. In particular, we are interested in testing the mass-loss processes in planet formation at different timescales. Assuming that young planets undergo higher mass-loss rates than older ones, and higher mass-loss rates are, in general, easier to detect, we search for signs of evaporation using the He I triplet and/or $H\alpha$ line observations as proxy, focusing on transmission spectroscopy observations of ≤ 1 Gyr exoplanets. Moreover, we study the detection rate between young and old planet populations in our sample, and compare the observed He I triplet signals with predicted photo-evaporation mass-loss rates. We scheduled the observations such that telluric contamination of the He I triplet is minimised, taking advantage of a favourable barycentric velocity of the Earth. The majority of the high-resolution spectrographs that we used allowed us to observe the He I triplet and $H\alpha$ simultaneously: CARMENES (Quirrenbach et al. 2014, 2020), HARPS-N+GIANO-B (GIARPS; Claudi et al. 2016), and HARPS+NIRPS (Mayor et al. 2003; Wildi et al. 2022). Although $H\alpha$ might be more affected by the probable stellar activity, the simultaneous observation of the two lines increases

the capability to detect ongoing evaporation. For consistency, we complemented the database of He I triplet and H α observations with some Ly α observations from the literature when possible, although this work does not focus on this UV line.

This manuscript is organised as follows. We describe the observational datasets and the spectroscopic analysis methodology in Section 2. The atmospheric results for each planet are detailed in Section 3, while Section 4 introduces further H and/or He I atmospheric results from the literature. In Sect. 5 we detail our criteria to consider atmospheric detections. In Section 6 we discuss our main findings regarding atmospheric evaporation and the He I triplet. The conclusions of this work can be found in Section 7.

2. Observations and data analysis

2.1. Spectroscopic observations

In this work we analysed 16 transits observed with the Calar Alto high-Resolution search for M dwarfs with Exoearths with Near-infrared and optical Échelle Spectrographs (CARMENES, Quirrenbach et al. 2014, 2020) spectrograph located at the Calar Alto Observatory, Almería, Spain. CARMENES has two spectral channels: the optical channel (VIS), which covers the wavelength range from 0.52–0.96 μm with a resolving power of $\mathcal{R}=94\,600$, and the near-infrared channel (NIR), which covers 0.96–1.71 μm with a resolving power of $\mathcal{R}=80\,400$. The targets were observed with both channels simultaneously.

Fibre A was used to observe the targeting star, while fibre B was placed on blank sky in order to monitor the sky emission lines (fibres A and B are separated by 88 arcsecs in the east-west direction). The observations were reduced using the CARMENES pipeline caracal (Caballero et al. 2016), and both fibres were extracted with the flat-optimised extraction algorithm (Zechmeister et al. 2014).

We also analysed 11 transits observed with the High Accuracy Radial velocity Planet Searcher for the Northern hemisphere (HARPS-N, Cosentino et al. 2012) and/or GIANO-B (Oliva et al. 2012) spectrographs mounted on the 3.6m *Telescopio Nazionale Galileo* (TNG) at Roque de los Muchachos Observatory, La Palma, Spain. HARPS-N is an optical spectrograph which covers the wavelength range from 0.383–0.693 μm with a resolving power of $\mathcal{R}=115\,000$. HARPS-N spectra were extracted using the standard Data Reduction Software (DRS) pipeline (Cosentino et al. 2014). GIANO-B (Oliva et al. 2012) is a near-infrared spectrograph which covers the wavelength range from 0.95–2.45 μm with a resolving power of $\mathcal{R}\approx 50\,000$. When possible, the observations were done in GIARPS mode (Claudi et al. 2016), which allows the simultaneous use of HARPS-N and GIANO-B spectrographs.

GIANO-B observations were carried out with the nodding acquisition mode, where the object is observed at two different predefined positions on the slit (A and B) following an ABAB pattern (Claudi et al. 2016). The nodding technique enable to monitor the sky with the slit position that is not on the object, and then efficiently subtract the thermal background and telluric emission lines. The GIANO-B spectra were wavelength calibrated, and extracted using the GOFIO pipeline (Rainer et al. 2018).

Table 1 shows the observing log of the planetary transits analysed in this work, indicating the instrument used in each case. We computed the central time of transit (T_c) and its uncertainty (σ_{T_c}) with the *Transit and Ephemeris Service* tool from

NASA Exoplanet Archive¹ and the parameters from Table 2. The core of the MOPYS observations were conducted as part of the 21B-3.5-004, 22A-3.5-007, 22B-3.5-009, 23A-3.5-009, and 23B-3.5-002 observing programmes (PI J. Orell-Miquel) with CARMENES, and CAT21B_61, CAT22A_9, CAT22B_43, and CAT23A_100 observing programmes (PI J. Orell-Miquel) at TNG. K2-100 b, V1298 Tau c, HD 235088 b, and TOI-2048 b were observed using GTO time by the CARMENES consortium.

We processed the VIS and NIR CARMENES, and HARPS-N observations with *serval*² (Zechmeister et al. 2018), which derives the relative radial velocities (RVs) and several activity indicators: the chromatic radial velocity index (CRX), the differential line width (dLW), and the H α , Na I D1 and D2 and Ca II IRT line indices. Moreover, for the HARPS-N datasets we also used the YABI tool,³ an online version of the HARPS-N DRS pipeline, to derive absolute RVs and spectral activity indicators: cross-correlation function (CCF) full width at half maximum (FWHM), CCF constrast (CTR), bisector (BIS), and Mont-Wilson S-index. For the targets only observed with GIANO-B (because the GIARPS mode was not possible), we inspected the H Paschen lines in the NIR as stellar activity indicators. We constructed the stellar light curve of the H Paschen β (Pa- β , 12821.6 Å), H Paschen γ (Pa- γ , 10941.1 Å), and H Paschen δ (Pa- δ , 10052.1 Å) lines. Abrupt and/or strong variations in the time evolution of the activity indices or lines may indicate stellar activity or flares during the transit, and could compromise or challenge the detection of planetary signals, in particular absorption lines in the visible part of the spectrum (Palle et al. 2020b; Orell-Miquel et al. 2023).

RV measurements during a transit can be used to look for the Rossiter-McLaughlin (RM; Rossiter 1924; McLaughlin 1924) effect. During the crossing of a planet in front of its host star, the planet blocks different parts of the stellar disc. That produces an RV anomaly during the transit known as the RM effect. The detection of the RM effect in RV time series taken during a planetary transit enables the confirmation of the presence of the transiting planet and also helps to determine the orbital configuration and architecture of the planetary system. This technique has been successfully applied to young planets unveiling the architecture of its planetary systems, such as AU Mic b (Palle et al. 2020b) or DS Tuc A b (Benatti et al. 2021). Because we used the CARMENES instrumental configuration where fibre B points at the sky, there were no simultaneous Fabry-Pérot calibrations during the observations. Without them, the RV time evolution is dominated by the instrument drift during the night.

2.2. Photometric observations

We refined the ephemerides and planetary properties of TOI-2048 b, HD 73583 b & c, K2-77 b, TOI-1807 b, TOI-1683 b, TOI-2076 b, TOI-2018 b, and TOI-1268 b using photometric data.

From the *Transiting Exoplanet Survey Satellite* (TESS; Ricker et al. 2015), we analysed the 2-minute cadence TESS simple aperture photometry (SAP; Morris et al. 2017) using *juliet*⁴ (Espinoza et al. 2019). This python library is based on other public packages for transit light curve (batman, Kreidberg 2015), and for Gaussian process (GP; celerite, Foreman-

¹ <https://exoplanetarchive.ipac.caltech.edu/cgi-bin/TransitView/nph-visibletbls?dataset=transits>

² <https://github.com/mzechmeister/serval>

³ Available at <http://ia2-harps.oats.inaf.it:8000>.

⁴ <https://juliet.readthedocs.io/en/latest/index.html>

Table 1: Observing log of the transits analysed in this work. Columns from left to right: name of the planet, spectrograph used, date of starting night of the observations, starting and ending time of observations, central time of the scheduled transit T_c , 1σ uncertainty of T_c , median exposure time of the observations, number of spectra fully taken between the first (T_1) and fourth (T_4) contacts ($N_{T_{14}}$) compared to the total number of spectra taken during the observations (N_{obs}), median signal-to-noise ratio (S/N) value at the spectral orders of H α and/or He I lines, respectively.

| Planet | Instrument | Date | Start [UT] | End [UT] | T_c [UT] | σ_{T_c} [min] | T_{exp} [min] | $N_{T_{14}}/N_{\text{obs}}$ | Median S/N |
|-------------|------------|-------------|---------------|-------------|------------------|-------------------------|---------------------------|-----------------------------|---------------|
| MASCARA-2 b | CARMENES | 2017 Aug 23 | 21:09 | 02:36 | 23:53 | 0.5 | 3.3 | 50/70 | 101/86 |
| K2-100 b | CARMENES | 2020 Jan 07 | 21:21 | 01:18 | 23:18 | 1 | 3.3 | 23/60 | 28/28 |
| V1298 Tau c | CARMENES | 2020 Jan 05 | 18:27 | 01:08 | 20:21 | 16 | 20 | 12/20 | 97/104 |
| TOI-1431 b | GIANO-B | 2020 May 31 | 23:46 | 05:14 | 01:14 | 1 | 1.6 | 50/116 | 44 |
| TOI-2048 b | CARMENES | 2021 Jun 07 | 21:11 | 03:04 | 23:27 | 8 | 10 | 18/32 | 32/39 |
| HD 63433 b | CARMENES | 2021 Nov 01 | 02:08 | 05:10 | 02:43 | 2 | 1 | 79/111 | 40/43 |
| | CARMENES | 2022 Nov 27 | 22:48 | 03:10 | 01:00 | 2.5 | 5 | 26/36 | 111/124 |
| HD 63433 c | CARMENES | 2023 Feb 18 | 21:40 | 03:00 | 00:23 | 4.4 | 5 | 41/54 | 142/139 |
| HD 73583 b | HARPS-N | 2022 Jan 12 | 23:44 | 03:33 | 01:31 | 1 | 10 | 12/23 | 86 |
| HD 73583 c | GIARPS | 2023 Jan 04 | 23:41 | 05:56 | 01:59 | 1 | 10 | 20/37 | 69/72 |
| HD 235088 b | CARMENES | 2022 Aug 06 | 21:00 | 01:18 | 23:07 | 0.8 | 5 | 28/44 | 72/86 |
| K2-77 b | CARMENES | 2022 Sep 27 | 23:40 | 04:28 | 03:21 | 9 | 10 | 14/26 | 23/29 |
| TOI-2046 b | GIARPS | 2022 Sep 29 | 19:51 | 01:05 | 21:39 | 9 | 10 | 13/30 | 22/21 |
| TOI-1807 b | CARMENES | 2021 Dec 16 | 02:48 | 05:39 | 05:34 | 1 | 10 | 3/16 | 32/40 |
| | CARMENES | 2022 Dec 23 | 02:05 | 05:20 | 03:45 | 2 | 6.6 | 8/25 | 61/77 |
| TOI-1136 d | HARPS-N | 2021 May 14 | 21:29 | 03:55 | 00:36 | 7 | 15 | 15/26 | 43 |
| | CARMENES | 2023 Jan 30 | 23:41 | 06:15 | 03:17 | 3 | 15 | 15/24 | 91/88 |
| TOI-1268 b | GIANO-B | 2023 Feb 24 | 23:15 | 06:50 | 04:02 | 0.5 | 10 | 21/42 | 39 |
| TOI-2076 b | CARMENES | 2022 May 11 | 21:55 | 03:29 | – ^(a) | – | 5 | 0/54 | 72/85 |
| | CARMENES | 2023 Apr 13 | 22:01 | 04:35 | 23:37 | 6 | 10 | 15/32 | 80/90 |
| TOI-1683 b | CARMENES | 2022 Sep 11 | 00:33 | 01:15 | 01:40 | 3.7 | 6.6 | 3/6 | 26/33 |
| | GIANO-B | 2023 Sep 19 | 01:05 | 05:55 | 02:09 | 3.8 | 10 | 8/24 | 39 |
| | GIANO-B | 2023 Sep 22 | 00:57 | 05:43 | 03:32 | 3.8 | 10 | 8/26 | 41 |
| WASP-189 b | GIANO-B | 2019 May 06 | 21:42 | 04:46 | 01:18 | 0.1 | 1.6 | 95/156 | 67 |
| HAT-P-57 b | CARMENES | 2018 Jul 08 | 21:24 | 02:56 | 00:05 | 6 | 10 | 18/30 | /47 |
| TOI-2018 b | GIARPS | 2022 Apr 09 | 23:34 | 06:00 | 00:12 | 3.3 | 5 | 19/67 | 29/53 |
| | GIARPS | 2022 Jun 15 | 21:52 | 02:33 | 22:17 | 3 | 5 | 11/45 | 33/40 |

Notes. ^(a) No planetary transit was observed.

Mackey et al. 2017) modelling and uses nested sampling algorithms (dynesty, Speagle 2020; MultiNest, Feroz et al. 2009; Buchner et al. 2014) to explore all the parameter space. In the fitting procedure, we adopted a quadratic limb-darkening law with the (q_1, q_2) parameterisation introduced by Kipping (2013), and we considered the uninformative sample (r_1, r_2) parameterisation introduced in Espinoza (2018) to explore the impact parameter of the orbit (b) and the planet-to-star radius ratio ($p = R_p/R_\star$) values. We modelled the photometric variability of the young host stars adding to fit the celerite GP exponential or celerite GP quasi-periodic kernels. We followed the same procedure applied to analyse the HD 235088 system in Orell-Miquel et al. (2023).

One transit of TOI-1268 b and TOI-2018 b each were observed by the multi-colour imager MuSCAT2 (Narita et al. 2019) mounted at the 1.52-m Telescopio Carlos Sánchez (TCS) in the Teide Observatory in Tenerife, Spain. MuSCAT2 obtained simultaneous photometric data of the transits in four bands (Sloan g, r, i, z_s). The exposure times for each band were optimised for each night, CCD and target to avoid the saturation of the target and comparison stars in the field. Standard data reduction, aperture photometry, and transit modelling including systematic effects was performed by the MuSCAT2 custom pipeline (Parviainen et al. 2019).

One partial transit of TOI-2076 b was observed on the night of 14 May 2023 with the Sinistro imager mounted on one of the two 1-m telescopes (Dome B) operated by Las Cumbres Ob-

servatory (LCO; [Brown et al. 2013](#)) at the Teide Observatory in Tenerife, Spain. The observations were performed through the rp-band filter, in the full-frame mode, and with an exposure time of 10 s. To avoid detector saturation, the telescope was defocused such that the FWHM of the stellar point spread function was 7"–8". The observation started at 22:00 UT, about 1.6 hours before the expected ingress time, and halted at 01:03 UT, in the middle of the expected transit, due to a technical problem. The obtained images were processed by the BANZAI pipeline ([McCully et al. 2018](#)) for dark and flat corrections. The light curve of TOI-2076 was then extracted by aperture photometry using a custom pipeline ([Fukui et al. 2011](#)), and the transit modelling was performed with *juliet*.

More details of each transit analysis can be found in their corresponding sections (TOI-1268 b: Sect. 3.15, TOI-2018 b: Sect. 3.20, and TOI-2076 b: Sect. 3.16).

2.3. Telluric correction

The main objective of these observations was the analysis of the He I triplet at $\sim 10833 \text{ \AA}$. However, the He I lines are surrounded by emission and absorption telluric lines. There is an H₂O absorption line at 10835 \AA and there are four emission lines of hydroxyl (OH) at 10832.1 \AA , 10832.4 \AA , 10834.2 \AA , 10834.3 \AA ([Oliva et al. 2015](#)), although the last two are detected in the spectra as a single peak. Due to the Earth's orbital motion the relative positions of the planet and telluric spectral lines change with the epoch. Thus, we only scheduled the observations during transiting epochs that minimise overlapping and mitigate the contamination over the He I triplet (see [Orell-Miquel et al. 2022](#); [Spake et al. 2022](#) for further details).

When analysing the transits presented in this work, we encountered another source of contamination of the He I triplet. We detected an emission line at $\sim 10833 \text{ \AA}$ in few transits where we needed to extend the observations into the astronomical twilight. This emission line only appears in the last few spectra and its strength increases towards the end of the night. We presume it is scattered sunlight from the incoming dawn.

Because each spectrograph has its own particularities, we handled with the telluric emission and absorption contamination differently for each of the instruments, see next subsections.

2.3.1. CARMENES telluric correction

We corrected the CARMENES VIS and NIR spectra from telluric absorptions following the approach described in [Nagel et al. \(2023\)](#) with the *molecfit* package in version 1.5.9 ([Smette et al. 2015](#); [Kausch et al. 2015](#)). Then, we corrected the He I region of the CARMENES NIR data from telluric OH emission following the methodology described in previous He I studies (e.g. [Nortmann et al. 2018](#); [Palle et al. 2020a](#); [Czesla et al. 2022](#)), in particular [Orell-Miquel et al. \(2022, 2023\)](#).

We used fibre B to generate a synthetic emission model fitting simultaneously the three main OH peaks with three independent Gaussian profiles. The amplitude, central position, and standard deviation of the Gaussian profiles were set free, and we only introduced an initial guess for their central positions. Prior to applying the emission model to fibre A, we accounted for the different efficiency of the two injection fibres. For each dataset, we computed the scaling factor between fibres comparing the strongest OH peak from the co-added spectra of each fibre. We assumed the scaling factor to be constant during the night. Finally, for each pair of target and sky spectra, we divided

the science spectra by its particular OH emission model, multiplied by the nightly scaling factor. When we detected the solar He I emission line in fibre B, we added a fourth Gaussian profile in the fitting procedure.

2.3.2. HARPS-N telluric correction

We corrected the HARPS-N spectra from telluric absorptions with *molecfit* (v4.2) via its implementation in the SLOppy (Spectral Lines Of Planets with python, [Sicilia et al. 2022](#)) package. We only used SLOppy for the purpose of running *molecfit* easily on HARPS-N data, and correct those spectra from telluric absorptions.

Although the wavelength solution from the original HARPS-N data is based on wavelengths in air, the *molecfit* correction provides a wavelength solution in the vacuum. Because CARMENES and GIANO-B wavelengths are in the vacuum, we also used the vacuum wavelengths for the HARPS-N data for consistency.

2.3.3. GIANO-B telluric correction

Due to our planning of the observations, the H₂O absorption line is always far from the He I triplet. Thus, we decided to not correct the GIANO-B spectra from telluric absorption. If a particular residual map or transmission spectrum shows strong telluric residuals, we simply masked that spectral region.

The sky emission lines are corrected by the GOFIO pipeline, taking advantage of the nodding technique. This procedure is very efficient in removing emission lines that have similar strength in consecutive exposures. However, the He I emission increases too quickly between exposures for the ABAB nodding procedure to provide an accurate correction for the emission contamination. We inspected the individual spectra and masked the affected wavelength region of particular spectra.

2.4. Transmission spectrum analysis

We analysed the spectroscopic observations via the well-established transmission spectroscopy technique (e.g. [Wytenbach et al. 2015](#); [Casasayas-Barris et al. 2017](#)) successfully applied in [Orell-Miquel et al. \(2022, 2023\)](#). The planetary and stellar parameters needed to compute the transmission spectra for each planet are shown in Table 2.

The telluric corrected spectra are normalised by a first degree polynomial. We used a blue and red region near the line of interest and free of tellurics to fit the polynomial. The spectra are shifted into the stellar rest frame, accounting for the Earth's barycentric movement, the stellar systemic velocity (γ), and the stellar Doppler shift induced by the planet. Then, we created a high signal-to-noise ratio (S/N) stellar spectrum (Master-Out; MO) by calculating the mean of all the spectra taken completely during out-of-transit, and we divided all the spectra by the MO. With this step, the stellar spectrum is removed from the spectroscopic time series. Next, we moved the spectra to the planetary rest frame using the formula

$$v_p(t) = K_p \sin(2\pi\phi(t)), \quad (1)$$

where K_p is the radial velocity semi-amplitude that the star induces to the planet, and ϕ is the orbital phase. We neglected orbital eccentricity because the values provided for the planets in the literature are usually poorly constrained and the impact

Table 2: Transit and system parameters used to compute the transmission spectra for each planet analysed in this work.

| Planet | P [d] | $T_0^{(a)}$ [d] | $T_{14}^{(b)}$ [h] | $T_{12}^{(b)}$ [min] | a_p [au] | i_p [deg] | γ [km s ⁻¹] | K_* [m s ⁻¹] | $K_p^{(c)}$ [km s ⁻¹] |
|-------------|--------------------------------|----------------------------------|--|---|-----------------------------|--|-----------------------------------|---|--------------------------------------|
| K2-100 b | 1.6739035 (4) ⁽²⁾ | 140.71941 (27) ⁽²⁾ | 1.60±0.01 ⁽¹⁾ | 2.8±0.8 ⁽¹⁾ | 0.0301 (14) ⁽²⁾ | 81.27±0.37 ⁽²⁾ | +34.393 (3) ⁽²⁾ | 10.6±3.0 ⁽²⁾ | 193±9 |
| MASCARA-2 b | 3.4741070 (19) ⁽¹⁾ | 909.5906 (3) ⁽²⁾ | 3.57±0.02 ⁽¹⁾ | 29±1 ⁽¹⁾ | 0.0542 (21) ⁽¹⁾ | 86.15 ^{+0.28} _{-0.27} ⁽¹⁾ | -21.07 (3) ⁽²⁾ | 322.51 ⁽³⁾ | 170±7 ⁽³⁾ |
| V1298 Tau c | 8.249071 (58) ⁽¹⁾ | 1854.3479 (11) ⁽¹⁾ | 4.66±0.12 ⁽²⁾ | 12 ⁽²⁾ | 0.0841 (13) ⁽³⁾ | 88.5 ^{+0.9} _{-0.7} ⁽²⁾ | +14.64 (14) ⁽⁴⁾ | 4 ⁺⁵ ₋₃ ⁽³⁾ | 111±2 |
| TOI-1431 b | 2.6502409 (41) ⁽¹⁾ | 1739.17728 (11) ⁽¹⁾ | 2.489±0.009 ⁽¹⁾ | 0.716±0.022 ⁽¹⁾ | 0.0465 (17) ⁽¹⁾ | 80.30 ^{+0.18} _{-0.17} ⁽¹⁾ | -25.154 ⁽¹⁾ | 294.1±1.1 ⁽¹⁾ | 188.15 ⁽²⁾ |
| TOI-2048 b | 13.790546 (55) ⁽¹⁾ | 1739.1123 (27) ⁽¹⁾ | 3.5±0.1 ⁽¹⁾ | 6.9 ^{+1.2} _{-0.7} ⁽¹⁾ | 0.1078 (80) ⁽¹⁾ | 89.41±0.35 ⁽¹⁾ | -7.6 (2) ⁽²⁾ | ~2.8 ⁽¹⁾ | 85±6 |
| HD 63433 b | 7.107789 (10) ⁽²⁾ | 1916.45142 (32) ⁽²⁾ | 3.22±0.03 ⁽¹⁾ | 9±1 ⁽¹⁾ | 0.0719 (44) ⁽¹⁾ | 89.4 ^{+0.4} _{-0.6} ⁽¹⁾ | -15.81 (10) ⁽¹⁾ | 1.4 ^{+1.4} _{-0.9} ⁽³⁾ | 110±6 |
| HD 63433 c | 20.543888 (46) ⁽²⁾ | 1844.05824 (48) ⁽²⁾ | 4.07±0.03 ⁽¹⁾ | 8±1 ⁽¹⁾ | 0.1458 (62) ⁽¹⁾ | 89.15 ^{+0.07} _{-0.20} ⁽¹⁾ | -15.81 (10) ⁽¹⁾ | 3.6 ^{+1.1} _{-1.0} ⁽³⁾ | 77±3 |
| HD 73583 b | 6.3980580 (26) ⁽¹⁾ | 2592.56287 (25) ⁽¹⁾ | 2.100 ^{+0.015} _{-0.013} ⁽¹⁾ | 6.9±0.2 ⁽¹⁾ | 0.0618 (20) ⁽¹⁾ | 88.35±0.07 ⁽¹⁾ | +21.52 ⁽³⁾ | 4.37 ^{+1.5} _{-1.3} ⁽²⁾ | 105±3 |
| HD 73583 c | 18.879300 (48) ⁽¹⁾ | 2949.58243 (77) ⁽¹⁾ | 3.60 ^{+0.03} _{-0.05} ⁽¹⁾ | 6.9±0.20 ⁽¹⁾ | 0.1270 (40) ⁽¹⁾ | 89.96±0.03 ⁽¹⁾ | +21.52 ⁽³⁾ | 2.89 ^{+0.53} _{-0.51} ⁽²⁾ | 73.2±2.3 |
| HD 235088 b | 7.4341394 (60) ⁽¹⁾ | 2798.4635 (56) ⁽¹⁾ | 2.700±0.025 ⁽¹⁾ | 4.4±0.5 ⁽¹⁾ | 0.0725 (35) ⁽¹⁾ | 88.85±0.30 ⁽¹⁾ | -27.370 (2) ⁽²⁾ | ~2.5 ⁽¹⁾ | 106±5 |
| K2-77 b | 8.200139 (60) ⁽¹⁾ | 2522.6338 (35) ⁽¹⁾ | 2.68±0.22 ⁽¹⁾ | 6.3 ^{+1.5} _{-1.1} ⁽¹⁾ | 0.0751 (45) ⁽¹⁾ | 88.7 ^{+0.7} _{-0.4} ⁽¹⁾ | +7.35 (20) ⁽²⁾ | ~3.4 ⁽¹⁾ | 100±6 |
| TOI-2046 b | 1.4971842 (6) ⁽¹⁾ | 1792.2767 (23) ⁽¹⁾ | 2.410 (32) ⁽¹⁾ | 21±1 ⁽²⁾ | 0.0267 (18) ⁽²⁾ | 83.6±0.9 ⁽¹⁾ | -9.480 (43) ⁽¹⁾ | 374.7±7.8 ⁽¹⁾ | 193±13 |
| TOI-1807 b | 0.54937084 (65) ⁽¹⁾ | 2664.06930 (75) ⁽¹⁾ | 0.970±0.022 ⁽¹⁾ | 1.45 ^{+0.25} _{-0.18} ⁽¹⁾ | 0.0121 (9) ⁽¹⁾ | 81.7±1.8 ⁽¹⁾ | -7.33±0.59 ⁽³⁾ | 2.39 ^{+0.45} _{-0.46} ⁽²⁾ | 235±6 |
| TOI-1136 d | 12.51937 (41) ⁽¹⁾ | 2349.525 (5) ⁽¹⁾ | 4.12±0.11 ⁽¹⁾ | 11.0±0.5 ⁽¹⁾ | 0.1057 (46) ⁽¹⁾ | 89.41±0.28 ⁽¹⁾ | +6.91±0.33 ⁽²⁾ | ~2.2±0.6 ⁽¹⁾ | 92±4 |
| TOI-1268 b | 8.1577094 (45) ⁽¹⁾ | 3000.66841 (14) ⁽²⁾ | 4.001±0.025 ⁽¹⁾ | 21±2 ⁽¹⁾ | 0.0711 (63) ⁽¹⁾ | 88.63 ^{+0.32} _{-0.30} ⁽¹⁾ | +3.79±0.14 ⁽³⁾ | 31.7 ^{+2.5} _{-2.6} ⁽¹⁾ | 105±8 |
| TOI-2076 b | 10.355183 (65) ⁽¹⁾ | 3079.5495 (45) ⁽²⁾ | 3.251±0.03 ⁽³⁾ | 8.5±0.2 ⁽³⁾ | 0.0682 (13) ⁽³⁾ | 88.9±0.11 ⁽³⁾ | -13.19±0.21 ⁽⁴⁾ | ~2 ⁽³⁾ | 71.6±1.3 |
| TOI-1683 b | 3.057541 (14) ⁽¹⁾ | 2522.7001 (12) ⁽¹⁾ | 1.43 ^{+0.07} _{-0.05} ⁽¹⁾ | 5.0 ^{+0.8} _{-0.6} ⁽¹⁾ | 0.0368 (23) ⁽¹⁾ | 86.80±0.38 ⁽¹⁾ | +38.4±0.3 ⁽²⁾ | ~5 ⁽³⁾ | 130±8 |
| WASP-189 b | 2.7240330 (42) ⁽¹⁾ | 1926.5416960 (65) ⁽¹⁾ | 4.351±0.026 ⁽²⁾ | 18.6±6.2 ⁽²⁾ | 0.05053 (98) ⁽¹⁾ | 84.03±0.14 ⁽¹⁾ | -24.465±0.012 ⁽¹⁾ | 182±13 ⁽¹⁾ | 200±4 |
| HAT-P-57 b | 2.4652950 (32) ⁽¹⁾ | 5113.48127 (48) ^(a,1) | 3.499±0.019 ⁽¹⁾ | 19.1±0.8 ⁽¹⁾ | 0.0406 (11) ⁽¹⁾ | 88.26±0.85 ⁽¹⁾ | -5.99±0.35 ⁽¹⁾ | <215 ⁽¹⁾ | 180±5 |
| TOI-2018 b | 7.435583 (22) ⁽¹⁾ | 2746.4287 (21) ^(a,1) | 2.36±0.09 ⁽¹⁾ | 6.5±0.5 ⁽¹⁾ | 0.0609 (22) ⁽¹⁾ | 88.52±0.22 ⁽¹⁾ | -25.617±0.002 ⁽³⁾ | 4.4±1.0 ⁽¹⁾ | 89.1±3.3 |

References. K2-100b: ⁽¹⁾ [Stefansson et al. \(2018\)](#), ⁽²⁾ [Barragán et al. \(2019\)](#). MASCARA-2 b: ⁽¹⁾ [Lund et al. \(2017\)](#), ⁽²⁾ [Talens et al. \(2018\)](#), ⁽³⁾ [Casasayas-Barris et al. \(2019\)](#). V1298 Tau c: ⁽¹⁾ J. Livingston, priv. comm., ⁽²⁾ [David et al. \(2019\)](#), ⁽³⁾ [Suárez Mascareño et al. \(2021\)](#), ⁽⁴⁾ [Gaidos et al. \(2022\)](#). TOI-1431 b: ⁽¹⁾ [Addison et al. \(2021\)](#), ⁽²⁾ [Stangret et al. \(2021\)](#). TOI-2048 b: ⁽¹⁾ This work (App. C), ⁽²⁾ [Newton et al. \(2022\)](#). HD 63433 b: ⁽¹⁾ [Mann et al. \(2020\)](#), ⁽²⁾ [Zhang et al. \(2022c\)](#), ⁽³⁾ [Mallorquín et al. \(2023\)](#). HD 63433 c: ⁽¹⁾ [Mann et al. \(2020\)](#), ⁽²⁾ [Zhang et al. \(2022c\)](#), ⁽³⁾ [Mallorquín et al. \(2023\)](#). HD 73583 b: ⁽¹⁾ [Barragán et al. \(2022\)](#), ⁽²⁾ [El Mufti et al. \(2021\)](#). HD 73583 c: ⁽¹⁾ [Barragán et al. \(2022\)](#), ⁽²⁾ [El Mufti et al. \(2021\)](#). HD 235088 b: ⁽¹⁾ [Orell-Miquel et al. \(2023\)](#), ⁽²⁾ [Gaia DR2 \(Soubiran et al. 2018\)](#). K2-77 b: ⁽¹⁾ This work (App. F), ⁽²⁾ [Gaidos et al. \(2017\)](#). TOI-2046 b: ⁽¹⁾ [Kabáth et al. \(2022\)](#), ⁽²⁾ Computed using this table parameters. TOI-1807 b: ⁽¹⁾ This work (App. G), ⁽²⁾ [Nardiello et al. \(2022\)](#), ⁽³⁾ [Gaia DR2 \(Soubiran et al. 2018\)](#). TOI-1136 d: ⁽¹⁾ [Dai et al. \(2023a\)](#), ⁽²⁾ [Gaia DR2 \(Soubiran et al. 2018\)](#). TOI-1268 b: ⁽¹⁾ [Šubjak et al. \(2022\)](#), ⁽²⁾ This work (Sect. 3.15), ⁽³⁾ [Gaia DR2 \(Soubiran et al. 2018\)](#). TOI-2076 b: ⁽¹⁾ [Zhang et al. \(2023b\)](#), ⁽²⁾ This work (Sect. 3.16), ⁽³⁾ [Osborn et al. \(2022\)](#), ⁽⁴⁾ [Gaia DR2 \(Soubiran et al. 2018\)](#). TOI-1683 b: ⁽¹⁾ This work (Sect. K), ⁽²⁾ [Gaia DR2 \(Soubiran et al. 2018\)](#), ⁽³⁾ [Zhang et al. \(2023b\)](#). WASP-189 b: ⁽¹⁾ [Lendl et al. \(2020\)](#), ⁽²⁾ [Anderson et al. \(2018\)](#). HAT-P-57 b: ⁽¹⁾ [Hartman et al. \(2015\)](#). TOI-2018 b: ⁽¹⁾ [Dai et al. \(2023b\)](#), ⁽²⁾ This work (Sect. 3.20), ⁽³⁾ [Gaia DR2 \(Soubiran et al. 2018\)](#).

Notes. ^(a) T_0 given in BJD - 2 457 000, except for HAT-P-57 b that is BJD - 2 450 000. ^(b) T_{14} is the total transit duration between the first (T_1) and fourth (T_4) contacts, and T_{12} is the duration of the ingress-egress. ^(c) Calculated from $K_p = 2\pi a_p P^{-1} \sin i_p$ using the parameters in this table, when there is no reference.

for all but one case is of the same order as the uncertainties derived for the signal shifts. The exception to this is TOI-1268 b for which we used the `radvel` ([Fulton et al. 2018](#)) package to account for the eccentricity shift during the transit.

To compute the transmission spectrum (TS), we only consider those spectra taken entirely between the first (T_1) and fourth (T_4) contacts. We averaged them using the inverse of the squared propagated errors ($1/\sigma^2$) as weights. If the residual map contains strong telluric residuals and/or stellar line variability near the inspected line, we mask those affected regions to compute the TS. However, each night is different, and we explain further details of their particularities in the data analysis section (Sect. 3), where needed.

When the TS shows a clear absorption at the expected position, we fitted the feature with a Gaussian profile using the MultiNest algorithm ([Feroz et al. 2009](#)) via its python implementation `PyMultiNest` ([Buchner et al. 2014](#)). Otherwise, when the residual map or the transmission spectrum do not show evidences of absorption from the planetary atmosphere, we derived conservative limits for the planetary absorption. We estimated a 3σ upper limit absorption peak as three times the root-mean-squared (RMS) value of flat spectral region in the continuum of the spectrum close to the line(s) of interest. The exact spectral range might be different in each case to avoid including strong

residuals or very scattered regions. The equivalent width (EW) of a line is a more appropriate measure because it is independent from the instrumental resolution, but it is difficult to compute when there is no line to measure. We give the upper limits in terms of absorption peak and we translate them into EWs (or from EW to absorption peak) as it is explained in App. M.

To analyse the data from GIANO-B, we followed some of the recommendations from [Guilluy et al. \(2020\)](#), [Fossati et al. \(2022\)](#), and [Guilluy et al. \(2023\)](#). We considered the science spectra taken at positions A and B as different instruments, and we combined them after computing both TS. GIANO-B is known to be affected by a fringing pattern that affects high S/N spectra ([Guilluy et al. 2020](#)). However, the lower S/N of our spectra, due to its maximum exposure time of 600 s and the faintness of our targets, prevented us to detect hints of the fringing pattern. The MO spectra obtained from GIANO-B did not show any clear sinusoidal pattern, as seen in [Guilluy et al. \(2020, Fig. 2\)](#). Thus, we decided to not correct the fringing pattern, as it was done in [Fossati et al. \(2022\)](#). Lastly, the wavelength solution of GIANO-B may not be stable during the night. [Guilluy et al. \(2020\)](#) found a typical instrument drift of half of the GIANO-B pixel element during four hours of observations. That could be an issue for the cross-correlation technique, where excellent precision in the wavelength solution is needed ([Brogi](#)

et al. 2018). However, the transmission spectra technique does not require such extreme precision, and hence we did not apply any correction to our GIANO-B observations, which have lower S/N than in Guilluy et al. (2020).

Another aspects to take into account with transit observations are the Rossiter-McLaughlin (RM) and center-to-limb-variation (CLV) effects, which can interfere or mimic single line absorptions (Casasayas-Barris et al. 2021b). Because these effects scale with R_p/R_* , they have larger impact on gas giant transmission observations. Previous He I triplet line works proved that they have negligible contributions on the He I results (e.g. Nortmann et al. 2018; Guilluy et al. 2023). Here, we computed the RM and CLV models for HD 63433 b ($R_p = 2.1 R_\oplus$) and TOI-1136 d ($R_p = 4.6 R_\oplus$) whose contribution to the H α and He I triplet signals is negligible. These analyses and results are presented in Sect. 3. The models of RM and CLV effects were created with the *Turbospectrum2019* (Plez 2012), using the Kurucz ATLAS9 (Castelli & Kurucz 2003) and VALD3 (Ryabchikova et al. 2015) line lists. The stellar models were created for 21 limb-darkening angles assuming local thermodynamical equilibrium (LTE). In the next step, taking into account the system parameters, we calculated the stellar models for orbital phases from -0.05 to 0.05 , remembering that the planet covers different stellar regions with different limb-darkening during its transit. Next, all models were divided by the out-of-transit spectrum, creating the RM and CLV effect model for each orbital phase and wavelength. However, it is necessary to first detect the RM in the RV time series to compute the models, and the effect is not detected for all our targets.

3. Transmission spectroscopy results

In this section we present the results and the details of the residuals maps and TS calculations planet by planet. We present an example of a residuals map and TS figure in Figure 1, and the figures for the rest of transits without detections are shown in Appendix A. Furthermore, the time evolution of the activity indicators derived from the analysed transits can be found in Appendix A as well.

3.1. K2-100b

The resulting residual maps and TS centred in the spectral regions of the H α and He I triplet are shown in Figure 1. The time evolution of all the activity indices is mainly flat, and there is no evidence of strong stellar variability during the transit.

The He I triplet TS shows a flat spectrum, while the H α TS is flat with some emission features from stellar variations in the line core during the transit. We found no significant absorption in either of the lines, and we placed a 3σ upper limit to the excess absorptions of 1.4 % and 1.3 % for H α and He I, respectively.

K2-100b was already observed with the InfraRed Doppler (IRD) spectrograph on the 8.2-m Subaru telescope ($R = 70\,000$; Kotani et al. 2018). Gaidos et al. (2020a) derived an EW 99% confidence detection upper limit of 5.7 mÅ. From Fig. 8 therein, we estimated an absorption depth of $\sim 1.2\%$, which is consistent with the upper limit derived from the CARMENES observations.

3.2. MASCARA-2b

Casasayas-Barris et al. (2019) already detected H α in MASCARA-2b using CARMENES and HARPS-N observations. The H α absorption measured with CARMENES VIS data

was $-0.85 \pm 0.03\%$, and while combining 3 nights with HARPS-N was $-0.68 \pm 0.06\%$.

Here, we inspected the CARMENES NIR spectra, which were not analysed in Casasayas-Barris et al. (2019), looking for He I excess absorption. Figure A.1 presents the residual map and TS around the He I triplet. Because some telluric OH variability was still remaining in the residual map, we masked the affected regions. Despite the structure in the final TS, due to the masked regions, we found no significant planetary absorption. We computed a 3σ upper limit to the He I excess absorption of 0.5 %.

3.3. V1298 Tau c

V1298 Tau planetary system is known to have transit time variations (TTVs) that can complicate the analysis of high-resolution spectroscopy observations (David et al. 2019). According to non-linear ephemerids for the V1298 Tau system (J. Livingston, priv. comm.), a nearly complete transit of planet c was observed the night of 5 of January 2020. Unfortunately, we missed pre-transit observations which are critical to compute a good MO and to check for stellar variability during the observations.

For this transit, the *serval* H α index shows a clear decrease only from about mid-transit to egress, and an increase at the end of the observations. We did not include those last spectra in the computation of the MO spectrum, although they are plotted in the residual maps. The other *serval* products do not show signs of strong stellar activity (see Fig. A.20).

The H α residual map (Fig. A.2 left) shows a clear absorption region coincident with the *serval* H α index decrease, suggesting the stellar origin of the signal. We computed the TS only with the non-affected spectra from the first half of the transit. We fitted a $-1.10 \pm 0.13\%$ feature at the H α position, which is consistent with the 3σ upper limit derived from the nearby spectral region (1.1 %). The priors and posterior values from the fit are listed in Table B.1, and the posterior distributions are shown in Fig. B.1.

The first half of the transit in the He I NIR triplet residual map (Fig. A.2 left) shows an extended absorption region, which does not coincide in time with the H α variability detected. In the second half of the transit, there is a vertical absorption feature in the stellar rest frame that does not follow the planetary track when we shift the spectra into the planet rest frame. This feature seems to be related to telluric residuals. We computed the TS with those unaffected spectra from the first half of the transit. The He I TS has a deep ($-3.75 \pm 0.12\%$) and broad ($1.02 \pm 0.04 \text{ \AA}$) absorption feature, which is larger than the 3σ upper limit (1.1 %). The priors and posterior values from the fit are listed in Table B.2, and the posterior distributions are shown in Fig. B.1.

To explore the origin of the H α and He I features, we computed the TS from the unaffected spectra (start phase), the centre of the transit (centre phase), the end of the transit (end phase), and post-transit. We compare those TS with the MO spectra in Fig. B.2. The start TS from H α and He I lines show a different behaviour from centre and end. Furthermore, the comparison between TS and MO evidences the stellar line profile variation during the observations. Therefore, we cannot confidently attribute the detected features to V1298 Tau c atmosphere. Moreover, the H α TS in Fig. B.2 show a tiny bump at $\sim 6563 \text{ \AA}$ which can be attributed to the star and its youth. The surprisingly large Δv ($-28.7 \pm 1.1 \text{ km s}^{-1}$) is another reason for not claiming the significant He I signal as a detection.

The H α line of V1298 Tau c was previously explored by Feinstein et al. (2021) and Schlawin et al. (2021). Feinstein et al.

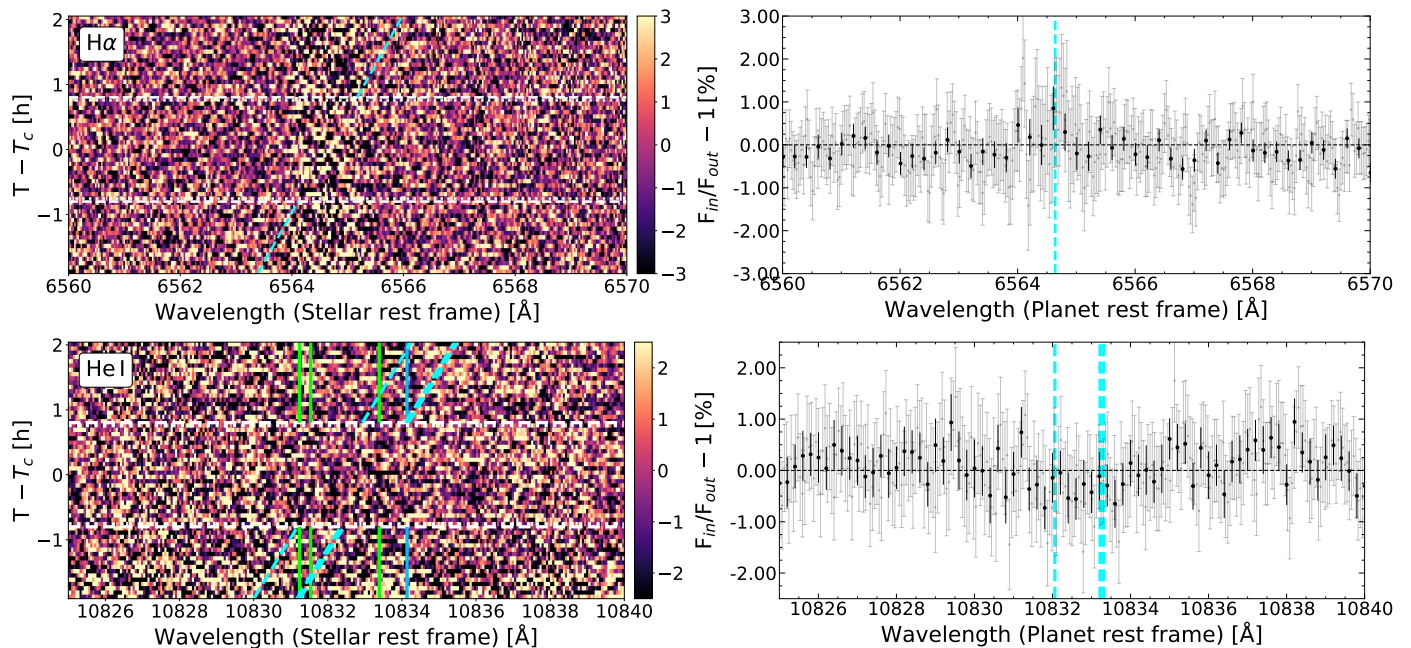


Fig. 1: Residuals maps and transmission spectra around the $H\alpha$ line (*top panels*) and He I NIR triplet (*bottom panels*) lines for K2-100 b observations with CARMENES. *Left panels*: Residual maps in the stellar rest frame. Time since mid-transit time (T_c) is shown on the vertical axis, wavelength is on the horizontal axis, and relative absorption is colour-coded. The dashed and dotted white horizontal lines indicate the different contacts during the transit. The dashed cyan tilted lines indicate the predicted trace of the planetary signals. The solid green vertical lines indicate the position of the OH emission telluric lines. The solid blue line indicates the position of the H_2O absorption telluric line. *Right panels*: Planet transmission spectra (TS) in the planet rest frame. We show the original data in light grey and the data binned by 0.2 \AA in black. When an absorption signal is fitted, a red line and shaded region show the best Gaussian fit model with its 1σ uncertainties. The dotted cyan vertical lines indicate the $H\alpha$ (*top*) and the He I triplet (*bottom*) lines positions. All the wavelengths in this figure are referenced in a vacuum.

(2021) studied with the Gemini/GRACES spectrograph the behaviour of the $H\alpha$ and Ca II infrared triplet during a transit, finding significant variations of the $H\alpha$ during the observations. Schlawin et al. (2021) analysed one transit looking for $H\alpha$ absorption with the PEPsi spectrograph, but the observations were affected by stellar variability. Furthermore, Vissapragada et al. (2021) explored the He I triplet of planet c with the Habitable-zone Planet Finder (HPF) spectrograph, but the in-transit spectra were affected by a stellar flare. Lastly, a transit of planet c was observed with narrow-band helium filter photometry, but Vissapragada et al. (2021) did not detect the transit during the observations.

Unfortunately, our observations join the previous unsuccessful attempts to analyse the atmosphere of V1298 Tau c. Due to the many complications that affected the observations, we adopted the absorption peaks from the $H\alpha$ and He I features as upper limits of any possible planetary absorption. Our upper limits to $H\alpha$ and He I excess absorption are 1.1 % and 3.7 %, respectively.

3.4. TOI-1431 b

Stangret et al. (2021) analysed two HARPS-N and one EXPRES transits, finding no signs of atomic or molecular absorption. A tentative detection of $H\alpha$ appeared only during the first HARPS-N dataset ($0.33 \pm 0.07 \%$), but it was considered as stellar variability because it was not reproduced in the other two visits. We consider that absorption feature as an upper limit for the purpose of this work.

Here, we looked for He I excess absorption in the GIANO-B spectra from the first night of Stangret et al. (2021). The residual map and TS are shown in Fig. A.3. The TS is mainly flat and we placed a 3σ upper limit to the He I excess absorption of 0.4 %.

3.5. TOI-2048 b

Newton et al. (2022) noted that ground-based follow-up observations found a tentative transit detection ~ 20 min later than expected. We analysed the new available TESS data to derive updated ephemerides. The details of the photometric fit are explained in Appendix C. We refined TOI-2048 b ephemerides and planet properties (Table C.1), and confirmed the detected delay from ground-based observations. Furthermore, because TOI-2048 b does not have mass measurements, we estimated its probable mass from its radius (Wolfgang et al. 2016) to predict its semi-amplitude K_* . This parameter is required for a proper measurement of the TS. We forecasted a mass of $9.4 \pm 1.0 M_{\oplus}$ and a K_* of $2.8 \pm 0.3 \text{ m s}^{-1}$. The details of all these calculations are explained in App. C as well.

The time evolution of all the activity indicators is mainly flat except for the last four $H\alpha$ index points. We excluded those spectra from the MO combination, although they are plotted in the residual maps. Furthermore, we masked a region near the He I triplet because some residuals still remained after correcting the OH emission. We obtained similar results with or without applying the OH emission correction.

$H\alpha$ shows a narrow absorption feature (see Fig. A.4), but we consider it too narrow to have a planetary origin (it is only one binned point). Moreover, there are emission signals around the

absorption signal in the residual map, and the absorption peak is of the order of the 3σ upper limit of 1.5 %, and is difficult to distinguish from the continuum in the final TS. We found no significant absorption features around He I triplet (Fig. A.4). We placed a 3σ upper limit to the He I excess absorption of ~ 1 %.

3.6. HD 63433 b

The night on 1 November 2021 was cloudy until $\sim 01:40$ UT, and we could only cover the transit partially, without pre-transit information. The observations are a bit noisy because the exposures were set to 1 minute and we missed pre-transit observations due to bad weather conditions. Then, we observed a complete transit one year later, on 27 November 2022. The time evolution of all the activity indicators is mainly flat, without evidence of stellar activity during the observations in both nights. Although the RM effect was detected by Mann et al. (2020), the RM and CLV contribution to the H α and He I triplet transmission spectra is well within the error bars of the TS (see Fig. D.1), so we decided to not correct the data from these marginal effects.

The H α transmission spectrum from the first partial transit displays an absorption feature of $-1.21^{+0.22}_{-0.24}$ % (Fig. A.5). Table D.1 shows the priors and posterior values from the fit and Fig. D.2 shows the posterior distribution. However, we did not recover that H α absorption in our second visit, which covered the entire transit. We consider the H α feature does not have a planetary origin. Due to the different quality around the H α from both nights, we did not combine the two datasets. The residual map and TS for the H α from the second transit is shown in Fig. A.5. We placed a 3σ upper limit to the H α excess absorption of 0.4 %.

The residual maps and TS for the He I triplet from both nights separately are shown in Fig. A.5. The He I triplet was completely uncontaminated from tellurics, and both transmission spectra show some residuals from the stellar Si I line at 10830 Å. Due to the different quality of the nights, we did not combine them and focused on the second event which is less noisy. The TS presents a ~ 0.25 % excess absorption feature just at the expected position, but there is noise structure of similar amplitude. Finally, we adopted a conservative 3σ upper limit of 0.4 %.

Our results on the He I triplet are consistent with the previous upper limit of ~ 0.5 % reported by Zhang et al. (2022c). Their partial transit also showed a ~ 0.2 % excess absorption, but they found a correlation between the stellar He I and H Paschen γ lines. We also compared the H Paschen lines with the He I line, but we could not explain the He I triplet feature as stellar line variability. Further high-S/N observations of HD 63433 b are required to confirm the interesting feature of ~ 0.2 % around the He I triplet found in this work and Zhang et al. (2022c).

Although the study of Ly α observations is not the focus of this work, it is worth mentioning Zhang et al. (2022c) presented HST/STIS observations of HD 63433 b around the Ly α line, but no absorption was found for this planet.

3.7. HD 63433 c

The time evolution of the several activity indicators is flat, except the H α line index that displays a narrow peak close to mid-transit, which is also visible in the H α residual map (Fig. A.6). Therefore, we excluded those spectra to compute the H α TS, which is mainly flat. The H α TS displays a too narrow absorption feature that originates only from the first half of the transit. Thus, we attributed this signal to a stellar origin rather than to

absorption from the planet. We put a 3σ upper limit of 0.4 % to any possible H α excess absorption from the planet's atmosphere.

The He I triplet residual map and TS do not show features from the planetary atmosphere, or from stellar variability (Fig. A.6). We placed a 3σ upper limit to the He I excess absorption of 0.4 %, consistent with the previous upper limit of ~ 0.5 % reported by Zhang et al. (2022c) with Keck/NIRSPEC.

Zhang et al. (2022c) detected an excess absorption of Ly α in one visit of HD 63433 c atmosphere with HST/STIS. However, we do not detect the evaporating atmosphere of HD 63433 c via H α in the VIS, or the He I triplet in the NIR. Similar situation applies to, e.g. GJ 436 b where Ly α was detected (Kulow et al. 2014), but not H α or He I triplet (Cauley et al. 2017; Nortmann et al. 2018; Villarreal D'Angelo et al. 2021).

3.8. HD 73583 b

We analysed the new TESS data to update the ephemerides on HD 73583 planetary system (see App. E) and we used them to analyse the transit of HD 73583 b observed with HARPS-N. The MO spectra was computed without the last three spectra, which show different values in the several H α indicator and YABI S-index. The time evolution for the other activity indicators is mainly flat.

The H α residual map and TS are shown in Fig. A.7, where the last spectra clearly exhibit higher flux in the H α line core. The TS shows a small absorption feature at the H α position, which seems to come from the second half of the transit according to the residual map. The signal is -0.46 ± 0.16 % deep (significance $< 3\sigma$), and has a net shift of $-6.1^{+3.2}_{-2.5}$ km s $^{-1}$. The priors and posteriors from the fit are shown in Table E.3, and the posterior distributions are plotted in Fig. E.3. However, it is hard to link that absorption to the planet atmosphere for two reasons: *i*) the absorption comes mostly from the second half of transit (see the residual map on Fig. A.7), and *ii*) the shift of the feature is in the opposite direction of the He I detection from Zhang et al. (2022b). We considered the ~ 0.5 % absorption feature as the upper limit for H α absorption.

Because GIANO-B was not on the telescope the night of the observations, we could not explore the He I triplet. Zhang et al. (2022b) detected an excess absorption of 0.68 ± 0.08 % from one full and one partial transits of HD 73583 b with Keck/NIRSPEC. These observations were re-analysed in Zhang et al. (2023b) reporting a new excess absorption measurement of 0.72 ± 0.08 %. The He I triplet signal has a blue shift, rather than the usual red-shift reported in the other He I detections.

3.9. HD 73583 c

As we mention in the previous section, the TESS photometric analysis for the HD 73583 planetary system is shown in App. E. Using the values from Barragán et al. (2022), the uncertainty on HD 73583 c T_c would be 50 minutes, while we now obtained a precision of ~ 1 min.

The time evolution of the several H α and dLW indicators show a peak at the beginning of the transit that extends until mid-transit. Thus, to compute the TS, we only considered the spectra from the second half of the transit. The other activity indicators show a scattered but flat time evolution. The H α residual map and TS are shown in Fig. A.8, where the H α variability is visible in the residual map. The TS has a small feature at the expected position. We fitted an absorption of $-0.54^{+0.13}_{-0.14}$ %, and we present the prior and posterior values in Table E.3, and the posterior dis-

tributions are shown in Fig. E.3. Although the fitted absorption is significant ($\sim 3.8\sigma$), we consider that value as an upper limit or a tentative detection. A second transit with better S/N and no stellar activity will confirm these results.

The He I triplet residual map and TS is shown in Fig. A.8. There is no clear evidence of a planetary trace on the residual map or planetary absorption detected on the TS. We placed a 3σ upper limit to the He I excess absorption of 0.5 %.

3.10. HD 235088 b

We observed one transit of this sub-Neptune-sized planet during this project and its results were analysed in depth in Orell-Miquel et al. (2023). We detected a He I blueshifted absorption signal of -0.91 ± 0.11 %, confirming the previous detection from Zhang et al. (2023b) of -0.64 ± 0.06 % absorption. The residual maps and transmission spectra for the H α and He I triplet are shown in Fig. A.9 (adapted from Orell-Miquel et al. 2023).

In this work we adopted the results presented in Orell-Miquel et al. (2023), where an age of 600–800 Myr was estimated for HD 235088.

3.11. K2-77 b

Because K2-77 b ephemerides are based on K2 photometry, we decided to analyse the available TESS data and improve the uncertainties on T_c for this target (see App. F).

According to our results, the last spectrum from the CARMENES observations was taken during the egress, missing the post-transit coverage to compute the MO spectrum. Moreover, the pre-transit observations have low S/N due to higher air-mass.

The difficulties to calculate the MO spectrum are visible in the residual maps and TS for both H α and He I triplet lines (Fig. A.10). We could only derive broad 3σ upper limits for H α and He I excess absorptions of 2.5 % and 2.7 %, respectively.

3.12. TOI-2046 b

We set GIARPS mode observations with similar exposure times than for HARPS-N and GIANO-B. Due to the faintness of the host star ($J = 10.4$ mag), we used GIANO-B's maximum time exposure of 600 s for both spectrographs. The spectra have relatively low S/N around the H α and the He I triplet. Also, the GOFIO pipeline could not properly remove the biggest telluric OH emission peak, and we decided to mask those telluric affected regions. The masked regions are far enough from the He I line to ensure that they do not affect the final results.

H α and He I residual maps and TS are shown in Figures A.11. We only could derive very broad 3σ upper limits for H α and He I excess absorptions of 5 % and 2.9 %, respectively.

3.13. TOI-1807 b

We analysed the newly available TESS data to derive updated ephemerids, and refine the T_c . The details of the photometric fit are explained in App. G, and our results for the planet properties are shown in Table G.1. However, we planned the observations with older ephemerides (Nardiello et al. 2022), missing part of the transit on 16 December 2022. We observed a second full transit on 23 December 2022, also with better S/N. The H α and He I residual maps and TS for both events are shown in Figures A.12. The second visit does not show evidences of absorption features.

We only used the data from the second transit to compute upper limits due to the different quality between both observations. We derived a 3σ upper limit of 0.95 % for H α excess absorption, and an upper limit of 0.80 % for the He I triplet.

A transit of this ultra-short period (USP) Earth-like density planet was already observed with IRD, reporting an upper limit to the He I triplet EW of 4 mÅ (Gaidos et al. 2023, ~ 0.4 % absorption). Because our upper limit is less constraining than the previous observations, we used the results from Gaidos et al. (2023) in the discussion in Section 4.

3.14. TOI-1136 d

One HARPS-N transit of TOI-1136 d was observed to check for the planetary RM signature in the RV time series (Dai et al. 2023a). In this work, we inspected the dataset looking for H α planetary absorption signal. Furthermore, we scheduled a second transit with CARMENES to inspect the whole spectral range. We used nonlinear ephemerides to determine the T_c for the second transit (F. Dai, priv. comm.). The RM and CLV effects over the final TS of H α and He I triplet lines are negligible (Fig. H.1). Thus, we did not correct the data from these marginal effects.

The residual maps and TS of the H α for the individual nights are shown in Figure A.13, while the final results are shown in Figure 2. HARPS-N results show a noisy TS with a small absorption feature. However, a similar feature is also detected in the CARMENES H α TS, which has higher S/N. The results from both nights confirm the H α detection on the atmosphere of TOI-1136 d. The combined H α residual map and TS are shown in Fig. A.13. We fitted the signal obtaining an absorption of $-1.12^{+0.12}_{-0.13}$ %. Table H.1 presents the priors and posteriors, and Fig. H.2 shows the posterior distributions. Although the signal is a bit deeper in the first half of the transit, the H α transit light curve (Fig. 3) shows an absorption consistent with the transit duration without evidences of tail-like structure.

For the He I triplet, because the CARMENES observations were performed close to the end of the night, the last spectra are affected by solar He I emission. Although we corrected the emission line, some residuals still persisted. Then, we decided to mask the affected spectral range only on particular spectra. The He I residual map and TS are shown in Fig. A.13, and do not show clear evidences of He I absorption. We placed a 3σ upper limit to the He I triplet excess absorption of ~ 0.5 %.

3.15. TOI-1268 b

The transit of TOI-1268 b on the 24 of February 2023 was only followed spectroscopically by GIANO-B, and we missed the information about H α , and the stellar variability or activity from the visible wavelength range covered by HARPS-N. MuSCAT2 covered the same transit photometrically with the exposure times initially set to $g = 5$ s, $r = 10$ s, $i = 10$ s, and $z_s = 15$ s and later modified to $g = 5$ s, $r = 10$ s, $i = 8$ s, and $z_s = 12$ s to avoid the saturation of the target star. Our MuSCAT2 transit fit has a central time of $T_c = 2460000.66841 \pm 0.00014$ BJD.

The four bands of the MuSCAT2 photometry do not show the presence of strong stellar activity or the planet crossing in front of any big starspot(s). Moreover, the Pa- β , Pa- γ , and Pa- δ lines are mainly flat with no correlation with the stellar He I line. Because our observations ended close to the twilight, our last spectra are affected by He I sunlight contamination. Because this kind of emission increases quickly between exposures as the observations are approaching the twilight, it is not well corrected

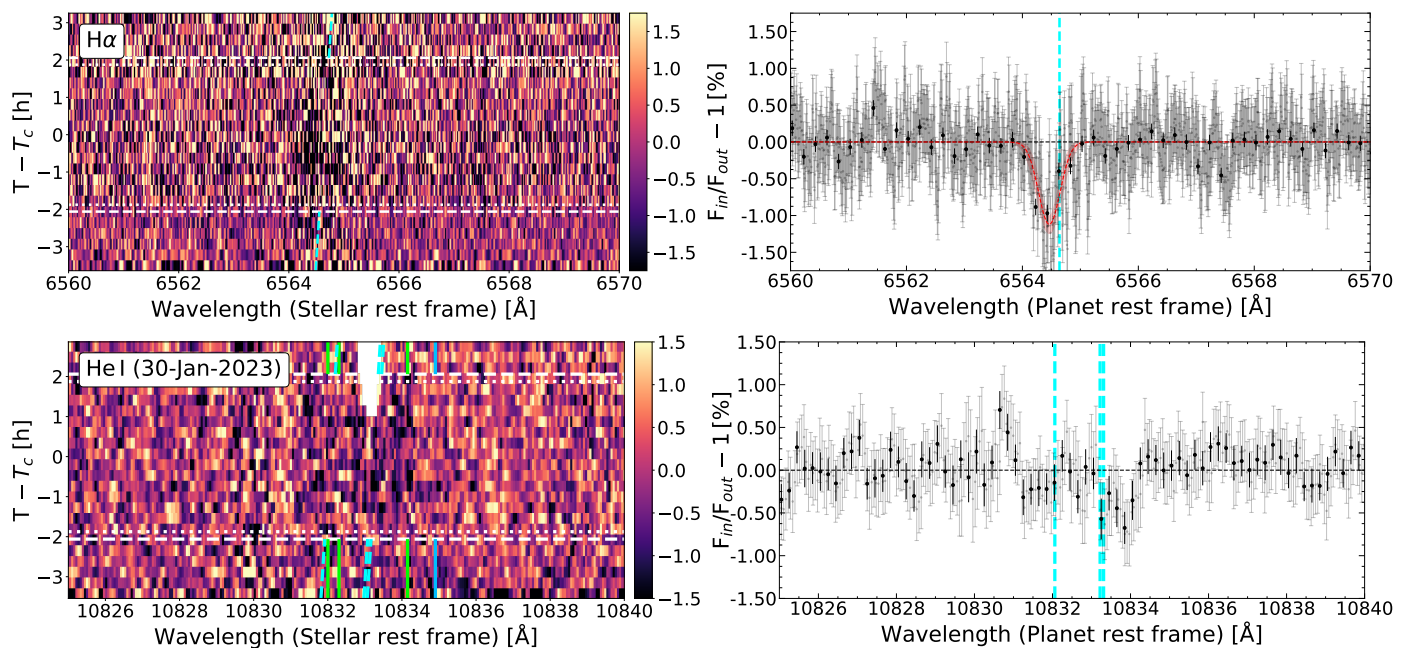


Fig. 2: Same as Fig. 1, but for TOI-1136 d. $H\alpha$ results (top panels) are the combination of HARPS-N and CARMENES VIS observations. He I triplet results (bottom panels) are from CARMENES NIR observations.

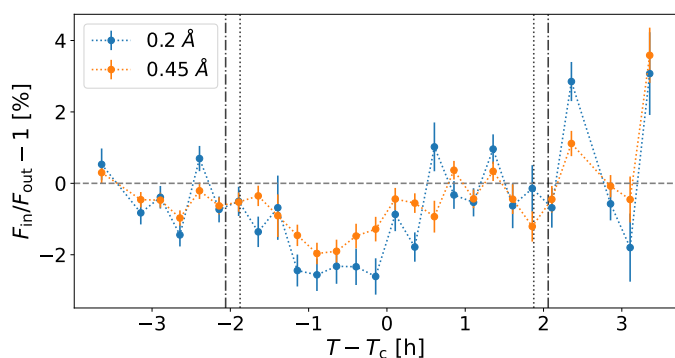


Fig. 3: Transit light curve of $H\alpha$ line from the combined observations of TOI-1136 d. The $H\alpha$ light curve was constructed integrating the counts of the residual map in the planet rest frame around λ_0 using σ (blue) and FWHM (orange) wavelength band passes from Table H.1. The vertical lines represent the different contacts during the transit.

by the ABAB procedure. We decided to mask those regions affected by the He I emission only in the selected spectra.

The residual map and TS are shown in Fig. 4, where the residual map shows an absorption region at the expected position of the planetary trace. The signal is well detected in the residual map and the TS, where we fitted a blue-shifted absorption of $-2.00^{+0.15}_{-0.16}$ % (EW = 19.1 ± 1.9 mÅ). Table I.1 presents the priors and posteriors, and Fig. I.2 shows the posterior distributions. These high-resolution spectroscopy results confirm the He I detection using narrow-band photometry from Pérez-González et al. (2024). We also constructed the He I triplet transit light curve, shown in Fig. 5. The absorption seems to extend further than the end of the white light transit hinting an He tail, that needs to be confirmed in further observations.

3.16. TOI-2076 b

In this section we present the analyses and results from one CARMENES transit of TOI-2076 b observed in 2023. Previously in May 2022, we missed a transit of TOI-2076 c due to imprecise ephemerides from Hedges et al. (2021). Nowadays, the periods of TOI-2076 planets are well-constrained and refined (Osborn et al. 2022; Zhang et al. 2023b), and we could confirm that none of the three planets were transiting the night of 11 May 2022. However, we take advantage of those observations to study the behaviour of the star between epochs. The values derived from the several activity indicators for the two datasets are consistent, and there are no differences between epochs. The levels of stellar activity of both visits are very similar and TOI-2076 b transit seems unaffected by stellar activity or variability. Due to bad weather conditions at the beginning of the night of 13 April 2023, we missed the pre-transit baseline and a very small part of the transit. Moreover, the median S/N of the in-transit spectra is lower (~ 60) than after transit (~ 90).

The TTVs of the TOI-2076 system (Osborn et al. 2022) make the scheduling of its transits complicated and increase the probability of missing part of them. Thus, we complemented our observations on 2023 with a photometric follow-up. We could not perform simultaneous observations on 13 April 2023, but we detected TOI-2076 b ingress one month after (14 May 2023). The details of the photometric analysis and their results are explained in App. J.

The $H\alpha$ residual map and TS are shown in Fig. A.14. The TS close to the $H\alpha$ has consistently negative values that could be considered as a planetary absorption. Although the lack of pre-transit baseline could be the origin of the signal, as for HD 63433 b transit on 1 November 2021 (Sect. 3.6). Then, a full transit coverage is needed to confirm this tentative signal. We set a 3σ upper limit of 0.7% to $H\alpha$ exoplanet absorption.

The He I triplet residual map and TS are shown in Fig. A.14. We do not detect clear evidences of He I planetary absorption. We looked for correlations of the He I NIR line with the He I D3

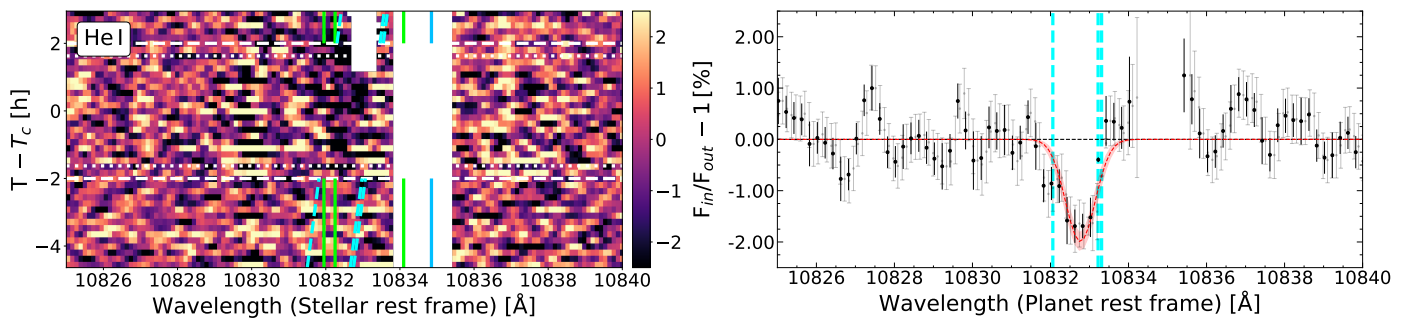


Fig. 4: Same as Fig. 1, but for TOI-1268 b He I triplet observations with GIANO-B.

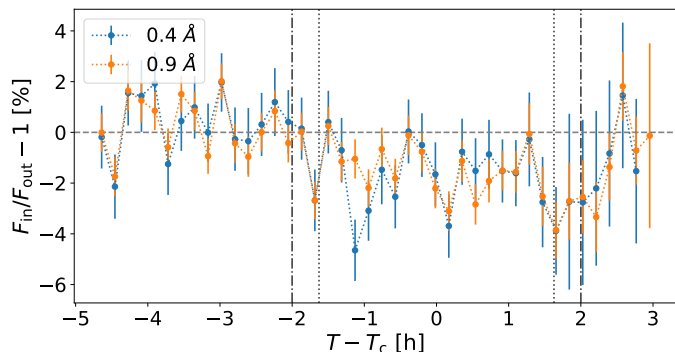


Fig. 5: Transit light curve of He I triplet from TOI-1268 b detection. The He I light curve was constructed integrating the counts of the residual map in the planet rest frame around λ_0 using σ (blue) and FWHM (orange) wavelength band passes from Table I.1. The vertical lines represent the different contacts during the transit.

(5877.2 Å), and H Paschen lines, with no conclusive results. We could only put a 3σ upper limit of $\sim 1\%$ for any He I triplet planetary absorption.

TOI-2076 b atmosphere was already targeted looking for He I. The same partial transit was observed from the same mountain with two different 8-m telescopes with their high-resolution spectrographs. In both cases, a consistent feature was detected but there are differences in the interpretation of the signal. Zhang et al. (2023b) with Keck/NIRSPEC reported a He I detection with an excess absorption of $1.01 \pm 0.05\%$ ($EW = 10.0 \pm 0.7$). On the other hand, Gaidos et al. (2023) fitted a significant excess EW of $8.5 \pm 1.4 \text{ m}\text{\AA}$, but their analyses did not rule out the stellar origin of the signal. Although CARMENES has the capability to detect such He I excess absorptions (e.g. Salz et al. 2018; Alonso-Floriano et al. 2019; Orell-Miquel et al. 2023), the S/N of our transit only allows us to put an upper limit at $\sim 1\%$, which is at the same level of the previous detected feature. Further observations in good weather conditions are needed to firmly confirm the TOI-2076 b He I signal. For the purpose of this work, we use the positive results from Zhang et al. (2023b) in the discussion.

We also used the dataset from May 2022 to check for H/He structures around TOI-2076, recently reported in other exoplanets (Zhang et al. 2023c; Gully-Santiago et al. 2024). However, we obtained very similar results when we included those spectra in the analyses of TOI-2076 b H α and He I lines.

3.17. TOI-1683 b

We scheduled three transits of TOI-1683 b for the MOPYS project, one with CARMENES and two with GIARPS. CARMENES transit was stopped due to bad weather and the few taken spectra are useless for atmospheric analyses. The two other transits were observed only with GIANO-B due to problems with the GIARPS mode, and we could not observe until ingress for the first GIANO-B visit (19 September 2023).

Zhang et al. (2023b) reported an age of 500 ± 150 Myr, based on gyrochronology relations. Here, we derived a new age estimation of $2^{+1.3}_{-0.9}$ Gyr based on gyrochronology, stellar kinematics, and stellar Li I analyses, indicating that TOI-1683 is not a young star. Hence, we do not consider TOI-1683 b as a young planet. The details of our stellar age analyses are explained in Appendix K. Furthermore, we derived new ephemerides for TOI-1683 b using the available TESS data from Sectors 19, 43, and 44 in the MAST archive. The photometric analyses and results are shown in Appendix K as well.

Zhang et al. (2023b) observed one transit in bad weather conditions with Keck/NIRSPEC, and reported a He I detection of $0.84 \pm 0.17\%$. Although we also observe in poor weather and seeing conditions, we do not detect a significant He I excess absorption in the individual or combined nights from GIANO-B. The residual maps and TS from the individual and combined nights are shown in Fig. A.15. We placed a 3σ upper limit from our two visits with GIANO-B to the He I excess absorption of 0.7% , which is $\sim 1\sigma$ consistent with Zhang et al. (2023b) detection. We use the positive detection from Zhang et al. (2023b) in the discussion.

3.18. WASP-189 b

Stangret et al. (2022) already analysed one HARPS-N and two HARPS observations finding a H α absorption feature of $-0.13 \pm 0.02\%$. However, because the line was affected by the RM effect, they were cautious claiming a detection. Here, we inspected the GIANO-B data taken simultaneously to those HARPS-N observations.

The Si I and He I stellar lines are not detectable in the spectra and the only visible spectral features are the H $_2$ O telluric absorption lines, which we masked in the residual map and TS, shown in Fig. A.16. Although the TS has some structure, there is no evidence of He I triplet absorption. We set a 3σ upper limit of 0.3% to the He I absorption on WASP-189 b.

3.19. HAT-P-57 b

HAT-P-57 b is an ‘adolescent’ planet ($1.00^{+0.67}_{-0.51}$ Gyr; Hartman et al. 2015), where Stangret et al. (2022) found an H α absorption feature (-0.7 ± 0.2 %). However, the signal is narrow compared to other H α detections from the literature and it is surrounded by pulsations from the host star.

We analysed one archival CARMENES NIR transit to inspect the He I triplet. Although we masked some regions of strong tellurics, the residual map and TS in Fig. A.17 do not show any significant planetary absorption signal. We set a 3σ upper limit of 1 % to the planetary He I absorption.

3.20. TOI-2018 b

The planet candidate TOI-2018 b was initially alerted to the community as a ‘young planet’, but final analyses of its age were ambiguous and it was not possible to confirm an age below 1 Gyr ($2.4^{+0.8}_{-0.2}$; Dai et al. 2023b). Although we can not include TOI-2018 b in our sample of young planets, the results obtained from two partial transits observed with GIARPS deserve to be included in this work.

The GIARPS transit on the night of 15 June 2023 was photometrically followed with MuSCAT2, observing the transit in four bands with the exposure times set to $g=15$ s, $r=15$ s, $i=10$ s, and $z_s=10$ s. Our MuSCAT2 transit fit found a central time of $T_c = 2459746.4287 \pm 0.0021$ BJD, confirming that we missed partially the transits in both visits.

The H α residual map and TS from the individual nights and their combination are shown in Figures A.18 and 6, respectively. The TS is flat, and the 3σ upper limit for H α excess absorption is set to 1.5 %.

The He I triplet residual map and TS from the individual nights and their combination are shown in Figures A.19 and 6, respectively. Although the quality of the two nights is different, the results of both nights are consistent within 2σ , and we detect a consistent excess absorption of ~ 1 % at the expected position of the planetary He I signal. When we combine both nights, we confirm the detection of a red-shifted He I absorption of $-1.02^{+0.19}_{-0.22}$ % (EW = 7.8 ± 1.5 mÅ). All the nested sampling material for the individual and combined datasets is shown in App. L. The He I triplet transit light curve (Figure 7) shows an absorption signal consistent with the transit duration, with no evidence of an extended He signal. Although the He I signal is consistent and well detected in the two partial transits, a full transit observation will help to confirm our detection and the study of TOI-2018 b atmospheric evaporation.

4. Additional literature evaporation tracers observations

4.1. Young planets from the literature

In the framework of the MOPYS project, we adopted the 1 Gyr stellar age as the threshold to classify exoplanets as young (≤ 1 Gyr) or old (≥ 1 Gyr). We used this nomenclature in the discussion in Section 6. The 1 Gyr threshold is mainly based on the core-powered evaporation timescale, which is longer than the strong photo-evaporation initial stage (X-ray driven).

Young exoplanets are an interesting population that have called the attention of different research groups. To put the young planet results obtained in this work into context, we inspected

the ExoAtmospheres⁵ database looking for other young exoatmospheric analyses. Table 3 presents a compilation of literature high-resolution spectroscopy studies of young transiting exoplanet atmospheres targeting the H α or the He I triplet.⁶ Here, we give a short context to those observations from the literature included in Table 3.

KELT-9 b: As the hottest exoplanet known to date, this planet attracted attention to probe and investigate its extreme atmosphere. Yan & Henning (2018) detected an evaporating exosphere of H α . However, Nortmann et al. (2018, see supplementary material section therein) could only place an upper limit to the He I triplet absorption.

K2-25 b: The He I triplet was observed using the IRD spectrograph, although the transit was contaminated by telluric OH emission. Gaidos et al. (2020b) reported a 99% confidence upper limit to the transit-associated EW of 17 mÅ.

AU Mic b: Due to the host star’s youth, the H α observations with ESPRESSO were strongly affected by stellar activity, making it impossible to set an upper limit (Palle et al. 2020b). Recently, Rockcliffe et al. (2023) reported a Ly α detection but only in one of the two visits with HST/STIS. IRD and Keck/NIRSPEC spectrographs obtained a 99% confidence upper limit to the He I EW of 4.4 and 3.7 mÅ, respectively (Hirano et al. 2020). Allart et al. (2023) observed one transit with SPIRou spectrograph finding a significant He I absorption feature (0.37 ± 0.09 %). However, the authors finally reported a conservative 3σ upper limit of 0.26 %, consistent with previous observations.

K2-136 c: Gaidos et al. (2021) put a 99% confidence upper limit to the He I triplet EW of 25 mÅ with one transit observed with the IRD spectrograph. The He I lines position in between the telluric OH emission and H₂O absorption lines complicated the calculation of the transmission spectra.

DS Tuc b: The H α was analysed with ESPRESSO and HARPS spectrographs observations. However, the transits were affected by stellar activity and an H α upper limit could not be set (Benatti et al. 2021).

V1298 Tau system: This 20-Myr old multi-planet system has seen different attempts to study the presence of He I in their planetary atmospheres. Gaidos et al. (2022) used the IRD spectrograph to observe, during different nights, the star alone and a transit of planet b. An increasing He I absorption was detected during the transit, but the authors proposed other explanations besides the planetary absorption. Using the narrowband helium filter technique, Vissapragada et al. (2021) observed the transits of planets b and d. For planet b they do not require extra absorption to explain the flux decrease, while they found a tentative excess absorption combining two partial transits of planet d, but it requires a significant transit time variation.

WASP-52 b: The planet was observed with ESPRESSO detecting H α , and other atomic species as well (Chen et al. 2020). The presence of He I in its atmosphere has been studied, first with a tentative detection using narrow-band photometry (Vissapragada et al. 2020, 2022a) and later confirmed with the Keck/NIRSPEC spectrograph (Kirk et al. 2022). However, a recent paper by Allart et al. (2023) did not find He I absorption in two visits with the SPIRou spectrograph, and derived a 3σ upper limit of 1.69 %.

⁵ <http://research.iac.es/proyecto/exoatmospheres/index.php>

⁶ We also acknowledge the He I observations of K2-33 b (Hirano et al. 2024), which appeared during the peer review process of the manuscript.

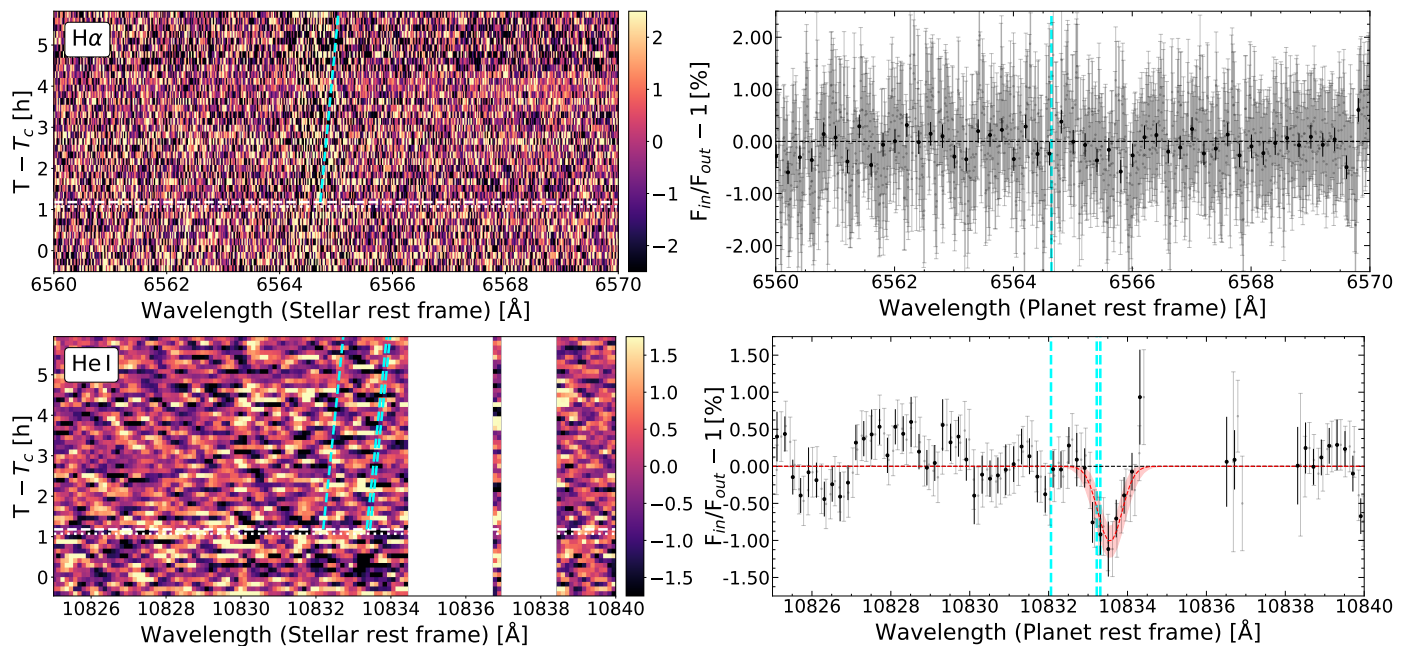


Fig. 6: Same as Fig. 1, but for TOI-2018 b combined observations of $H\alpha$ with HARPS-N and He I triplet with GIANO-B.

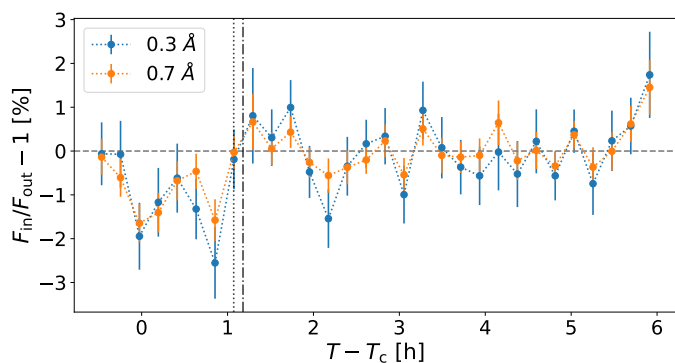


Fig. 7: Transit light curve of He I triplet from the combined nights of TOI-2018 b. The He I light curve was constructed integrating the counts of the residual map in the planet rest frame around λ_0 using σ (blue) and FWHM (orange) wavelength band passes from Table L.3. The vertical lines represent the different contacts during the observation.

HAT-P-70 b: The atmosphere of this ultra-hot Jupiter was inspected by [Bello-Arufe et al. \(2022\)](#) using HARPS-N. They detected absorption coming from the $H\alpha$, $H\beta$, and $H\gamma$ lines, and many other atomic and molecular species as well.

WASP-80 b: Its atmosphere has been targeted in search of He I absorption but without success ([Fossati et al. 2022](#); [Al-lart et al. 2023](#)). [Salz et al. \(2015\)](#) is the only reference which provides a formerly calculated age of <200 Myr. However, the observed X-ray luminosity ($\log L_X \sim 27.8 \text{ erg s}^{-1}$ in [Salz et al. 2015](#), down to 27.5 erg s^{-1} in [Sanz-Forcada et al. in prep.](#)) yields a $\log L_X/L_{\text{bol}} \sim -5.0$, implying an age of ~ 3 Gyr using [Sanz-Forcada et al. \(2011\)](#) age- L_X relations. Moreover, the TESS light curve do not suggest a rotational period of $\lesssim 15$ d. Therefore, WASP-80 is probably older than 1 Gyr according to the gyrochronology method shown in Figure K.3 ($G - J = 2.05$).

4.2. Older planets from the literature

To put in context the young exoplanet He I (planets with ages $\lesssim 1$ Gyr) findings, we complemented them with old exoplanet high-resolution He I observations (planets with age $\gtrsim 1$ Gyr) from the literature. We have compiled a He I triplet database, detailed in Table M.1, which we constructed using the ExoAtmospheres database and literature results. For consistency, we only considered He I triplet results from high-resolution spectrographs. That is, the narrow-band photometry detections of HAT-P-26 b ([Vissapragada et al. 2022b](#)) and TOI-1420 b ([Vissapragada et al. 2024a](#)) were not included.⁷ Although we analysed the $H\alpha$ and we cited some results on the $Ly\alpha$ as well, Table M.1 only reports the H ($H\alpha$ or $Ly\alpha$) observations for the planets with He I triplet observations, except for the young hot Jupiter HAT-P-70 b with $H\alpha$ detection ([Bello-Arufe et al. 2022](#)). The young Neptune DS Tuc b is not included in Table M.1 because no upper limit could be set from $H\alpha$ observations ([Benatti et al. 2021](#)) and no He I triplet observations could be found in the literature.

Given the number of planets and details of each observation, we do not discuss the planets individually here. We refer to Table M.1 and the appropriate references.

4.3. A note on He I variability

The planetary He I triplet is known to show variability in its strength but also in its detectability (e.g. [Palle et al. 2020a](#); [Zhang et al. 2022a](#)). In this work, we presented two upper limits for TOI-2076 b and TOI-1683 b, for which [Zhang et al. \(2023b\)](#) reported He I detections. Our upper limits are consistent at 1σ with [Zhang et al. \(2023b\)](#) detections. Thus, He I triplet variability may be one reason for our absence of planetary signals. Variability was also invoked by [Orell-Miquel et al. \(2023\)](#) to explain the $\sim 2\sigma$ deeper absorption found in HD 235088 b. We note that [Gaidos et al. \(2023\)](#) derived non-conclusive results for TOI-2076 b

⁷ We also acknowledge the He I observations of TOI-1259A b ([Saidel et al. 2024](#)), which appeared during the peer review process of the manuscript.

Table 3: Compilation of H α and He I observations from high-resolution spectroscopy facilities of young (≤ 1 Gyr) transiting exoplanets, from the literature and this work (Sect. 3). A cross (\times) indicates when the stellar activity prevented to measure any planetary absorption or derive upper limits.

| Planet | H α [%] | He I [%] | Planet | H α [%] | He I [%] |
|---------------------------|---------------------------------|--|---------------------------|--|--|
| MASCARA-2 b | 0.85 \pm 0.03 ⁽¹⁾ | <0.5 | TOI-2046 b | <5 | <2.4 |
| K2-100 b | <1.4 | <1.3 ≤ 1.2 ⁽²⁾ | TOI-1807 b | <0.95 | <0.80 ≤ 0.4 ⁽⁸⁾ |
| TOI-1431 b | <0.33 ⁽³⁾ | <0.4 | TOI-2048 b | <1.5 | <1.0 |
| HD 63433 b | <0.4 | <0.4 ≤ 0.5 ⁽⁴⁾ | HD 63433 c | <0.4 – | <0.4 ≤ 0.5 ⁽⁴⁾ |
| HD 73583 b | ≤ 0.5 | 0.72 \pm 0.08 ^(5,6) | HD 73583 c | ≤ 0.5 | <0.5 |
| HD 235088 b | \times ⁽⁷⁾ | 0.91 \pm 0.11 ⁽⁷⁾ 0.64 \pm 0.06 ⁽⁶⁾ | TOI-2076 b | <0.7 | ≤ 1 1.01 \pm 0.05 ⁽⁶⁾ |
| V1298 Tau b | – | ≤ 1.7 ⁽²⁰⁾ | V1298 Tau c | <1.1 | <3.7 |
| TOI-1268 b | – | 2.00 ^{+0.15} _{-0.16} | TOI-1136 d | 1.12 ^{+0.12} _{-0.13} | <0.5 |
| WASP-189 b | 0.13 \pm 0.02 ⁽⁹⁾ | <0.3 | HAT-P-57 b | <0.7 \pm 0.2 ⁽⁹⁾ | <1 |
| K2-77 b | <2.5 | <2.7 | K2-25 b | – | <1.7 ⁽¹²⁾ |
| AU Mic b | \times ⁽¹³⁾ | <0.34 ⁽¹⁴⁾ | K2-136 c | – | <2.3 ⁽¹⁵⁾ |
| DS Tuc b | \times ⁽¹⁶⁾ | – | WASP-52 b | 0.86 \pm 0.13 ⁽¹⁷⁾ | 3.44 \pm 0.31 ⁽¹⁸⁾ |
| HAT-P-70 b | 1.56 \pm 0.15 ⁽¹⁹⁾ | – | WASP-80 b | – | <0.85 ⁽²¹⁾ |
| KELT-9 b | 1.15 \pm 0.05 ⁽¹⁰⁾ | <0.33 ⁽¹¹⁾ | | | |
| TOI-2018 b ^(†) | <1.5 | 1.02 ^{+0.19} _{-0.22} | TOI-1683 b ^(†) | – | <0.7 0.84 \pm 0.17 ⁽⁶⁾ |

References. ⁽¹⁾ Casasayas-Barris et al. (2019), ⁽²⁾ EW at 99% confidence of 5.7 mÅ (Gaidos et al. 2020a), ⁽³⁾ Stangret et al. (2021), ⁽⁴⁾ Zhang et al. (2022c), ⁽⁵⁾ Zhang et al. (2022b), ⁽⁶⁾ Zhang et al. (2023b), ⁽⁷⁾ Orell-Miquel et al. (2023), ⁽⁸⁾ EW at 99% confidence of 4 mÅ (Gaidos et al. 2023), ⁽⁹⁾ Stangret et al. (2022), ⁽¹⁰⁾ Yan & Henning (2018), ⁽¹¹⁾ Nortmann et al. (2018), ⁽¹²⁾ EW at 99% confidence of 17 mÅ (Gaidos et al. 2020b), ⁽¹³⁾ Palle et al. (2020b), ⁽¹⁴⁾ EW at 99% confidence of 3.7 mÅ (Hirano et al. 2020), ⁽¹⁵⁾ EW at 99% confidence of 25 mÅ (Gaidos et al. 2021), ⁽¹⁶⁾ Benatti et al. (2021), ⁽¹⁷⁾ Chen et al. (2020), ⁽¹⁸⁾ Kirk et al. (2022), ⁽¹⁹⁾ Bello-Arufe et al. (2022), ⁽²⁰⁾ Gaidos et al. (2022), ⁽²¹⁾ Fossati et al. (2022)

Notes. ^(†) TOI-2018 b and TOI-1683 b are included in the table, but they are likely not young planets.

He I signal, and TOI-1683 b transit from Zhang et al. (2023b) was performed in poor observing conditions. We want to stress the importance of re-observing targets as a sanity check to confirm previous results (detections or upper limits), but also to study the planetary He I triplet variability.

On the other hand, Krolikowski et al. (2024) analysed the variability of the He I triplet of young stars. In particular, V1298 Tau, K2-100, K2-136, K2-77, HD 63433, and TOI-2048 were in the list of observed stars. They found that young stars show higher variability, with V1298 Tau being extremely variable, which could explain the non-conclusive results from the He I observations. The stellar He I variability decreases rapidly and keeps constant for stars older than ~ 300 Myr (Krolikowski et al. 2024). Although the stellar He I triplet line is variable, the short-term variability might not have a significant impact on the transit observations performed during the same night (Fuhrmeister et al. 2020; Krolikowski et al. 2024). In fact, H α is more sensitive to stellar variability than the He I triplet (Fuhrmeister et al. 2020) and the analyses of those lines on AU Mic b and DS Tuc b are good examples (Palle et al. 2020b; Hirano et al. 2020; Benatti et al. 2021).

5. Criteria for detections, non-detections, and non-conclusive measurements

A problem we encountered when studying the He I signal (and H α as well) was how to deal with the observations where only an upper limit value is given, which are the majority of the cases (52 of 69 in Table M.1). In this work, we classified the upper limit measurements in two groups: *a)* non-conclusive measurements (i.e. the upper limit value is large, and it does not actually constrain the presence of the atom in the exoplanet atmosphere) and *b)* non-detection (i.e. the upper limit value is low enough to confidently assume there is no significant presence of that atom in the exoplanet atmosphere).

To assign observations to either category, for the He observations, we used the relationship that the observed and theoretical mass-loss rates (\dot{m}_{obs} and \dot{m}_{theory} , respectively) seem to follow, represented in Figure 8. We present \dot{m}_{obs} and \dot{m}_{theory} equations in Sect. 6.3, and we further explore and discuss the trend in that section. For the time being, the fitted line between $\dot{m}_{\text{obs}}-\dot{m}_{\text{theory}}$ seems to account for the differences between planetary characteristics, and populations (Vissapragada et al. 2022b; Zhang et al. 2023a, and Sect. 6.3). Therefore, we consider that relation

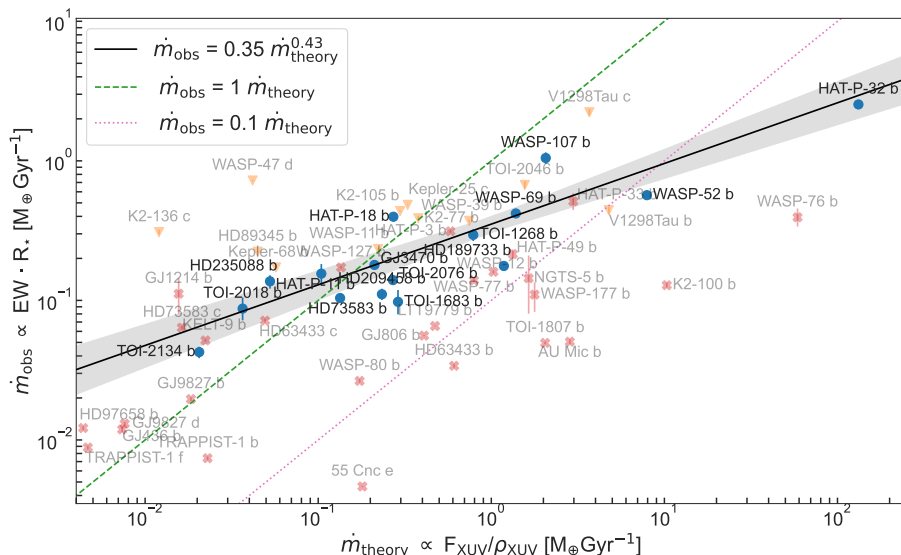


Fig. 8. Relationship between the observed (\dot{m}_{obs}) and the theoretical (\dot{m}_{theory}) energy-limited mass-loss rates. We define XUV until the He I ionisation range ($\lambda = 5 - 504 \text{ \AA}$). The black line indicates the fitted relationship (shown in the legend) and the shaded area the 1σ uncertainty. He I observations are coded as blue circles for detections, red crosses for non-detections, orange down-pointing triangles for non-conclusive. We did not plot the error bars of \dot{m}_{theory} due to the very large uncertainties associated with the F_{XUV} values and its calculation. Every planet has its name labelled: in black for detections and the others in grey. The two new detections presented in this work, TOI-2018 b and TOI-1268 b, are in good agreement with the predicted trend.

to classify the He I upper limits. Although other criteria might be chosen, it is used consistently for the whole sample.

We computed the \dot{m}_{obs} upper limits from the He I EW upper limit values. If the \dot{m}_{obs} upper limit falls above the fitted line, the \dot{m}_{obs} upper limit value is higher than the a priori expected signal, and so it is not constrained. Thus, we refer to those measurements as non-conclusive (orange down-pointing triangles in Fig. 8). On the other side, the \dot{m}_{obs} upper limits falling below the line can be considered as non-detections (red crosses in Fig. 8). We also considered as non-detections the \dot{m}_{obs} upper limits that fall within 1σ of the fit (grey shaded area in Fig. 8).

We note that F_{XUV} is unknown for some of the exoplanets in our sample. For those planets with no measured F_{XUV} , we performed a similar procedure but in a $1/\rho_{\text{XUV}}$ versus \dot{m}_{obs} diagram (not shown), which is a proxy for \dot{m}_{theory} versus $\dot{m}_{\text{obs}} \cdot \rho_{\text{XUV}}$ is the planet density when considering as the radius its XUV radius, which is different from the planet density ρ_{p} (see Sect. 6.3).

We did some exceptions when classifying some He I observations. GJ 1214 b: we re-classified as a non-detection the tentative He I signal reported by Orell-Miquel et al. (2022) due to other upper limits reported in the literature (Petit dit de la Roche et al. 2020; Kasper et al. 2020; Spake et al. 2022; Allart et al. 2023). V1298 Tau b: because of the unclear origin of the signal detected by Gaidos et al. (2022), we set this observation as non-conclusive. V1298 Tau c is in the same situation as planet b, and its He I upper limit is non-conclusive. Moreover, the measurements for the V1298 Tau planets are consistent with the stellar He I line variability range derived for their host star (Krolkowski et al. 2024). WASP-76 b: its He I feature was presented as upper limit in Casasayas-Barris et al. (2021a) but here we consider it as a non-detection due to the planet position well below the $\dot{m}_{\text{obs}} - \dot{m}_{\text{theory}}$ line.

For H α , we simply considered the upper limits as non-detections. However, if the H α upper limit absorption is comparable to that of He I, we used the He I classification for both measurements. We only considered few Ly α detections for some particular exoplanets. The classification and nomenclature described in this section (detection, non-detection, and non-conclusive) is used all across the manuscript.

We note that absorption measurements of the three lines (Ly α , H α , and He I triplet) would be the ideal case to determine whether an exoplanet is undergoing strong atmospheric escape. However, these observations are not available for all targets,

and may be hard (even impossible) to obtain for some individual stars (e.g. Ly α interstellar medium extinction, H α variability in active stars, or low He I triplet population). When possible, we consider the results from the three lines to determine atmospheric escape detections.

6. Discussion

We have organised the discussion of our results in the following manner: Section 6.1 gives a general view of the evaporation tracers across stellar age, planet radius, period, and mass. In Sect. 6.2 we constrain the cosmic shoreline from He I detections. In Section 6.3 we explore the relation between He I detections and the energy-limited mass-loss rates. Finally, we explore further relations between He I detections and different planet and stellar properties in Sections 6.4, 6.5, and 6.6.

6.1. Evaporation tracers of planetary atmospheres across stellar age

Figure 9 displays the planetary radius versus stellar age, with the planets colour-coded according to their evaporation measurements. We considered the He I triplet and/or H α absorption detections (and Ly α in some particular cases) as proxies of evaporation signs. Thus, an evaporation detection means that either He I or H α or both have been positively detected.

Figure 10 is similar to Figure 9 but focuses only on the He I triplet, and presents a comparison between the He I EW signals and the stellar age. The planets are marked and colour-coded according to their He I results. Allart et al. (2023) reported that a trend between He I and stellar age was noticeable in their sample of eleven planets, however the authors refrained from further conclusions due to their small sample size and the lack of precise stellar ages. Although in this work we used a larger sample (18 young and 35 old planets, including detections and non-detections, but less homogeneous than the Allart et al. 2023 one), we do not notice a clear correlation between He I EW and stellar age.

The first 100 Myr are critical for the planetary atmospheric evolution, according to photo-evaporation models (see Introduction in Sect. 1). Unfortunately, there are only a few planets in Figures 9 and 10 with ages ≤ 100 Myr. The youngest objects have ages of ~ 20 Myr (AUMic b and V1298 Tau c & b) and

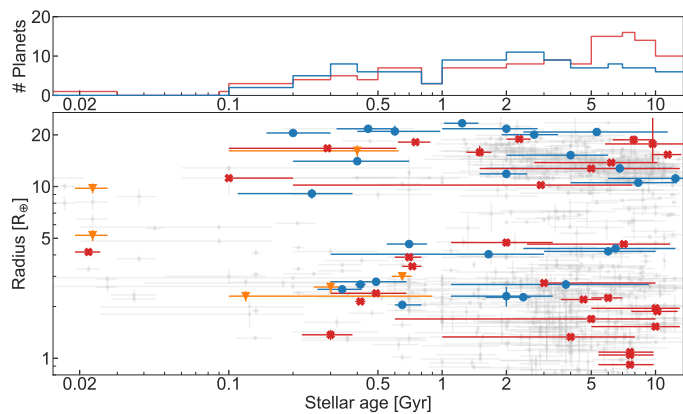


Fig. 9: Planetary radius vs stellar age diagram of evaporation (H and He I) detections (blue circles), non-detections (red crosses), and non-conclusive observations (orange down-pointing triangles). Planetary radii and stellar ages are from Table M.1. The top panel shows the summed histogram of evaporation detections (blue line) and non-detections (red line) across stellar age. The grey points represent all known planets with radius and age determined with precision better than 30% and 50%, respectively (data from NASA Exoplanet Archive).

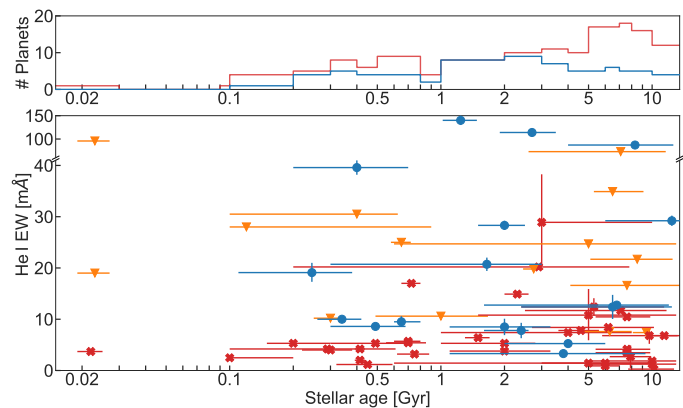


Fig. 10: Equivalent width (EW) of He I detections (blue circles), non-detections (red crosses), and non-conclusive observations (orange down-pointing triangles) as functions of stellar age. The top panel shows the summed histogram of He I detections (blue line) and non-detections (red line) across stellar age bins.

then there is a lack of He I and H α observations until ~ 100 Myr (WASP-80 b, and K2-77 b). WASP-80 b, with a formerly calculated age of <200 Myr (Salz et al. 2015), has no detection of He I triplet. However, a possible older age of WASP-80 (see Section 4.1) and the calculated $\log L_{\text{XUV}}$ at the planet separation (Table M.1) could explain the lack of detection of the He I triplet. AU Mic b non-detection is harder to reconcile, but different scenarios can be invoked (e.g. stellar activity masking possible detections or H/He ratio). He I and H α observations of V1298 Tau b & c resulted in non-conclusive measurements, mainly due to the strong stellar activity levels of the young host star. However, the masses derived for planets b and c indicate that their densities are similar to older planets, suggesting they are not inflated and that they contracted faster than expected (Suárez Mascareño et al. 2021).

While the non-detections of WASP-80 b, AU Mic b, V1298 Tau b & c do not seem to fit the predictions from

photo-evaporation models (Lopez et al. 2012; Owen & Jackson 2012; Owen & Wu 2013, 2017; Owen & Lai 2018; Dawson & Johnson 2018), the sample of ≤ 100 Myr-old planets is too small to draw conclusions. A larger sample of ≤ 150 -Myr-old planets is needed to explore the photo-evaporation timescales.

From Fig. 9 and 10, the youngest planet with He I detection is TOI-1268 b (245 ± 135 Myr), and the youngest planet with H α detection is MASCARA-2 b (200^{+100}_{-50} Myr). The number of planets with evaporation detections increases until peaking at ~ 2 Gyr, and then it is roughly constant, but this is related to the age distribution in our sample. The proportion between detections and non-detections remains constant (within error bars) with age, except at old ages (>5 Gyr) when non-detections dominate (see Figs. 9, and 10). This non-detections domination is more pronounced when considering only the He I observations (Fig. 10), and extended over all stellar ages, except over the 1–3 Gyr range.

Our results on evaporation timescales agree with the conclusions from Loyd et al. (2020) on the radius gap, and Christiansen et al. (2023) on the hot Neptune population (see Fig. 6 in their work), and photo-evaporation mechanism is not more supported than the core-powered one. The fact that we do not see a decrease in the evaporation tracers, until very old ages (~ 5 Gyr, see Figs. 9, and 10), might be marginally more consistent with the core-powered timescale of Gyr (Ginzburg et al. 2016, 2018; Gupta & Schlichting 2020).

6.1.1. Radius–period diagram across stellar age

Figure 11 compares the population of young (≤ 1 Gyr, top panels) and old (>1 Gyr, bottom panels) planets in a radius–period diagrams for only He I triplet observations, only H (mainly H α with few Ly α) observations, and both evaporation proxies. Figures 9, 10, and 11 show no clear differences for the evaporation of the gas giant planets before and after 1 Gyr. The detections of evaporation are evenly spread over the stellar ages, with more preference of H α detection than from He I for the young gas giants. We note that there are no evaporation detections of young and old planets below the radius gap or for Earth-like planets, supporting rocky planets are not under extreme atmospheric mass-loss processes, at least after ~ 300 Myr which is the age of the youngest rocky planet in our dataset (TOI-1807 b).

Allan et al. (2024) simulated how the He I triplet planetary signal from a highly irradiated ($a_p = 0.045$ AU) gas giant planet ($M_p = 0.3 M_J$) around a K-dwarf star changes with the stellar age. They assumed a typical H/He ratio of 98/2 (Lampón et al. 2020, 2021b; Orell-Miquel et al. 2023). From their simulations, they derive excess absorption peaks of 4–7 % for young (16–550 Myr) Hot Jupiters, while at 5 Gyr the excess absorption would be of $\sim 1.5\%$. They state that a close-in ($a_p < 0.1$ AU) planet with a radius of 1–2 R_J transiting a <150 -Myr-old K dwarf star would be the best target to test their evolution models. Although the He I triplet detection is favoured by the extreme radiation in XUV range ($\lambda < 504$ nm; Sanz-Forcada & Dupree 2008) and the TS simulations from Allan et al. (2024), none of the three 20-Myr-old planets analysed here present a clear detection of He I. WASP-80 b ($a_p = 0.035$ AU, $R_p = 1 R_J$, $M_p = 0.5 M_J$, <200 Myr, spectral type $\sim K7V$) is the closest planet from Table M.1 to the simulated one in Allan et al. (2024) but it has very low He I upper limits (Fossati et al. 2022; Allart et al. 2023). WASP-52 b might be in agreement with the simulations, although the largest He I excess absorptions to date come from older planets (e.g. HAT-P-67 b, Gully-Santiago et al. 2024; HAT-P-32 b, Czesla et al. 2022; and WASP-107 b, Kirk et al. 2020). In Fig. 11 WASP-52 b is the only young gas giant planet with a He I

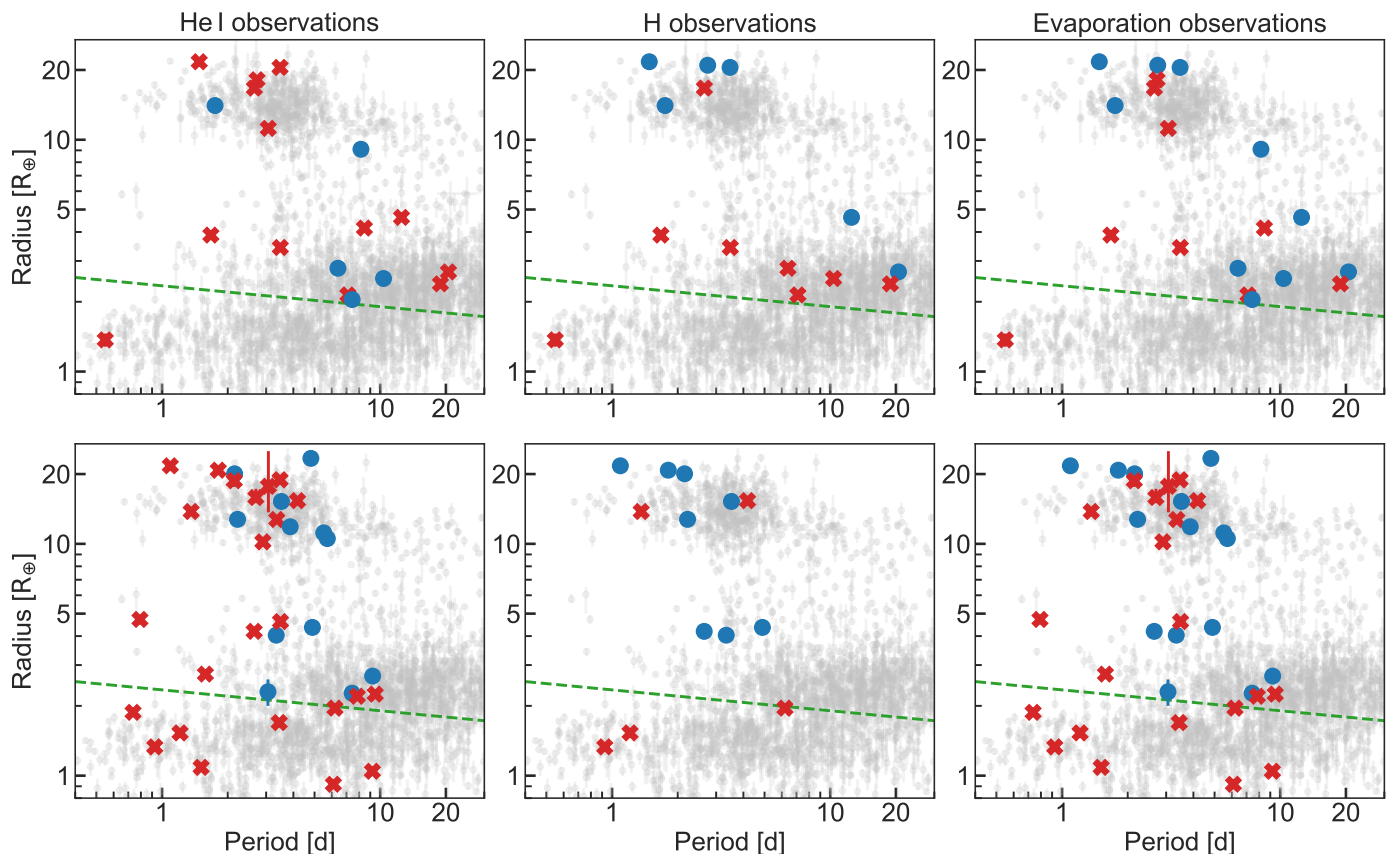


Fig. 11: Radius-period diagrams for planets with ages ≤ 1 Gyr (top panels) and > 1 Gyr (bottom panels) with He I (left panels) and H ($H\alpha$ or $Ly\alpha$, middle panels) observations, and evaporation (combination of He I and/or H observations, right panels). Detections and non-detections are marked as blue circles and red crosses, respectively. The radius gap (Van Eylen et al. 2018) is marked as a dashed green line. The grey points represent all known planets with period and radius determined with a precision better than 25% (data from NASA Exoplanet Archive).

detection. The ratio of He I detections to non-detections seems larger for old rather than young planets, but there are fewer differences when comparing the H detections to non-detections.

6.1.2. Small planet evaporation across stellar age

Figure 12 shows the radius-mass diagram for small planets ($R_p < 5 R_\oplus$ and $M_p < 30 M_\oplus$), also comparing evaporation proxies for young and old planets. Planets with $R_p \sim 1.5\text{--}3 R_\oplus$ fall in a degenerated region of the mass-radius diagram, and their bulk compositions can be consistent with a large range of models, from water worlds (planets with a large water mass fraction) to planets with rocky cores with H/He envelopes (Zeng et al. 2019). For these planets, in Figure 12, we found a mixture of detections and non-detections, with no difference between young and old planets.

Planets with $R_p > 3 R_\oplus$ are well above the water-rich composition line and are supposed to be gaseous with very light envelopes and low densities (Luque & Pallé 2022). In our sample there are four young and five old puffy planets with evaporation observations (see right panels of Fig. 12). While only 1 in 4 young planets has an evaporation detection, 3 out of 5 old planets have a detection, hinting that atmospheric escape of puffy sub-Neptunes is stronger at ages older than ~ 1 Gyr. Still, the numbers are small, and a larger sample is needed to confirm these findings.

For the planets above the radius valley, Malsky et al. (2023) predicted a He enhancement due to the diffusive separation of the atmospheric constituents where the He and metals are preferentially retained while H is evaporated. The timescale of this mechanism is comparable to the planet lifetime (~ 10 Gyr) and planets with ≤ 1 Gyr have not had time to show the effects of favoured H evaporation (Malsky et al. 2023). So, our young planet population is too young to suffer this differential escape process, and even some of our old planets could be considered young as well. Then, the long timescale might explain why Figure 12 does not show more He I detections for the old waterworlds than for the young ones. Malsky et al. (2023) predict that TOI-1235 b will have an He enhanced atmosphere at 10 Gyr, but Krishnamurthy et al. (2023) put a very restricted He I upper limit, although its age is poorly constrained ($5^{+5}_{-4.4}$ Gyr). The other planets listed in Malsky et al. (2023, Table 1) have no H/He observations to test their predictions.

Although Malsky et al. (2023) focus only on the small planet population ($\leq 3 R_\oplus$), the diffusive separation and the subsequent preferential H evaporation could be the mechanism to explain some observational results from Fig. 11 and 12 regarding large and intermediate-sized planets. i) There are no He I detections in young puffy planets but there are for old ones. TOI-1136 d is the only young puffy planet with $H\alpha$ detection, and the only three old puffy planets with H observations both show H evaporation. ii) WASP-52 b is the only young gas giant with He I detection (and also has $H\alpha$ detection) while there are several detections on

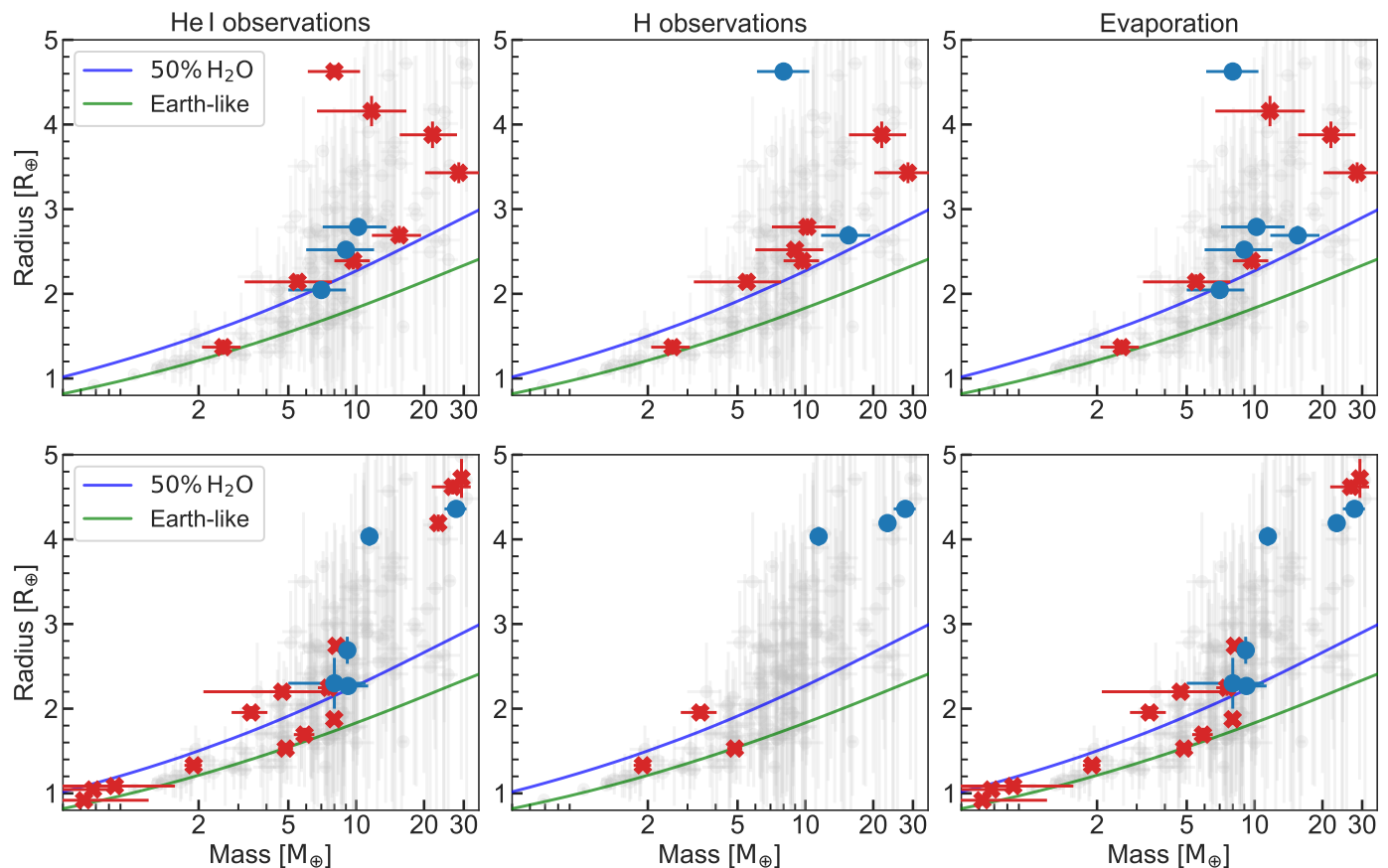


Fig. 12: Radius-mass diagrams for planets with ages ≤ 1 Gyr (top panels) and > 1 Gyr (bottom panels) with He I (left panels) and H ($H\alpha$ or $Ly\alpha$, middle panels) observations, and evaporation (combination of He I and/or H observations, right panels). Detections and non-detections are marked as blue circles and red crosses, respectively. The solid lines are the theoretical models from Zeng et al. (2019) for Earth-like (green) and 50% H_2O +50% rocky (blue) compositions. The grey points represent all known planets with mass and radius determined with a precision better than 20% (data from NASA Exoplanet Archive).

old gas giants, and $H\alpha$ is extensively detected in young and old gas giant planets.

6.2. Cosmic shoreline from He I observations

The cosmic shoreline (Zahnle 1998) is an empirical division found in the Solar System bodies that splits them between those that retain a certain amount of atmosphere and those that are purely bare rocks without atmosphere. The division was extended to the extrasolar planet population with success by Zahnle & Catling (2017). Determining precisely the cosmic shoreline is important as it has often been used to predict the existence of an atmosphere for newly discovered planets, and to argue for atmospheric characterisation follow-up (e.g. with the James Webb Space Telescope). Observationally, extended atmospheres are relatively easy to detect via H and He I absorptions. Here, we use these observations to better constrain the cosmic shoreline.

Zahnle & Catling (2017) found a power law between planet bolometric instellation (I_p) and planet velocity escape v_{esc} that follows $I_p \propto v_{\text{esc}}^4$. However, the radiation that shapes the exoplanet atmosphere is the X-rays and EUV stellar flux received by the planet during its early stages. Zahnle & Catling (2017) assumed the approximation of X-ray luminosity saturation (Jackson et al. 2012) to estimate the total extreme radiation (X+EUV radiation) received by the planet. Following Zahnle & Catling (2017, Eq. 27), we compute the cumulative X-rays and EUV in-

stellation (I_{X+EUV} ; considering $\lambda < 100$ nm) as a function of the planet instellation (I_p) and the stellar bolometric luminosity (L_\star):

$$I_{X+EUV} = I_p (L_\star / L_\odot)^{-0.6}. \quad (2)$$

We computed v_{esc} as

$$v_{\text{esc}} = \sqrt{2GM_p/R_p}, \quad (3)$$

where G is the universal gravitational constant. The empirical relation found between I_{X+EUV} with v_{esc} also follows the same power law ($I_{X+EUV} \propto v_{\text{esc}}^4$), as for I_p .

Zahnle & Catling (2017) presented the relationships between I_p and v_{esc} , and between I_{X+EUV} and v_{esc} for the planets and small bodies of the Solar System along with the exoplanet population. To test the predictions of the cosmic shoreline, we compared the proposed empirical relationships to the actual He I detections. Figure 13 reproduces Figures 1 and 2 from Zahnle & Catling (2017), and includes also the He I observations. Because the cosmic shorelines are empirical relations, only the slope in logarithmic scale is determined. Thus, we get from Zahnle & Catling (2017, Figs. 1 and 2) the independent terms to plot the empirical equations.

By definition, all He I (and $H\alpha$) detections must be below the cosmic shorelines plotted in Fig. 13. However, we find seven gas planets with He I (or $H\alpha$) detections in the region of supposedly

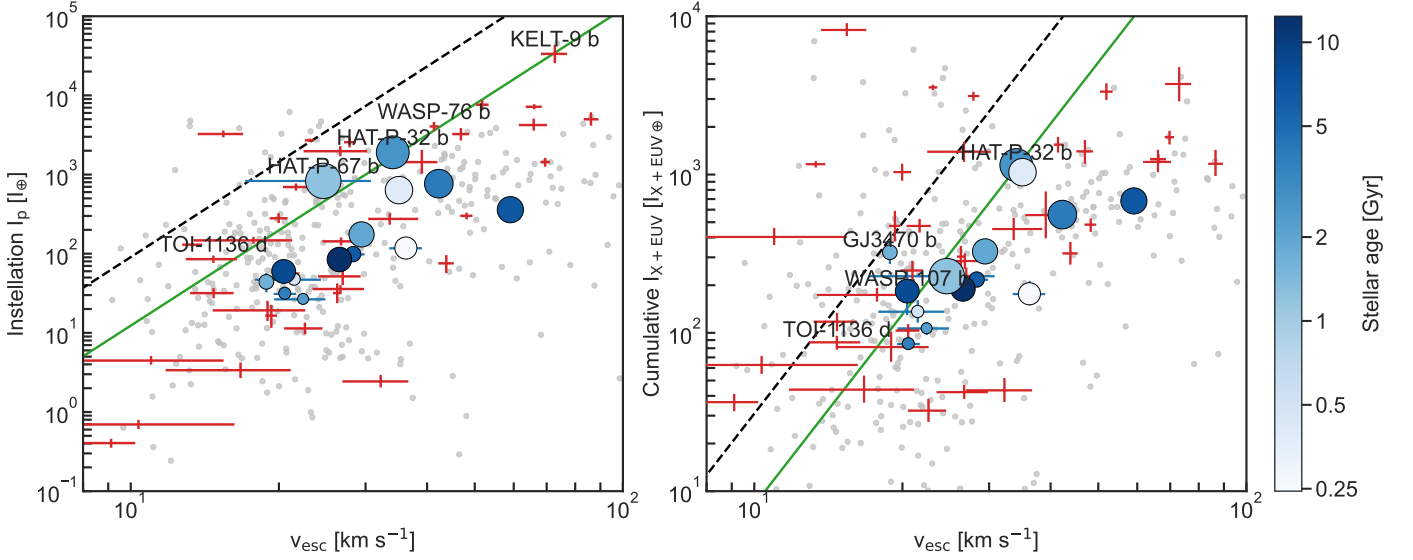


Fig. 13: Cosmic shoreline compared to He I observations. He I non-detections are denoted by red error bars with no marker. He I detections are circles scaled by their R_p and colour-coded by their stellar age (lateral colour bar). Installation relative to Earth vs escape velocity (*left panel*) and cumulative installation in the XUV range relative to Earth vs escape velocity (*right panel*) graphics. We marked the cosmic shoreline, as $I \propto v_{\text{esc}}^4$, from Zahnle & Catling (2017, solid green line) and constrained from the observations (dashed black line). Planets sitting above or on the cosmic shore and with H/He detections are labelled.

bare rocky planets. Those are the ones labelled in Fig. 13 panels. In Fig. 13 left panel, HAT-P-32 b and HAT-P-67 b are clearly located above the line, although their 1σ uncertainties fall in the limit of the cosmic shoreline. TOI-1136 d, WASP-76 b, and KELT-9 b which have He I non-detections but H α detections, are also over or above the cosmic shoreline. Moreover, in Fig. 13 right panel, HAT-P-32 b and WASP-107 b fall over the line, and GJ 3470 b and TOI-1136 d are clearly above the cosmic shoreline for energy-limited regime. With the exception of TOI-1136 d, the planets that contradict the shoreline are not young planets, with stellar ages >1 Gyr.

Zahnle & Catling (2017) stated that the $I \propto v_{\text{esc}}^4$ and $I_{X+EUUV} \propto v_{\text{esc}}^4$ lines are ‘drawn in by hand to guide the eye’. Thus, the evaporation detections above the shoreline can help to constrain the independent terms of those by-hand equations. For that purpose, we considered the planet whose uncertainties have the largest separation from the by-hand line to compute the limits of the cosmic shoreline. We took the coordinates of the extreme uncertainty as a point to calculate the line equation. We took HAT-P-67 b for the $I \propto v_{\text{esc}}^4$ line, and GJ 3470 b for $I_{X+EUUV} \propto v_{\text{esc}}^4$ although very similar results were obtained with TOI-1136 d. Then, it is trivial to get the line equation with the slope and one point. The cosmic shoreline equations constrained from the evaporation detections are

$$\log(I/I_{\oplus}) = 4 \log(v_{\text{esc}} [\text{km s}^{-1}]) - 2.04 \quad (4)$$

and

$$\log(I_{X+EUUV}/I_{X+EUUV_{\oplus}}) = 4 \log(v_{\text{esc}} [\text{km s}^{-1}]) - 2.51. \quad (5)$$

They are shown in Figure 13 left and right panels as dashed black lines, respectively. In both cases, the cosmic shoreline moved to higher radiation levels reducing the amount of exoplanets with no atmosphere. Further atmospheric observations and more precise measurements of the planets close to the shoreline will allow a better constraint of the observed cosmic shoreline.

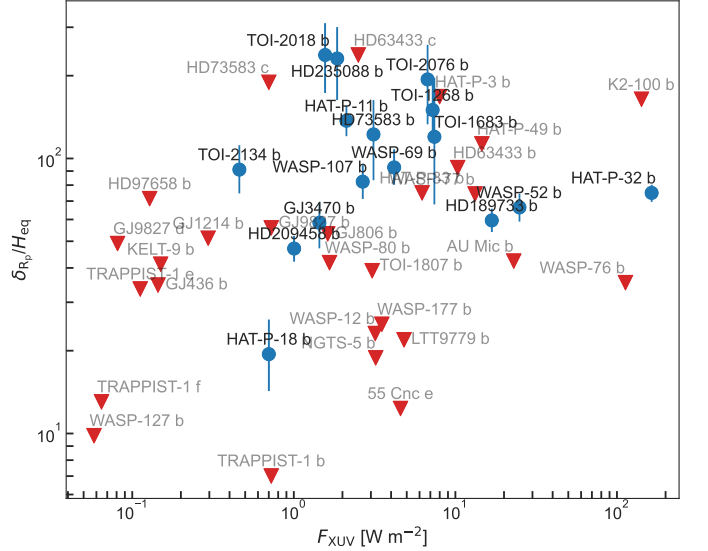


Fig. 14: He I transmission signal strength for the planets with detections (blue circles with error bars in black) and non-detections (red down-pointing triangles in grey) as a function of the stellar F_{XUV} ($\lambda = 5 - 504 \text{ \AA}$) at the planet distance. We show the equivalent height of the He I atmosphere, δ_{Rp} , normalised by the atmospheric scale height, H_{eq} . Data from Table M.1 and references therein.

6.3. Observed versus theoretical mass-loss rates

Since the first He I detection in planetary atmospheres, there have been many attempts to predict the presence of this line using other observable planetary parameters. Nortmann et al. (2018) performed one of the first attempts by computing $\delta_{Rp}/H_{\text{eq}}$. That is: the equivalent height of the He I absorbing atmosphere $\delta_{Rp} = (R_p^2 + D_{\text{He}} R_{\star}^2)^{1/2} - R_p$, where D_{He} is the He I absorption peak in %, divided by the atmospheric scale height

$H_{\text{eq}} = (k_B T_{\text{eq}})/(\mu g_p)$, where k_B , μ , and g_p are the Boltzmann constant, the mean molecular mass, and planet gravity, respectively. Figure 4 in [Nortmann et al. \(2018\)](#) presented a correlation between the He I absorption signal and F_{XUV} ($\lambda = 5 - 504 \text{ \AA}$), but with a sample of only five planets. Figure 14 reproduces the same diagram with the current set of 43 He I observations (detections and non-detections with F_{XUV} measurements). The trend is not that clear and there is no evident pattern between detections and non-detections, maybe due to the non-uniformity of the sample (e.g. different instruments and data analysis techniques).

Rather than using the strength of the He I absorption, [Vissapragada et al. \(2022b\)](#), and later [Zhang et al. \(2023a\)](#), explored the relation between the mass-loss rates derived from the observations (\dot{m}_{obs}) as a function of F_{XUV}/ρ_p (ρ_p is the planet density). While [Vissapragada et al. \(2022b\)](#) derived the observed mass-loss rates comparing the measured excess transit absorptions with a grid of Parker wind models, [Zhang et al. \(2023a\)](#) estimated the observed mass-loss rates from an order-of-magnitude method. Furthermore, [Zhang et al. \(2023a\)](#) found that the theoretical maximum energy-limited mass-loss rate (\dot{m}_{theory}) is proportional to $F_{\text{XUV}}/\rho_{\text{XUV}}$ (ρ_{XUV} is defined below). However, they reported very similar results when using F_{XUV}/ρ_p . Despite those differences, both works found a positive correlation between \dot{m}_{obs} and F_{XUV}/ρ_p , and, their energy-limited outflow efficiencies agree within uncertainties ([Vissapragada et al. \(2022b\)](#): $\eta_0 = 0.41^{+0.16}_{-0.13}$; [Zhang et al. \(2023a\)](#): $\eta_0 = 0.31 \pm 0.06$).

Here, we focus on the relationship between \dot{m}_{obs} and \dot{m}_{theory} while adding the two new He I detections presented in this work (TOI-1268 b and TOI-2018 b), which is the main difference with the study performed by [Zhang et al. \(2023a\)](#). For consistency, we followed the indications from [Zhang et al. \(2023b,a\)](#) to compute the $\dot{m}_{\text{obs}}-\dot{m}_{\text{theory}}$ diagram with our set of He I observations.

We made the same assumptions as in [Zhang et al. \(2023b,a\)](#) to calculate \dot{m}_{obs} with the order-of-magnitude method as

$$\dot{m}_{\text{obs}} = \frac{m_e m_{\text{He}} c_s c^2 EW R_\star}{0.25 f e^2 \lambda_0^2 \Sigma g_l f_l} \propto EW \cdot R_\star. \quad (6)$$

Equation 6 is computed in cgs units, where m_e is the electron mass, m_{He} is the He atomic mass, c_s is the sound speed (assumed to be $c_s = 10 \text{ km s}^{-1}$), c is the speed of light, EW is the equivalent width of the He I signal, R_\star is the stellar radius, 0.25 comes from assuming that 25 % of mass out-flow is He (atoms or ions), f is the fraction of He atoms in the metastable ground state (assumed to be $f = 10^{-6}$), e is the electron charge, λ_0 is the He I wavelength (fixed to 10833.3 \AA), $\Sigma g_l f_l$ is the sum of the product of the degeneracy and oscillator strength over the three lines of the He I triplet which is 1.62 ([Zhang et al. 2023a](#)).

The theoretical maximum energy-limited mass-loss rate (\dot{m}_{theory} ; [Caldirola et al. 2022](#); [Zhang et al. 2023a](#)), assuming that all the XUV flux received by the planet is spent on evaporation, is computed as

$$\dot{m}_{\text{theory}} = \frac{\pi R_{\text{XUV}}^3 F_{\text{XUV}}}{G M_p} = \frac{3 F_{\text{XUV}}}{4 G \rho_{\text{XUV}}} \propto F_{\text{XUV}}/\rho_{\text{XUV}}, \quad (7)$$

where F_{XUV} is the XUV flux ($\lambda = 5 - 504 \text{ \AA}$), R_{XUV} is the planetary XUV photosphere radius, G is the gravitational constant, M_p is the planet mass, and ρ_{XUV} is the planet density using the R_{XUV} . We followed the equations and indications from [Wang & Dai \(2018\)](#); [Zhang et al. \(2023b,a\)](#) to estimate R_{XUV} as

$$R_{\text{XUV}} = \frac{R_p}{1 + \beta^{-1} \ln(\rho_{\text{atm.XUV}}/\rho_{\text{atm.phot}})}, \quad (8)$$

where

$$\rho_{\text{atm.phot}} = \frac{P \mu}{k_B T_{\text{eq}}}; \quad \beta \equiv \frac{G M_c \mu}{R_p k_B T_{\text{eq}}}. \quad (9)$$

In Eqs. 8 and 9, P is the pressure at the white-light planet radius (assumed $P = 100 \text{ mbar}$), μ is the (dimensional) mean molecular mass (we assumed $\mu = 1.3 \times m_{\text{H}}$; m_{H} is the H atomic mass), k_B is Boltzmann constant, T_{eq} is the equilibrium temperature, M_c is the planet mass core, and $\rho_{\text{atm.XUV}}$ is the planet atmosphere's density at the R_{XUV} layer. We approximated $M_c \approx M_p$ and used $\rho_{\text{atm.XUV}} = 10^{-15} \text{ g cm}^{-3}$. Our computed values for ρ_{XUV} are consistent within errors with those presented in [Zhang et al. \(2023a, Table 3\)](#).

Figure 8 presents our computed observed and theoretical mass-loss rates, recovering the predicted positive correlation for the He I detections. For a quantitative analysis, we fitted a power law as $\dot{m}_{\text{obs}} = \eta_0 (\dot{m}_{\text{theory}})^\alpha$. We used `scipy`'s orthogonal distance regression to fit the equation $\log_{10}(\dot{m}_{\text{obs}}) = \alpha \log_{10}(\dot{m}_{\text{theory}}) + \log_{10}(\eta_0)$. We obtained an energy-limited efficiency of $\eta_0 = 0.35 \pm 0.04$, which is consistent with the previous derived values ([Vissapragada et al. 2022b](#): $\eta_0 = 0.41^{+0.16}_{-0.13}$; [Zhang et al. 2023a](#): $\eta_0 = 0.31 \pm 0.06$). TOI-1268 b and TOI-2018 b positions in the diagram agree with the previous detections, and they are over the fitted line. For the linearity between log mass-loss rates, we got $\alpha = 0.43 \pm 0.05$, also consistent with [Zhang et al. \(2023a, \$\alpha = 0.50 \pm 0.08\$ \)](#). When using ρ_p instead of ρ_{XUV} , we get slightly larger uncertainties for η_0 and α but consistent within uncertainties ($\eta_0 = 0.39 \pm 0.06$, $\alpha = 0.42 \pm 0.06$).

If the evaporation on those planets was in the energy-limited regime, they should exhibit a linear relation between \dot{m}_{obs} and \dot{m}_{theory} . Although we computed the mass-loss rates as an order-of-magnitude and with some approximations, α is $\sim 11\sigma$ apart from 1. We find a sub-linearity relation ($\alpha \sim 0.43 < 1$) and the efficiency of the \dot{m}_{obs} decreases with \dot{m}_{theory} , as already pointed out by both [Vissapragada et al. \(2021\)](#) and [Zhang et al. \(2023a\)](#). However, this is in agreement with the theory as models predict that as the F_{XUV} increases, the photo-evaporation escape begins to lose efficiency via radiative cooling (e.g. [Murray-Clay et al. 2009](#); [Caldirola et al. 2022](#)). The H/He ratio or different hydrodynamical regimes (e.g. [Lampón et al. 2020, 2021b,a, 2023](#)) may also contribute to derive a sub-linear relation.

Along the $\dot{m}_{\text{obs}}-\dot{m}_{\text{theory}}$ sub-linearity, five planets (TOI-2134 b, TOI-2018 b, HD 235088 b, HAT-P-11 b, and HAT-P-18 b) show an unphysical $>100\%$ photo-evaporation efficiency. \dot{m}_{theory} , as it is computed in Eq. 7, assumes the photo-evaporation scenario. However, there are other mechanisms that could enhance the atmospheric mass-loss, namely the core-powered and the Roche lobe overflow. The core-powered mechanism may contribute in the atmospheric escape of those planets as they are relatively young (except HAT-P-11 b and HAT-P-18 b). However, a core-powered contribution can not be confidently assumed in those planets, as other parameters as the H/He ratio, the stellar flux or the atmospheric heating efficiency may contribute to change the derived $\dot{m}_{\text{obs}}-\dot{m}_{\text{theory}}$ relation and yield unrealistic efficiencies. On the other hand, Roche lobe overflow is not expected, as these planets are not extremely close-in. Non-thermal processes (e.g. ion pick-up or sputtering) may also help to achieving a $>100\%$ efficiency in those planets ([Güdel et al. 2014](#)).

tions as function of the different spectral types. Figure 16 shows that K-type exoplanet hosting stars are the most targeted ones (29 planets), but also the spectral type with a larger detection percentage (45%). In fact, the two detections presented in this work, TOI-1268 b and TOI-2018 b, are both around K stars. For M-type stars, GJ 3470 b is the only clear He I triplet detection (Palle et al. 2020a; Ninan et al. 2020), along with the tentative detection on GJ 1214 b reported by Orell-Miquel et al. 2022. The three detections around F-type stars (HD 209458 b, Alonso-Floriano et al. 2019; HAT-P-67 b, Gully-Santiago et al. 2024; and HAT-P-32 b, Czesla et al. 2022) are interesting because these planets are hot Jupiters, and HAT-P-67 b and HAT-P-32 b possess very extended He structures (Gully-Santiago et al. 2024; Zhang et al. 2023c). To date, there are no He I detections of exoplanets orbiting G, A, B, or O stars. To further understand the dependence on spectral type, we also computed the histogram of He I detections and non-detections as function of the stellar mass (Fig. A.23). The number of detections increases from $0.47 M_{\odot}$ (GJ 3470) until peaking at $0.9 M_{\odot}$. Above $0.9 M_{\odot}$, non-detections are dominant over detections. Therefore, we can estimate a limit in host stellar mass at $\sim 0.9 M_{\odot}$ for the He I detections, which deserves further investigation.

We note that all the He I detections from Table M.1 are found in planets orbiting stars with $T_{\text{eff}} \lesssim 6250$ K, which is the temperature at which the Kraft Break happens (Kraft 1967). Exoplanet spin-orbit alignment seems to be related to the Kraft Break (e.g. Winn et al. 2010; Brown et al. 2017; Attia et al. 2023). To date, the hottest host star with He I detection is HAT-P-67 with $T_{\text{eff}} \sim 6400$ K. The observations of other ten planets orbiting ≥ 6250 K stars resulted in upper limits only. The Kraft Break marks also the transition between stars with outer convection zones and those without. These convection zones are predicted to generate magnetic fields able to heat the chromosphere and the corona, increasing the XUV radiation (Wright et al. 2011). Therefore, stars without this heating mechanism are less likely to significantly populate the He metastable level of their exoplanets' atmospheres. The link between the stellar T_{eff} , the flux in the XUV range and the He I triplet detections deserves further investigation.

6.6. He I dependence on planetary parameters

One of the aims of the MOPYS project was also to find a relation between planetary and stellar properties that could explain, and predict, the He I detections and non-detections, but without the need to involve the strength of the signal itself. From the many explored relations and diagrams, only the equilibrium temperature (T_{eq}) and the planet density (ρ_p) showed some hints of such relationship. Figure 17 presents the T_{eq} versus ρ_p diagram where the information about the He I observations is encoded in the colour markers (blue circles are detections, red crosses are non-detections, and non-conclusive observations are not shown). Although both are planet properties, T_{eq} encapsulates information about the star via the T_{eff} and the a_p/R_{\star} parameters.

From Fig. 17, one clear result is that there are no He I detections on exoplanets with $T_{\text{eq}} \geq 2000$ K. The hottest detection at $T_{\text{eq}} \sim 2000$ K comes from the puffy planet HAT-P-67 b. In fact, the data in Figure 17 hint to a density/ T_{eq} upper boundary for the detections. We draw ‘by-hand’ this observational limit for a better visualisation, which follows $T_{\text{eq}} \approx -500 \log_{10}(\rho_p)$ trend, approximately. If we assume that detections and non-detections are distributed randomly across the $T_{\text{eq}}-\rho_p$ parameter space, the probability of extracting 14 non-detections from a pool of 17 detections and 36 non-detections is only 0.16%. Although it is an

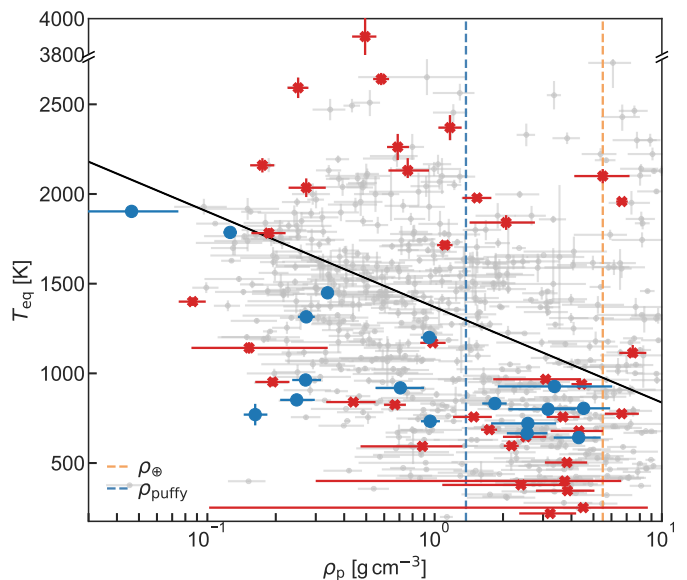


Fig. 17: Equilibrium temperature (T_{eq}) vs planet density (ρ_p) diagram for the He I detections (blue circles) and non-detections (red crosses). The black line (drawn by-eye) indicates the hinted upper boundary for the He I detections. The coloured dashed vertical lines indicate the Earth’s density (ρ_{\oplus} ; orange line at $\sim 5.5 \text{ g cm}^{-3}$), and a representative density where the puffy planet population starts (ρ_{puffy} ; blue line at $\sim 1.3 \text{ g cm}^{-3}$; Luque & Pallé 2022). All known planets with T_{eq} and ρ_p determined with a precision better than 50% are marked with grey dots (data from NASA Exoplanet Archive).

approximate calculation, the very low probability supports the robustness of the boundary. For planets falling above the line it is unlikely that one can detect He I, as all the inspected planets resulted in non-detections. Below that line, He I detections and non-detections are equally found.

At face value our results indicate that for high-density planets (from Earth-size to sub-Neptune-size) He I absorptions are present only in cool atmospheres. A possible interpretation is that these type of planets quickly lose any H/He atmosphere when subjected to strong stellar instellation (assuming that T_{eq} is directly related at the population level to stellar flux). For low-density planets (gas giants) He I detection are found up to ~ 2000 K.

Further He I detections will confirm or disprove the observational boundary proposed here, and define its exact dependence on different planet parameters.

7. Conclusions

This work shows the first results of the MOPYS survey, a project that aims to test the predictions of atmospheric evolution theories by confronting them with observations of evaporation proxies. We present CARMENES and GIARPS high-resolution transmission spectroscopy observations of 20 exoplanets. We analysed their atmospheres searching for He I triplet absorption in the NIR, and H α in the VIS as well. We report two new detections of the He I triplet for TOI-1268 b and TOI-2018 b, and a new H α detection for TOI-1136 d. We also found hints of He I on HD 63433 b, and of H α on HD 73583 b and c, which need further confirmation.

We complemented our target list with other planets from the literature with He I triplet and H α (and Ly α for some particular planets as well) observations, for a total of 70 planets. We considered those lines as proxy of evaporation to test mass-loss theories. The main findings of our study are:

- Our age distribution of evaporation detections does not favour either photo-evaporation or core-powered mass-loss as planet formation mechanisms.
- We find no trend in atmospheric evaporation with stellar age. Young (<1-Gyr-old) planets do not exhibit more He I or H α detections than older planets.
- Evaporation (He I or H α) signals are more frequent or easier to detect for planets around stellar hosts within $\sim 1\text{--}3$ Gyr ages.
- The fraction of planets that show He I detections is much larger for K-type stars (45%) than for any other spectral type.
- We find no evaporation detections of young and old planets below the radius gap, confirming rocky planets are not under extreme evaporation, at least after the first ~ 300 Myr.
- We find hints that evaporation of puffy sub-Neptunes ($R_p > 3 R_\oplus$) happens at ages older than 1 Gyr, although the number of planets is small, and a larger sample is needed to confirm this finding.
- We provide new constraints to the cosmic shoreline, by using the evaporation detections as evidences for the existence of planetary atmospheres. Our cosmic shoreline move to higher irradiation flux, reducing the parameter space of bare rocky planets.
- We present the He-related dimensionless parameter $R_{\text{He}}/R_{\text{Hill}}$, as a new valid parameter to study the He I detections and upper limits.
- All the He I detections are found in planets orbiting stars with $T_{\text{eff}} \lesssim 6250$ K, which is the temperature at which the Kraft Break happens.
- We determine a statistically significant observational upper boundary for He I detections in the T_{eq} versus ρ_p parameter space. The line decays at a rate of $T_{\text{eq}} \approx -500 \log_{10}(\rho_p)$, approximately. Planets falling above that boundary are unlikely to show He I absorption signals.

We encourage further evaporation observations (Ly α , H α , and He I triplet) to increase and complete the sample presented in this work. Although this work represents the biggest evaporation survey to date (specially focused on <1Gyr-old planets), some key questions of planet formation and atmospheric evaporation remained unanswered. In particular, the detection and atmospheric characterisation of very young planets (<100 Myr) is key for discriminating between different mass-loss processes in planetary atmospheres. It is precisely because of their age that they are the most difficult planets to analyse their atmospheres.

Acknowledgements. CARMENES is an instrument at the Centro Astronómico Hispano en Andalucía (CAHA) at Calar Alto (Almería, Spain), operated jointly by the Junta de Andalucía and the Instituto de Astrofísica de Andalucía (CSIC). The authors wish to express their sincere thanks to all members of the Calar Alto staff for their expert support of the instrument and telescope operation. CARMENES was funded by the Max-Planck-Gesellschaft (MPG), the Consejo Superior de Investigaciones Científicas (CSIC), the Ministerio de Economía y Competitividad (MINECO) and the European Regional Development Fund (ERDF) through projects FICTS-2011-02, ICTS-2017-07-CAHA-4, and CAHA16-CE-3978, and the members of the CARMENES Consortium (Max-Planck-Institut für Astronomie, Instituto de Astrofísica de Andalucía, Landessternwarte Königstuhl, Institut de Ciències de l’Espai, Institut für Astrophysik Göttingen, Universidad Complutense de Madrid, Thüringer Landessternwarte Tautenburg, Instituto de Astrofísica de Canarias, Hamburger Sternwarte, Centro de Astrobiología and Centro Astronómico Hispano-Alemán), with additional contributions by the MINECO, the Deutsche Forschungsgemeinschaft

(DFG) through the Major Research Instrumentation Programme and Research Unit FOR2544 “Blue Planets around Red Stars”, the Klaus Tschira Stiftung, the states of Baden-Württemberg and Niedersachsen, and by the Junta de Andalucía. Based on observations collected at the Centro Astronómico Hispano-Alemán (CAHA) at Calar Alto, proposals 21B-3.5-004, 22A-3.5-007, 22B-3.5-009, 23A-3.5-009, and 23B-3.5-002, operated jointly by Junta de Andalucía and Consejo Superior de Investigaciones Científicas (IAA-CSIC). We used data from the CARMENES data archive at CAB (CSIC-INTA). We acknowledge the use of the ExoAtmospheres database during the preparation of this work. This work is partly supported by JSPS KAKENHI Grant Number JPJP24H00017 and JSPS Bilateral Program Number JPJSBP120249910. This paper is based on observations made with the MuSCAT2 instrument, developed by ABC, at Telescopio Carlos Sánchez operated on the island of Tenerife by the IAC in the Spanish Observatorio del Teide. We acknowledge financial support from the Agencia Estatal de Investigación (AEI/10.13039/501100011033) of the Ministerio de Ciencia e Innovación and the ERDF “A way of making Europe” through projects PID2022-137241NBC4[1:4], PID2019-109522GB-C5[1:4], PID2021-125627OB-C31, PID2022-141216NB-I00, Ariel Postdoctoral Fellowship program of the Swedish National Space Agency (SNSA), and the Centre of Excellence “Severo Ochoa” and “María de Maeztu” awards to the Instituto de Astrofísica de Canarias (CEX2019-000920-S), Instituto de Astrofísica de Andalucía (CEX2021-001131-S) and Institut de Ciències de l’Espai (CEX2020-001058-M). J.O.M. agraeix el recolzament, suport i ànims que sempre ha rebut per part de Padrina Conxa, Padrina Mercè, Jeroni, Mercè i més familiars i amics. J.O.M. gratefully acknowledge the inspiring discussions with Maite Mateu, Alejandro Almodóvar, and Joan Perelló, and the support from Guillem, Benet, and Montse. This research has made use of resources from VallAlbaida-Mallorca collaboration. J.O.M. acknowledges the contributions and patience of Jorge Terol Calvo, i molt especialment a tu, Yess. L.N. and F.L. acknowledge the support by the Deutsche Forschungsgemeinschaft (DFG, German Research Foundation) – Project number 314665159. E.K. and S.H.A. acknowledge the support from the Danish Council for Independent Research through grant No.2032-00230B. E.N. acknowledges the support by the DFG Research Unit FOR2544 “Blue Planets around Red Stars”. S.C. acknowledges the support of the DFG priority program SPP 1992 “Exploring the Diversity of Extrasolar Planets” (CZ 222/5-1).

References

- Addison, B. C., Knudstrup, E., Wong, I., et al. 2021, *AJ*, 162, 292
- Allan, A. P., Vidotto, A. A., Villarreal D’Angelo, C., Dos Santos, L. A., & Driessen, F. A. 2024, *MNRAS*, 527, 4657
- Allart, R., Bourrier, V., Lovis, C., et al. 2019, *A&A*, 623, A58
- Allart, R., Bourrier, V., Lovis, C., et al. 2018, *Science*, 362, 1384
- Allart, R., Lemée-Joliecoeur, P. B., Jaziri, A. Y., et al. 2023, *A&A*, 677, A164
- Allart, R., Pino, L., Lovis, C., et al. 2020, *A&A*, 644, A155
- Alonso-Floriano, F. J., Snellen, I. A. G., Czesla, S., et al. 2019, *A&A*, 629, A110
- Anderson, D. R., Temple, L. Y., Nielsen, L. D., et al. 2018, arXiv e-prints, arXiv:1809.04897
- Attia, O., Bourrier, V., Delisle, J. B., & Eggenberger, P. 2023, *A&A*, 674, A120
- Barenfeld, S. A., Carpenter, J. M., Ricci, L., & Isella, A. 2016, *ApJ*, 827, 142
- Barragán, O., Aigrain, S., Kubyshkina, D., et al. 2019, *MNRAS*, 490, 698
- Barragán, O., Armstrong, D. J., Gandolfi, D., et al. 2022, *MNRAS*, 514, 1606
- Baruteau, C., Bai, X., Mordasini, C., & Mollière, P. 2016, *Space Sci. Rev.*, 205, 77
- Bello-Arufe, A., Cabot, S. H. C., Mendonça, J. M., Buchhave, L. A., & Rathcke, A. D. 2022, *AJ*, 163, 96
- Bello-Arufe, A., Knutson, H. A., Mendonça, J. M., et al. 2023, *AJ*, 166, 69
- Ben-Jaffel, L., Ballester, G. E., García Muñoz, A., et al. 2022, *Nature Astronomy*, 6, 141
- Benatti, S., Damasso, M., Borsa, F., et al. 2021, *A&A*, 650, A66
- Bennett, K. A., Redfield, S., Oklopčić, A., et al. 2023, *AJ*, 165, 264
- Bouma, L. G., Palumbo, E. K., & Hillenbrand, L. A. 2023, *ApJ*, 947, L3
- Bourrier, V., Lecavelier des Etangs, A., Ehrenreich, D., et al. 2018, *A&A*, 620, A147
- Bouvier, J., Barrado, D., Moraux, E., et al. 2018, *A&A*, 613, A63
- Brogi, M., Giacobbe, P., Guilluy, G., et al. 2018, *A&A*, 615, A16
- Brown, D. J. A., Triaud, A. H. M. J., Doyle, A. P., et al. 2017, *MNRAS*, 464, 810
- Brown, T. M., Baliber, N., Bianco, F. B., et al. 2013, *PASP*, 125, 1031
- Buchner, J., Georgakakis, A., Nandra, K., et al. 2014, *A&A*, 564, A125
- Caballero, J. A., Guàrdia, J., López del Fresno, M., et al. 2016, in *Society of Photo-Optical Instrumentation Engineers (SPIE) Conference Series*, Vol. 9910, *Observatory Operations: Strategies, Processes, and Systems VI*, ed. A. B. Peck, R. L. Seaman, & C. R. Benn, 99100E
- Caldirolì, A., Haardt, F., Gallo, E., et al. 2022, *A&A*, 663, A122
- Carleo, I., Youngblood, A., Redfield, S., et al. 2021, *AJ*, 161, 136
- Casasayas-Barris, N., Orell-Miquel, J., Stangret, M., et al. 2021a, *A&A*, 654, A163

- Casasayas-Barris, N., Palle, E., Nowak, G., et al. 2017, *A&A*, 608, A135
- Casasayas-Barris, N., Palle, E., Stangret, M., et al. 2021b, *A&A*, 647, A26
- Casasayas-Barris, N., Pallé, E., Yan, F., et al. 2019, *A&A*, 628, A9
- Castelli, F. & Kurucz, R. L. 2003, in *Modelling of Stellar Atmospheres*, ed. N. Piskunov, W. W. Weiss, & D. F. Gray, Vol. 210, A20
- Cauley, P. W., Redfield, S., & Jensen, A. G. 2017, *AJ*, 153, 81
- Chen, G., Casasayas-Barris, N., Pallé, E., et al. 2020, *A&A*, 635, A171
- Christiansen, J. L., Zink, J. K., Hardegree-Ullman, K. K., et al. 2023, *AJ*, 166, 248
- Claudi, R., Benatti, S., Carleo, I., et al. 2016, in *Society of Photo-Optical Instrumentation Engineers (SPIE) Conference Series*, Vol. 9908, *Ground-based and Airborne Instrumentation for Astronomy VI*, ed. C. J. Evans, L. Simard, & H. Takami, 99081A
- Cortés-Zuleta, P., Rojo, P., Wang, S., et al. 2020, *A&A*, 636, A98
- Cosentino, R., Lovis, C., Pepe, F., et al. 2012, in *Society of Photo-Optical Instrumentation Engineers (SPIE) Conference Series*, Vol. 8446, *Ground-based and Airborne Instrumentation for Astronomy IV*, ed. I. S. McLean, S. K. Ramsay, & H. Takami, 84461V
- Cosentino, R., Lovis, C., Pepe, F., et al. 2014, in *Society of Photo-Optical Instrumentation Engineers (SPIE) Conference Series*, Vol. 9147, *Ground-based and Airborne Instrumentation for Astronomy V*, 91478C
- Cummings, J. D., Deliyannis, C. P., Maderak, R. M., & Steinhauer, A. 2017, *AJ*, 153, 128
- Curtis, J. L., Agüeros, M. A., Douglas, S. T., & Meibom, S. 2019, *ApJ*, 879, 49
- Czesla, S., Lampón, M., Cont, D., et al. 2024, *A&A*, 683, A67
- Czesla, S., Lampón, M., Sanz-Forcada, J., et al. 2022, *A&A*, 657, A6
- Dai, F., Masuda, K., Beard, C., et al. 2023a, *AJ*, 165, 33
- Dai, F., Schlafman, K. C., Reggiani, H., et al. 2023b, *AJ*, 166, 49
- David, T. J., Petigura, E. A., Luger, R., et al. 2019, *ApJ*, 885, L12
- Dawson, R. I. & Johnson, J. A. 2018, *ARA&A*, 56, 175
- dos Santos, L. A., Ehrenreich, D., Bourrier, V., et al. 2020, *A&A*, 640, A29
- dos Santos, L. A., García Muñoz, A., Sing, D. K., et al. 2023, *AJ*, 166, 89
- Douglas, S. T., Agüeros, M. A., Covey, K. R., & Kraus, A. 2017, *ApJ*, 842, 83
- Douglas, S. T., Curtis, J. L., Agüeros, M. A., et al. 2019, *ApJ*, 879, 100
- Drake, G. W. 1971, *Phys. Rev. A*, 3, 908
- Ehrenreich, D., Bourrier, V., Wheatley, P. J., et al. 2015, *Nature*, 522, 459
- El Mufti, M., Plavchan, P. P., Isaacson, H., et al. 2021, *arXiv e-prints*, arXiv:2112.13448
- Espinoza, N. 2018, *RNAAS*, 2, 209
- Espinoza, N., Kossakowski, D., & Brahm, R. 2019, *MNRAS*, 490, 2262
- Fedele, D., van den Ancker, M. E., Henning, T., Jayawardhana, R., & Oliveira, J. M. 2010, *A&A*, 510, A72
- Feinstein, A. D., Montet, B. T., Johnson, M. C., et al. 2021, *AJ*, 162, 213
- Feroz, F., Hobson, M. P., & Bridges, M. 2009, *MNRAS*, 398, 1601
- Foreman-Mackey, D., Agol, E., Angus, R., & Ambikasaran, S. 2017, *AJ*, 154, 220
- Fossati, L., Guilluy, G., Shaikhislamov, I. F., et al. 2022, *A&A*, 658, A136
- Fossati, L., Pillitteri, I., Shaikhislamov, I. F., et al. 2023, *A&A*, 673, A37
- Fournier-Tondreau, M., MacDonald, R. J., Radica, M., et al. 2024, *MNRAS*, 528, 3354
- Fu, G., Espinoza, N., Sing, D. K., et al. 2022, *ApJ*, 940, L35
- Fuhrmeister, B., Czesla, S., Hildebrandt, L., et al. 2020, *A&A*, 640, A52
- Fukui, A., Narita, N., Tristram, P. J., et al. 2011, *PASJ*, 63, 287
- Fulton, B. J. & Petigura, E. A. 2018, *AJ*, 156, 264
- Fulton, B. J., Petigura, E. A., Blunt, S., & Sinukoff, E. 2018, *PASP*, 130, 044504
- Fulton, B. J., Petigura, E. A., Howard, A. W., et al. 2017, *AJ*, 154, 109
- Gaidos, E., Hirano, T., Beichman, C., et al. 2022, *MNRAS*, 509, 2969
- Gaidos, E., Hirano, T., Lee, R. A., et al. 2023, *MNRAS*, 518, 3777
- Gaidos, E., Hirano, T., Mann, A. W., et al. 2020a, *MNRAS*, 495, 650
- Gaidos, E., Hirano, T., Omiya, M., et al. 2021, *RNAAS*, 5, 238
- Gaidos, E., Hirano, T., Wilson, D. J., et al. 2020b, *MNRAS*, 498, L119
- Gaidos, E., Mann, A. W., Rizzuto, A., et al. 2017, *MNRAS*, 464, 850
- Gillon, M., Triaud, A. H. M. J., Demory, B.-O., et al. 2017, *Nature*, 542, 456
- Ginzburg, S., Schlichting, H. E., & Sari, R. 2016, *ApJ*, 825, 29
- Ginzburg, S., Schlichting, H. E., & Sari, R. 2018, *MNRAS*, 476, 759
- Gruner, D. & Barnes, S. A. 2020, *A&A*, 644, A16
- Güdel, M., Dvorak, R., Erkaev, N., et al. 2014, in *Protostars and Planets VI*, ed. H. Beuther, R. S. Klessen, C. P. Dullemond, & T. Henning, 883–906
- Guenther, E. W., Fossati, L., & Kabath, P. 2023, *arXiv e-prints*, arXiv:2311.02965
- Guilluy, G., Andretta, V., Borsa, F., et al. 2020, *A&A*, 639, A49
- Guilluy, G., Bourrier, V., Jaziri, Y., et al. 2023, *A&A*, 676, A130
- Gully-Santiago, M., Morley, C. V., Luna, J., et al. 2024, *AJ*, 167, 142
- Gupta, A. & Schlichting, H. E. 2020, *MNRAS*, 493, 792
- Haisch, Karl E., J., Lada, E. A., & Lada, C. J. 2001, *ApJ*, 553, L153
- Hartman, J. D., Bakos, G. Á., Buchhave, L. A., et al. 2015, *AJ*, 150, 197
- Hedges, C., Hughes, A., Zhou, G., et al. 2021, *AJ*, 162, 54
- Hejazi, N., Crossfield, I. J. M., Nordlander, T., et al. 2023, *ApJ*, 949, 79
- Hernández, J., Hartmann, L., Megeath, T., et al. 2007, *ApJ*, 662, 1067
- Hirano, T., Gaidos, E., Harakawa, H., et al. 2024, *MNRAS*, 530, 3117
- Hirano, T., Krishnamurthy, V., Gaidos, E., et al. 2020, *ApJ*, 899, L13
- Howard, W. S., Kowalski, A. F., Flagg, L., et al. 2023, *ApJ*, 959, 64
- Jackson, A. P., Davis, T. A., & Wheatley, P. J. 2012, *MNRAS*, 422, 2024
- Jenkins, J. S., Díaz, M. R., Kurtovic, N. T., et al. 2020, *Nature Astronomy*, 4, 1148
- Jensen, A. G., Cauley, P. W., Redfield, S., Cochran, W. D., & Endl, M. 2018, *AJ*, 156, 154
- Jensen, A. G., Redfield, S., Endl, M., et al. 2012, *ApJ*, 751, 86
- Kabáth, P., Chaturvedi, P., MacQueen, P. J., et al. 2022, *MNRAS*, 513, 5955
- Kanodia, S., Cañas, C. I., Stefansson, G., et al. 2020, *ApJ*, 899, 29
- Kanodia, S., Libby-Roberts, J., Cañas, C. I., et al. 2022, *AJ*, 164, 81
- Kasper, D., Bean, J. L., Oklopčić, A., et al. 2020, *AJ*, 160, 258
- Kausch, W., Noll, S., Smette, A., et al. 2015, *A&A*, 576, A78
- Kawachi, K., Murgas, F., Palle, E., et al. 2022, *A&A*, 666, A4
- Kipping, D. M. 2013, *MNRAS*, 435, 2152
- Kirk, J., Alam, M. K., López-Morales, M., & Zeng, L. 2020, *AJ*, 159, 115
- Kirk, J., Dos Santos, L. A., López-Morales, M., et al. 2022, *AJ*, 164, 24
- Koskinen, T. T., Lavvas, P., Huang, C., et al. 2022, *ApJ*, 929, 52
- Kotani, T., Tamura, M., Nishikawa, J., et al. 2018, in *Society of Photo-Optical Instrumentation Engineers (SPIE) Conference Series*, Vol. 10702, *Ground-based and Airborne Instrumentation for Astronomy VII*, ed. C. J. Evans, L. Simard, & H. Takami, 1070211
- Kraft, R. P. 1967, *ApJ*, 150, 551
- Kreidberg, L. 2015, *PASP*, 127, 1161
- Kreidberg, L. & Oklopčić, A. 2018, *RNAAS*, 2, 44
- Krishnamurthy, V., Hirano, T., Gaidos, E., et al. 2023, *MNRAS*, 521, 1210
- Krishnamurthy, V., Hirano, T., Stefansson, G., et al. 2021, *AJ*, 162, 82
- Krolikowski, D. M., Kraus, A. L., Tofflemire, B. M., et al. 2024, *AJ*, 167, 79
- Kulow, J. R., France, K., Linsky, J., & Loyd, R. O. P. 2014, *ApJ*, 786, 132
- Lam, K. W. F., Faedi, F., Brown, D. J. A., et al. 2017, *A&A*, 599, A3
- Lampón, M., López-Puertas, M., Czesla, S., et al. 2021a, *A&A*, 648, L7
- Lampón, M., López-Puertas, M., Lara, L. M., et al. 2020, *A&A*, 636, A13
- Lampón, M., López-Puertas, M., Sanz-Forcada, J., et al. 2023, *A&A*, 673, A140
- Lampón, M., López-Puertas, M., Sanz-Forcada, J., et al. 2021b, *A&A*, 647, A129
- Lendl, M., Csizmadia, S., Deline, A., et al. 2020, *A&A*, 643, A94
- Lopez, E. D., Fortney, J. J., & Miller, N. 2012, *ApJ*, 761, 59
- Loyd, R. O. P., Shkolnik, E. L., Schneider, A. C., et al. 2020, *ApJ*, 890, 23
- Lund, M. B., Rodriguez, J. E., Zhou, G., et al. 2017, *AJ*, 154, 194
- Lueke, R. & Pallé, E. 2022, *Science*, 377, 1211
- Mallorquín, M., Béjar, V. J. S., Lodieu, N., et al. 2023, *A&A*, 671, A163
- Malsky, I., Rogers, L., Kempton, E. M. R., & Marounina, N. 2023, *Nature Astronomy*, 7, 57
- Mamajek, E. E. & Hillenbrand, L. A. 2008, *ApJ*, 687, 1264
- Mann, A. W., Gaidos, E., Mace, G. N., et al. 2016, *ApJ*, 818, 46
- Mann, A. W., Johnson, M. C., Vanderburg, A., et al. 2020, *AJ*, 160, 179
- Mann, A. W., Vanderburg, A., Rizzuto, A. C., et al. 2018, *AJ*, 155, 4
- Mayo, A. W., Dressing, C. D., Vanderburg, A., et al. 2023, *AJ*, 165, 235
- Mayor, M., Pepe, F., Queloz, D., et al. 2003, *The Messenger*, 114, 20
- McCully, C., Volgenau, N. H., Harbeck, D.-R., et al. 2018, in *Society of Photo-Optical Instrumentation Engineers (SPIE) Conference Series*, Vol. 10707, *Proc. SPIE*, 107070K
- McLaughlin, D. B. 1924, *ApJ*, 60, 22
- Montes, D., López-Santiago, J., Gálvez, M. C., et al. 2001, *MNRAS*, 328, 45
- Morris, R. L., Twicken, J. D., Smith, J. C., et al. 2017, *Kepler Data Processing Handbook: Photometric Analysis*, Kepler Science Document KSCI-19081-002
- Murray-Clay, R. A., Chiang, E. I., & Murray, N. 2009, *ApJ*, 693, 23
- Nagel, E., Czesla, S., Kaminski, A., et al. 2023, *A&A*, 680, A73
- Nardiello, D., Malavolta, L., Desidera, S., et al. 2022, *A&A*, 664, A163
- Narita, N., Fukui, A., Kusakabe, N., et al. 2019, *Journal of Astronomical Telescopes, Instruments, and Systems*, 5, 015001
- Newton, E. R., Rampalli, R., Kraus, A. L., et al. 2022, *AJ*, 164, 115
- Ninan, J. P., Stefansson, G., Mahadevan, S., et al. 2020, *ApJ*, 894, 97
- Nortmann, L., Pallé, E., Salz, M., et al. 2018, *Science*, 362, 1388
- Oklopčić, A. 2019, *ApJ*, 881, 133
- Oklopčić, A. & Hirata, C. M. 2018, *ApJ*, 855, L11
- Oliva, E., Origlia, L., Maiolino, R., et al. 2012, in *Society of Photo-Optical Instrumentation Engineers (SPIE) Conference Series*, Vol. 8446, *Ground-based and Airborne Instrumentation for Astronomy IV*, ed. I. S. McLean, S. K. Ramsay, & H. Takami, 84463T
- Oliva, E., Origlia, L., Scuderì, S., et al. 2015, *A&A*, 581, A47
- Orell-Miquel, J., Lampón, M., López-Puertas, M., et al. 2023, *A&A*, 677, A56
- Orell-Miquel, J., Murgas, F., Pallé, E., et al. 2022, *A&A*, 659, A55
- Osborn, H. P., Bonfanti, A., Gandolfi, D., et al. 2022, *A&A*, 664, A156
- Owen, J. E. & Jackson, A. P. 2012, *MNRAS*, 425, 2931
- Owen, J. E. & Lai, D. 2018, *MNRAS*, 479, 5012
- Owen, J. E. & Wu, Y. 2013, *ApJ*, 775, 105
- Owen, J. E. & Wu, Y. 2016, *ApJ*, 817, 107
- Owen, J. E. & Wu, Y. 2017, *ApJ*, 847, 29
- Palle, E., Nortmann, L., Casasayas-Barris, N., et al. 2020a, *A&A*, 638, A61

- Palle, E., Orell-Miquel, J., Brady, M., et al. 2023, *A&A*, 678, A80
- Palle, E., Oshagh, M., Casasayas-Barris, N., et al. 2020b, *A&A*, 643, A25
- Parviainen, H., Tingley, B., Deeg, H. J., et al. 2019, *A&A*, 630, A89
- Pérez-González, J., Greklek-McKeon, M., Vissapragada, S., et al. 2024, *AJ*, 167, 214
- Petit dit de la Roche, D. J. M., van den Ancker, M. E., & Miles-Paez, P. A. 2020, *RNAAS*, 4, 231
- Plavchan, P., Barclay, T., Gagné, J., et al. 2020, *Nature*, 582, 497
- Plez, B. 2012, *Turbospectrum: Code for spectral synthesis*, *Astrophysics Source Code Library*, record ascl:1205.004
- Quirrenbach, A., Amado, P. J., Caballero, J. A., et al. 2014, in *Society of Photo-Optical Instrumentation Engineers (SPIE) Conference Series*, Vol. 9147, *Ground-based and Airborne Instrumentation for Astronomy V*, ed. S. K. Ramsay, I. S. McLean, & H. Takami, 91471F
- Quirrenbach, A., CARMENES Consortium, Amado, P. J., et al. 2020, in *Society of Photo-Optical Instrumentation Engineers (SPIE) Conference Series*, Vol. 11447, 114473C
- Rainer, M., Harutyunyan, A., Carleo, I., et al. 2018, in *Society of Photo-Optical Instrumentation Engineers (SPIE) Conference Series*, Vol. 10702, *Ground-based and Airborne Instrumentation for Astronomy VII*, ed. C. J. Evans, L. Simard, & H. Takami, 1070266
- Rebull, L. M., Stauffer, J. R., Bouvier, J., et al. 2016, *AJ*, 152, 113
- Ricker, G. R., Winn, J. N., Vanderspek, R., et al. 2015, *Journal of Astronomical Telescopes, Instruments, and Systems*, 1, 014003
- Rockcliffe, K. E., Newton, E. R., Youngblood, A., et al. 2021, *AJ*, 162, 116
- Rockcliffe, K. E., Newton, E. R., Youngblood, A., et al. 2023, *AJ*, 166, 77
- Rossiter, R. A. 1924, *ApJ*, 60, 15
- Ryabchikova, T., Piskunov, N., Kurucz, R. L., et al. 2015, *Phys. Scr*, 90, 054005
- Saidel, M., Vissapragada, S., Spake, J., et al. 2024, *arXiv e-prints*, arXiv:2404.08736
- Salz, M., Czesla, S., Schneider, P. C., et al. 2018, *A&A*, 620, A97
- Salz, M., Schneider, P. C., Czesla, S., & Schmitt, J. H. M. M. 2015, *A&A*, 576, A42
- Sanz-Forcada, J. & Dupree, A. K. 2008, *A&A*, 488, 715
- Sanz-Forcada, J., Micela, G., Ribas, I., et al. 2011, *A&A*, 532, A6
- Schlaufman, K. C. 2010, *ApJ*, 719, 602
- Schlawin, E., Ilyin, I., Feinstein, A. D., et al. 2021, *RNAAS*, 5, 195
- Seager, S. & Sasselov, D. D. 2000, *ApJ*, 537, 916
- Sicilia, D., Malavolta, L., Pino, L., et al. 2022, *A&A*, 667, A19
- Smette, A., Sana, H., Noll, S., et al. 2015, *A&A*, 576, A77
- Soubiran, C., Jasniewicz, G., Chemin, L., et al. 2018, *A&A*, 616, A7
- Spake, J. J., Oklopčić, A., & Hillenbrand, L. A. 2021, *AJ*, 162, 284
- Spake, J. J., Oklopčić, A., Hillenbrand, L. A., et al. 2022, *ApJ*, 939, L11
- Spake, J. J., Sing, D. K., Evans, T. M., et al. 2018, *Nature*, 557, 68
- Speagle, J. S. 2020, *MNRAS*, 493, 3132
- Stangret, M., Casasayas-Barris, N., Pallé, E., et al. 2022, *A&A*, 662, A101
- Stangret, M., Pallé, E., Casasayas-Barris, N., et al. 2021, *A&A*, 654, A73
- Stefansson, G., Li, Y., Mahadevan, S., et al. 2018, *AJ*, 156, 266
- Suárez Mascareño, A., Damasso, M., Lodieu, N., et al. 2021, *Nature Astronomy*, 6, 232
- Talens, G. J. J., Justesen, A. B., Albrecht, S., et al. 2018, *A&A*, 612, A57
- Turner, O. D., Anderson, D. R., Barkaoui, K., et al. 2019, *MNRAS*, 485, 5790
- Van Eylen, V., Agentoft, C., Lundkvist, M. S., et al. 2018, *MNRAS*, 479, 4786
- Van Eylen, V., Astudillo-Defru, N., Bonfils, X., et al. 2021, *MNRAS*, 507, 2154
- Vidal-Madjar, A., Lecavelier des Etangs, A., Désert, J. M., et al. 2003, *Nature*, 422, 143
- Villarreal D'Angelo, C., Vidotto, A. A., Esquivel, A., Hazra, G., & Youngblood, A. 2021, *MNRAS*, 501, 4383
- Vissapragada, S., Greklek-McKeon, M., Linssen, D., et al. 2024a, *AJ*, 167, 199
- Vissapragada, S., Knutson, H. A., Greklek-McKeon, M., et al. 2022a, *AJ*, 164, 234
- Vissapragada, S., Knutson, H. A., Greklek-McKeon, M., et al. 2022b, *AJ*, 164, 234
- Vissapragada, S., Knutson, H. A., Jovanovic, N., et al. 2020, *AJ*, 159, 278
- Vissapragada, S., McCreery, P., Dos Santos, L. A., et al. 2024b, *ApJ*, 962, L19
- Vissapragada, S., Stefánsson, G., Greklek-McKeon, M., et al. 2021, *AJ*, 162, 222
- von Braun, K., Boyajian, T. S., ten Brummelaar, T. A., et al. 2011, *ApJ*, 740, 49
- Šubjak, J., Endl, M., Chaturvedi, P., et al. 2022, *A&A*, 662, A107
- Wang, L. & Dai, F. 2018, *ApJ*, 860, 175
- West, R. G., Hellier, C., Almenara, J. M., et al. 2016, *A&A*, 585, A126
- Wildi, F., Bouchy, F., Doyon, R., et al. 2022, in *Society of Photo-Optical Instrumentation Engineers (SPIE) Conference Series*, Vol. 12184, *Ground-based and Airborne Instrumentation for Astronomy IX*, ed. C. J. Evans, J. J. Bryant, & K. Motohara, 121841H
- Winn, J. N., Fabrycky, D., Albrecht, S., & Johnson, J. A. 2010, *ApJ*, 718, L145
- Wolfgang, A., Rogers, L. A., & Ford, E. B. 2016, *ApJ*, 825, 19
- Wright, N. J., Drake, J. J., Mamajek, E. E., & Henry, G. W. 2011, *ApJ*, 743, 48
- Wytenbach, A., Ehrenreich, D., Lovis, C., Udry, S., & Pepe, F. 2015, *A&A*, 577, A62
- Yan, F. & Henning, T. 2018, *Nature Astronomy*, 2, 714
- Zahnle, K. 1998, in *Astronomical Society of the Pacific Conference Series*, Vol. 148, *Origins*, ed. C. E. Woodward, J. M. Shull, & J. Thronson, Harley A., 364
- Zahnle, K. J. & Catling, D. C. 2017, *ApJ*, 843, 122
- Zechmeister, M., Anglada-Escudé, G., & Reiners, A. 2014, *A&A*, 561, A59
- Zechmeister, M. & Kürster, M. 2009, *A&A*, 496, 577
- Zechmeister, M., Reiners, A., Amado, P. J., et al. 2018, *A&A*, 609, A12
- Zeng, L., Jacobsen, S. B., Sasselov, D. D., et al. 2019, *Proceedings of the National Academy of Science*, 116, 9723
- Zhang, M., Cauley, P. W., Knutson, H. A., et al. 2022a, *AJ*, 164, 237
- Zhang, M., Dai, F., Bean, J. L., Knutson, H. A., & Rescigno, F. 2023a, *ApJ*, 953, L25
- Zhang, M., Knutson, H. A., Dai, F., et al. 2023b, *AJ*, 165, 62
- Zhang, M., Knutson, H. A., Wang, L., Dai, F., & Barragán, O. 2022b, *AJ*, 163, 67
- Zhang, M., Knutson, H. A., Wang, L., et al. 2022c, *AJ*, 163, 68
- Zhang, M., Knutson, H. A., Wang, L., et al. 2021, *AJ*, 161, 181
- Zhang, Z., Morley, C. V., Gully-Santiago, M., et al. 2023c, *Science Advances*, 9, eadf8736
- Zicher, N., Barragán, O., Klein, B., et al. 2022, *MNRAS*, 512, 3060

²⁴ Hamburger Sternwarte, Gojenbergsweg 112, 21029 Hamburg, Germany

²⁵ Centro Astronómico Hispano en Andalucía, Observatorio Astronómico de Calar Alto, Sierra de los Filabres, 04550 Gérgal, Almería, Spain

Appendix A: Additional figures**Appendix B: V1298 Tau extra material**

Table B.1: Prior and posterior distributions from the nested sampling fitting for V1298 Tau c H α feature (see Fig. A.2). Prior label \mathcal{U} represents uniform distribution.

| Parameter | Prior | Posterior |
|-----------------------------------|---------------------------|---------------------------|
| Absorption [%] | $\mathcal{U}(-2, 0)$ | -1.10 ± 0.13 |
| λ_0 [\AA] | $\mathcal{U}(6560, 6570)$ | $6564.90^{+0.11}_{-0.10}$ |
| σ [\AA] | $\mathcal{U}(0, 1)$ | $0.55^{+0.10}_{-0.08}$ |
| Δv [km s^{-1}] | – | 12^{+5}_{-4} |
| FWHM [\AA] | – | $1.30^{+0.24}_{-0.17}$ |
| EW [m\AA] | – | $14.8^{+1.7}_{-1.6}$ |

Table B.2: Prior and posterior distributions from the nested sampling fitting for V1298 Tau c He I feature (see Fig. A.2). Prior label \mathcal{U} represents uniform distribution.

| Parameter | Prior | Posterior |
|-----------------------------------|-----------------------------|----------------------|
| Absorption [%] | $\mathcal{U}(-4.5, 4.5)$ | -3.75 ± 0.12 |
| λ_0 [\AA] | $\mathcal{U}(10830, 10835)$ | 10832.18 ± 0.04 |
| σ [\AA] | $\mathcal{U}(0.0, 2)$ | 1.02 ± 0.04 |
| Δv [km s^{-1}] | – | -28.7 ± 1.1 |
| FWHM [\AA] | – | 2.40 ± 0.10 |
| EW [m\AA] | – | $95.9^{+3.2}_{-3.0}$ |

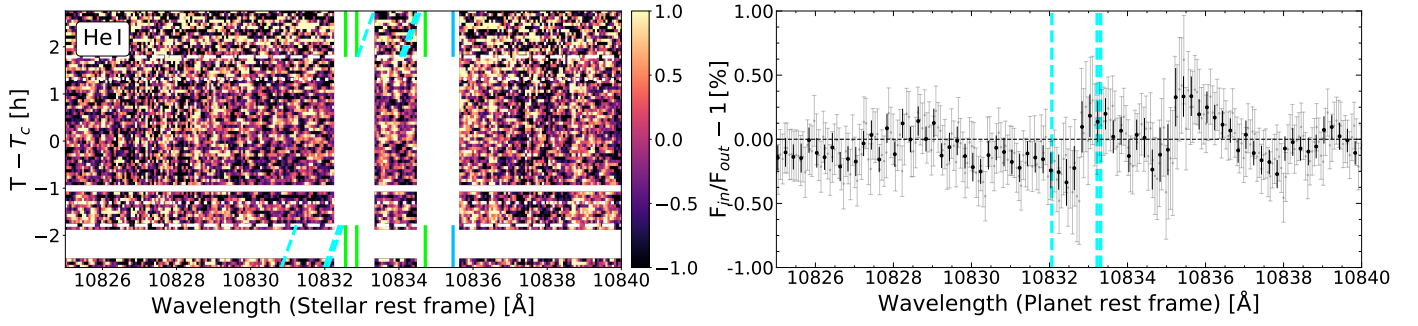


Fig. A.1: Same as Fig. 1, but for MASCARA-2 b observations with CARMENES.

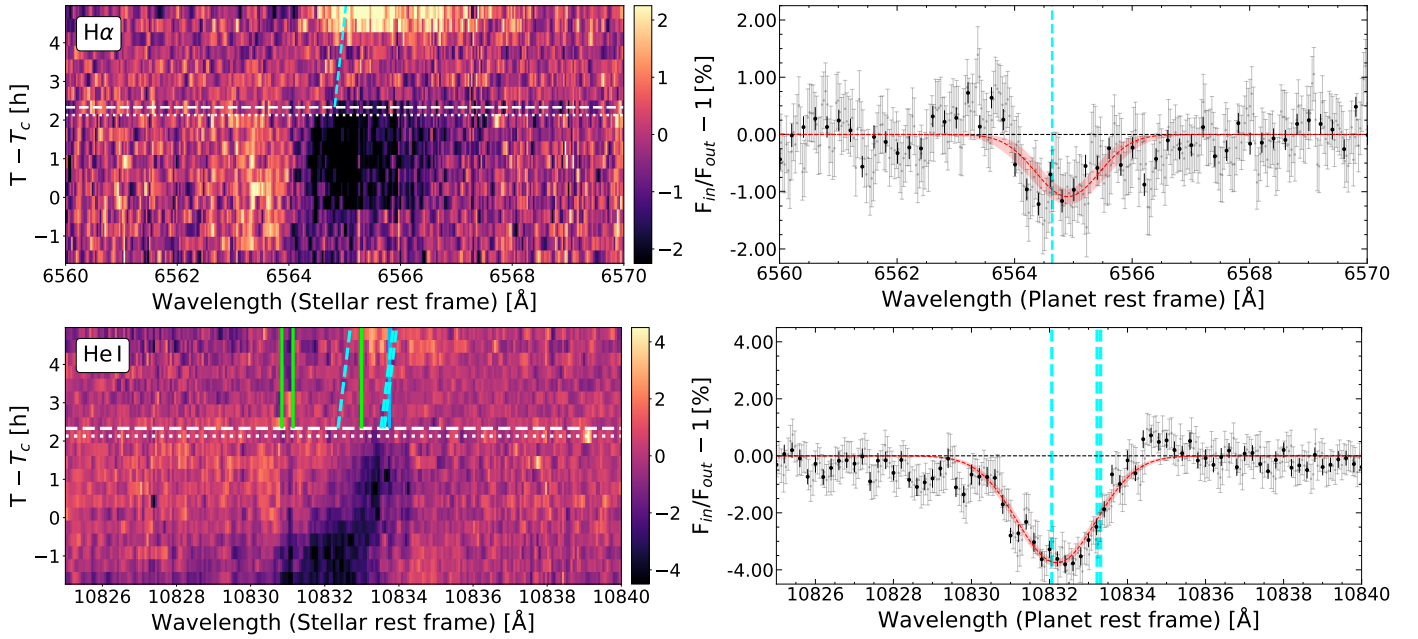


Fig. A.2: Same as Fig. 1, but for V1298 Tau c observations with CARMENES.

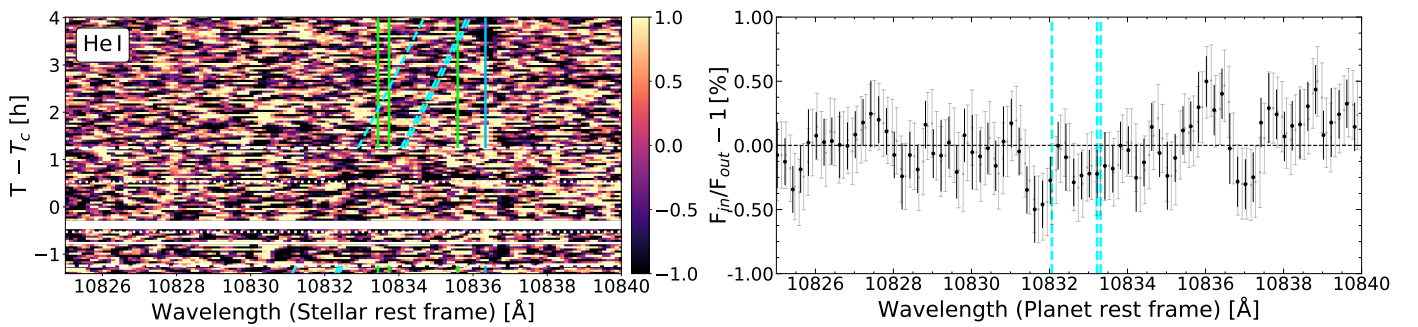


Fig. A.3: Same as Fig. 1, but for TOI-1431 b observations with CARMENES.

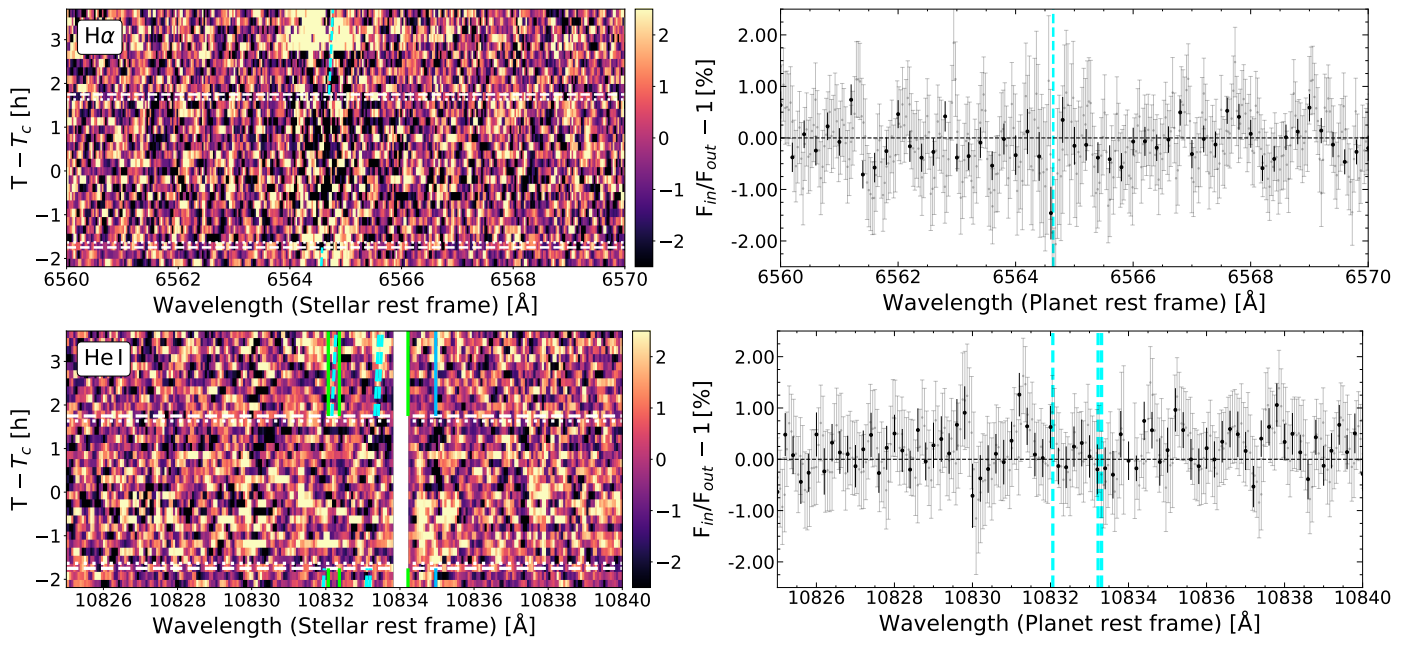


Fig. A.4: Same as Fig. 1, but for TOI-2048 b observations with CARMENES.

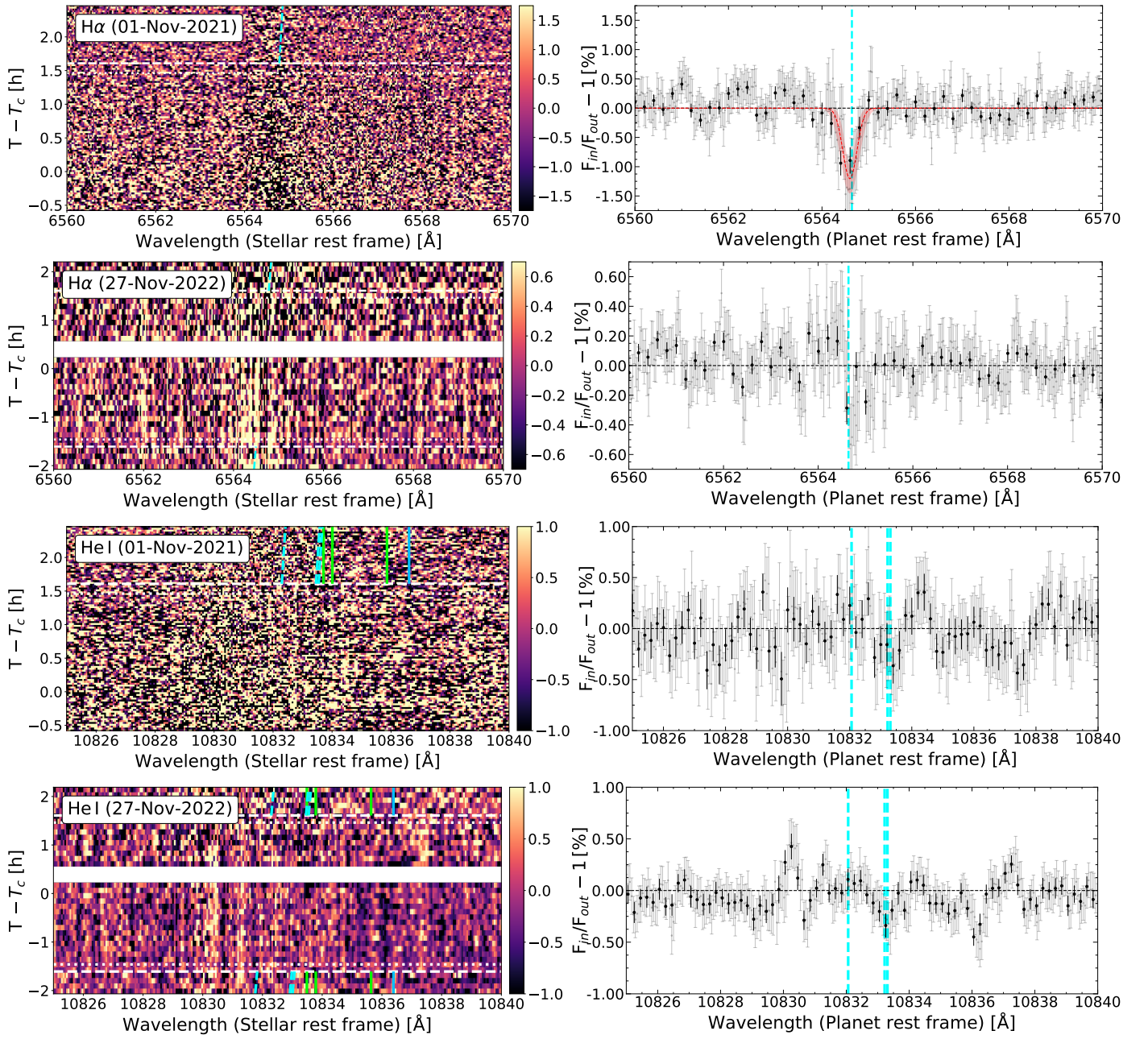


Fig. A.5: Same as Fig. 1, but for HD 63433 b observations with CARMENES.

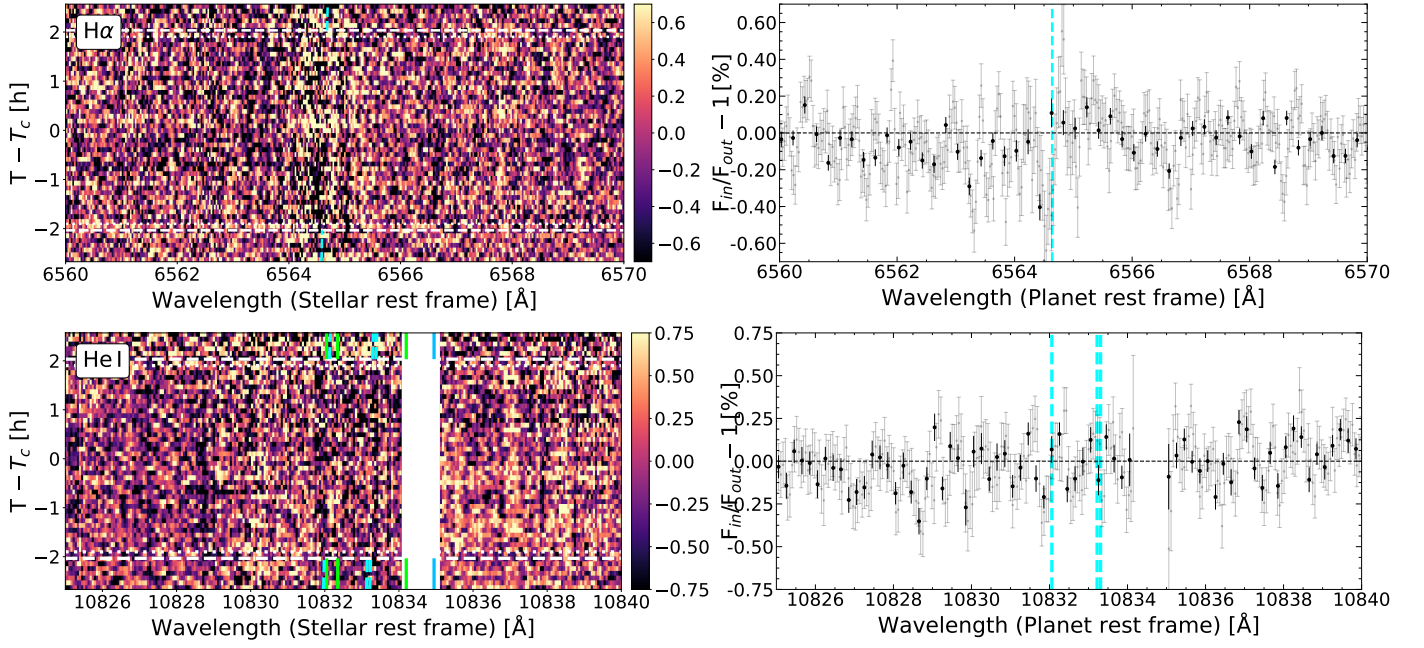


Fig. A.6: Same as Fig. 1, but for HD 63433 c observations with CARMENES.

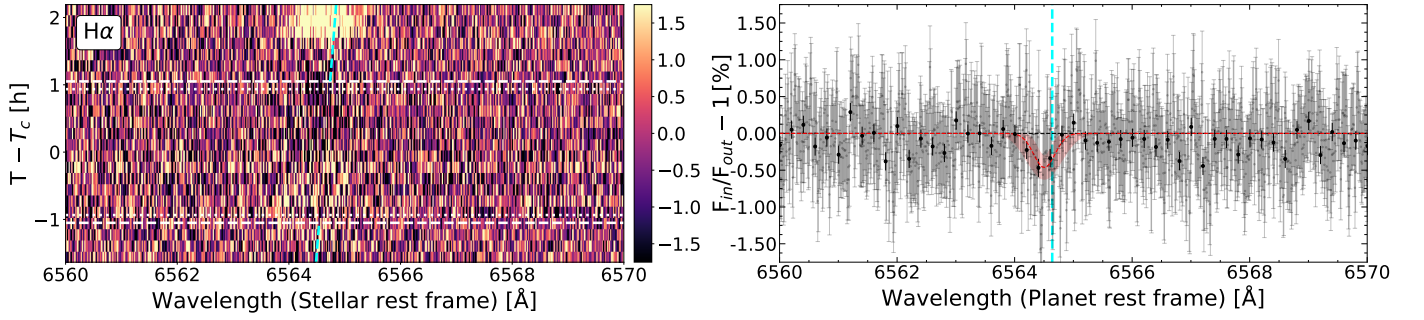


Fig. A.7: Same as Fig. 1, but for HD 73583 b observations with HARPS-N.

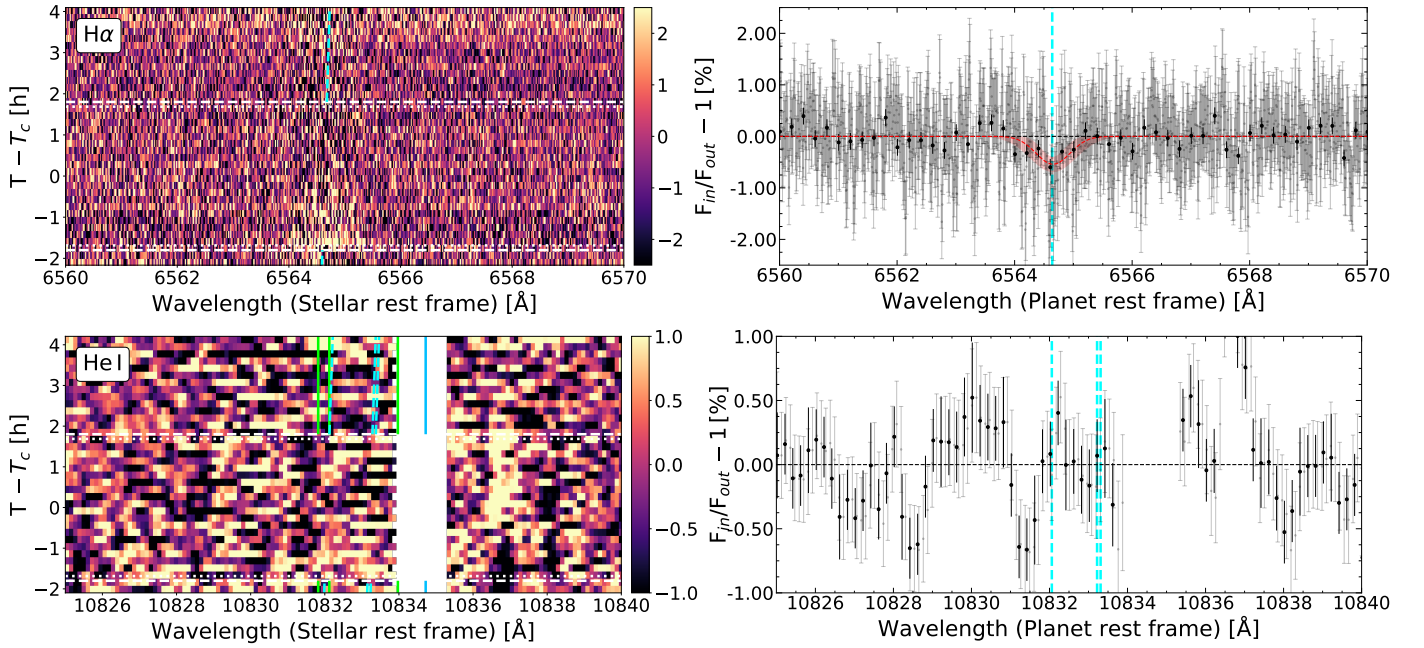


Fig. A.8: Same as Fig. 1, but for HD 73583 c observations with GIARPS.

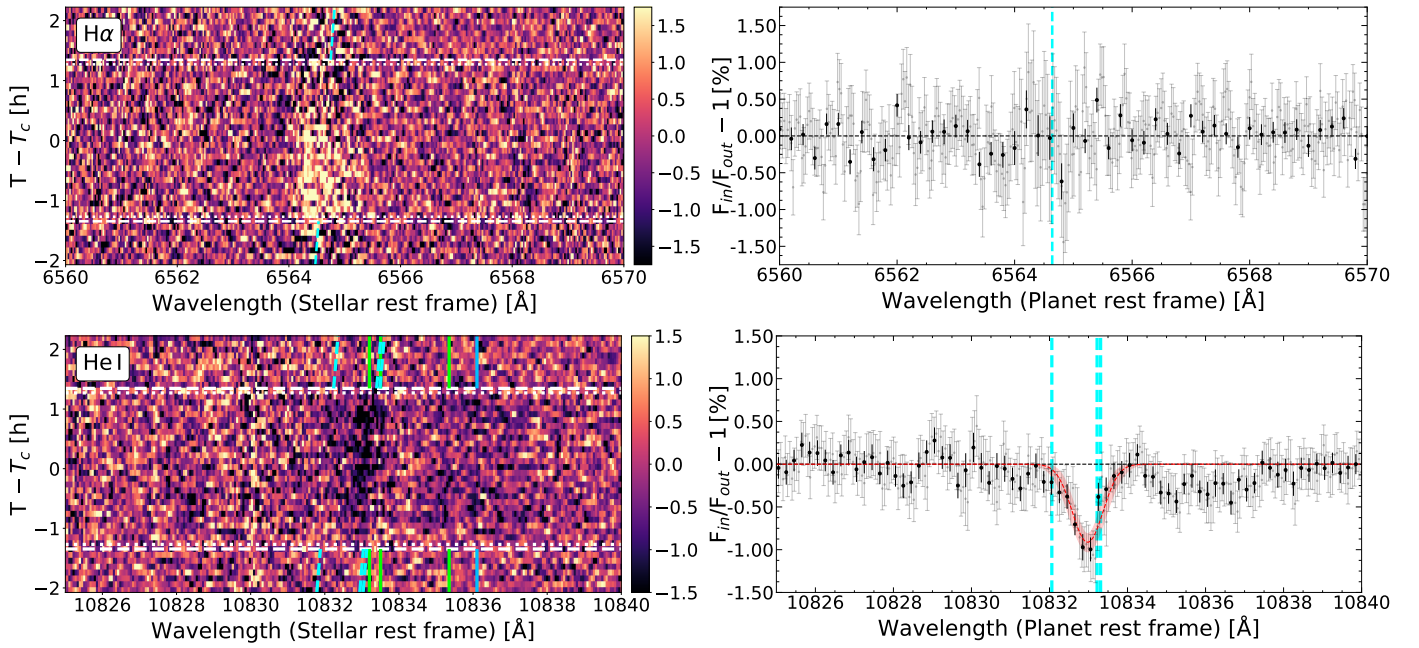


Fig. A.9: Same as Fig. 1, but for HD 235088 b observations with CARMENES.

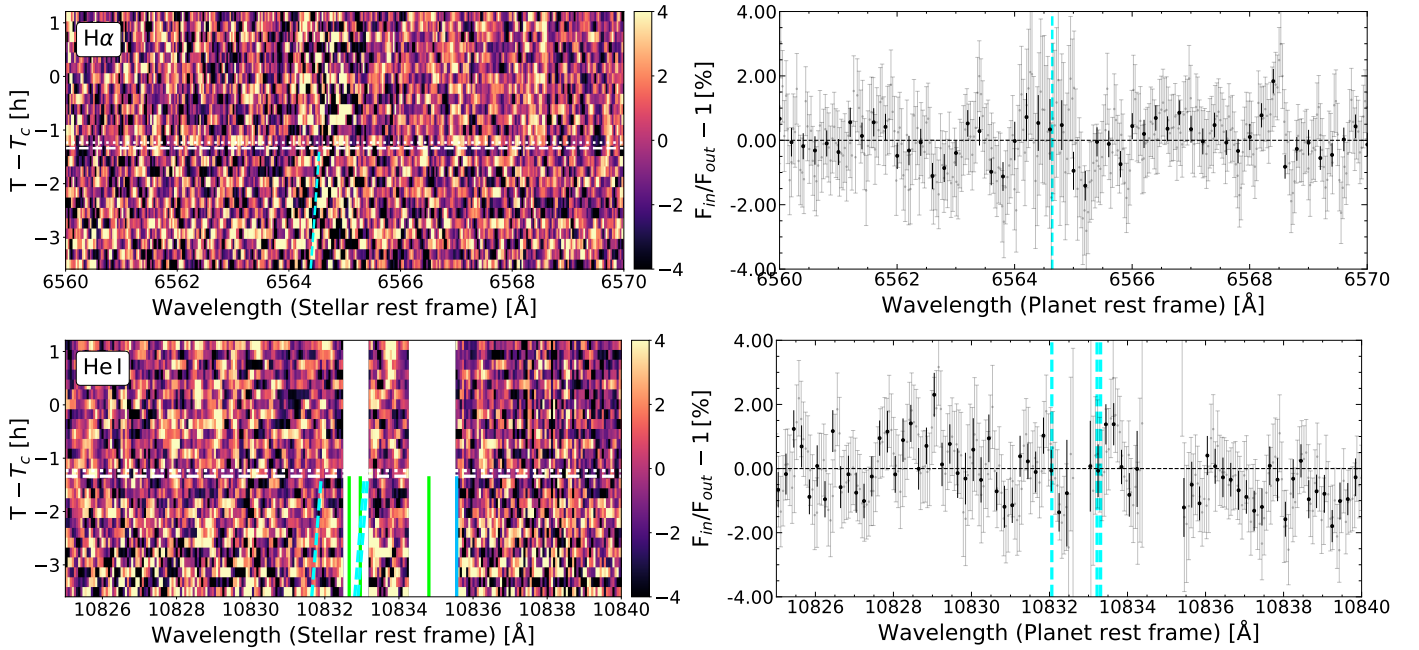


Fig. A.10: Same as Fig. 1, but for K2-77 b observations with CARMENES.

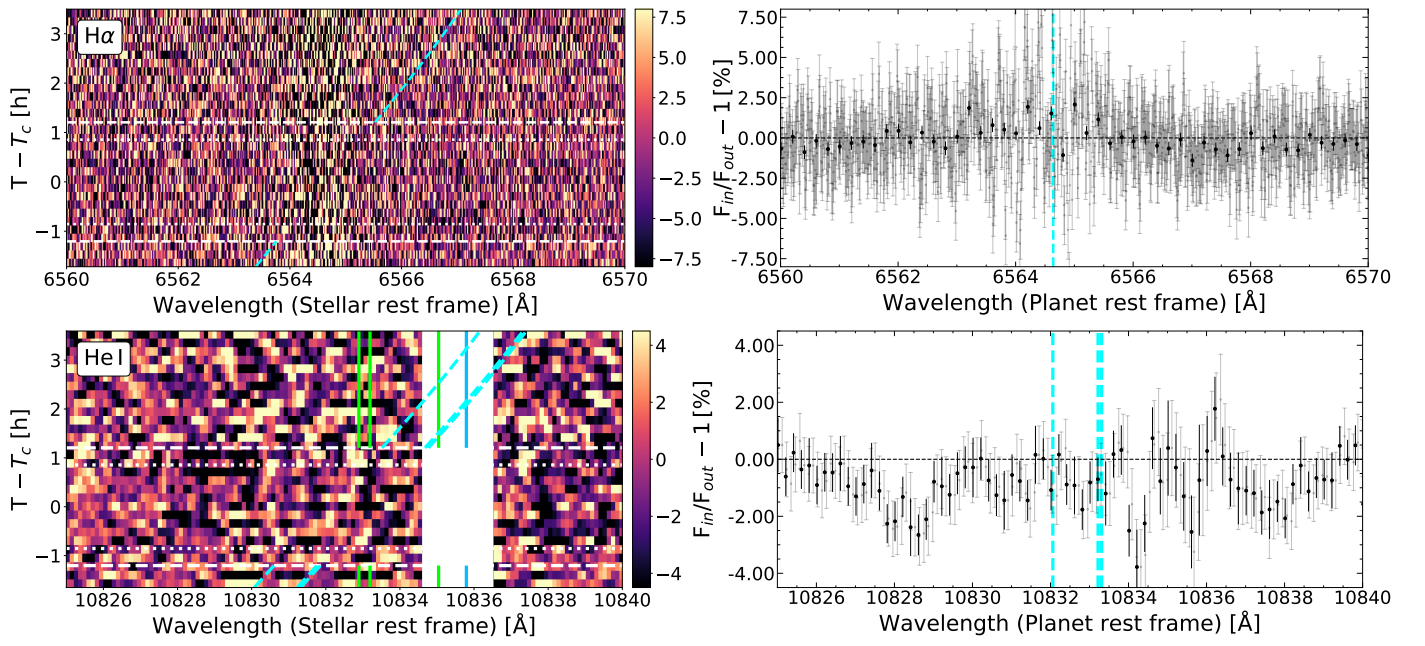


Fig. A.11: Same as Fig. 1, but for TOI-2046 b observations with GIARPS.

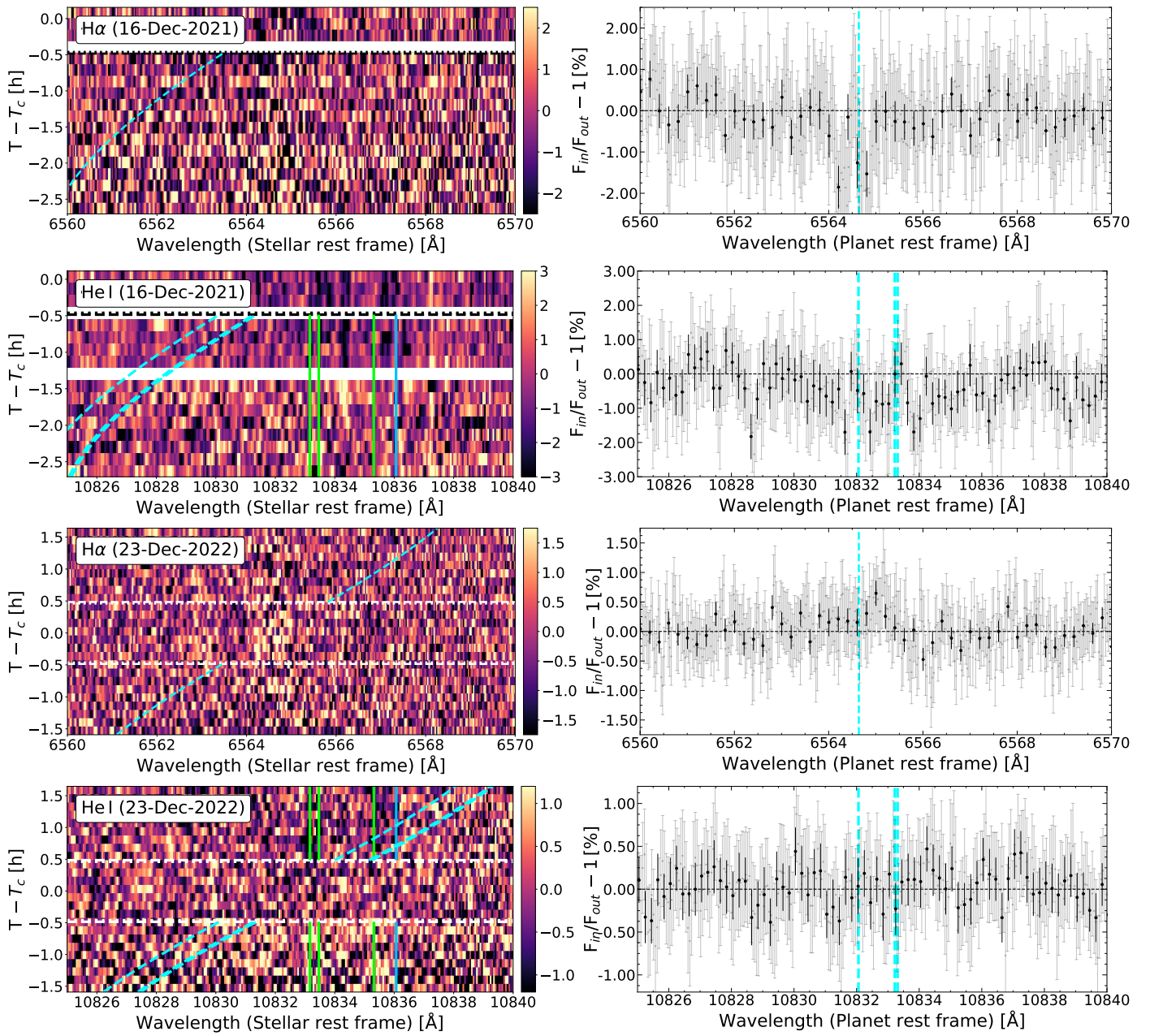


Fig. A.12: Same as Fig. 1, but for TOI-1807 b observations with CARMENES.

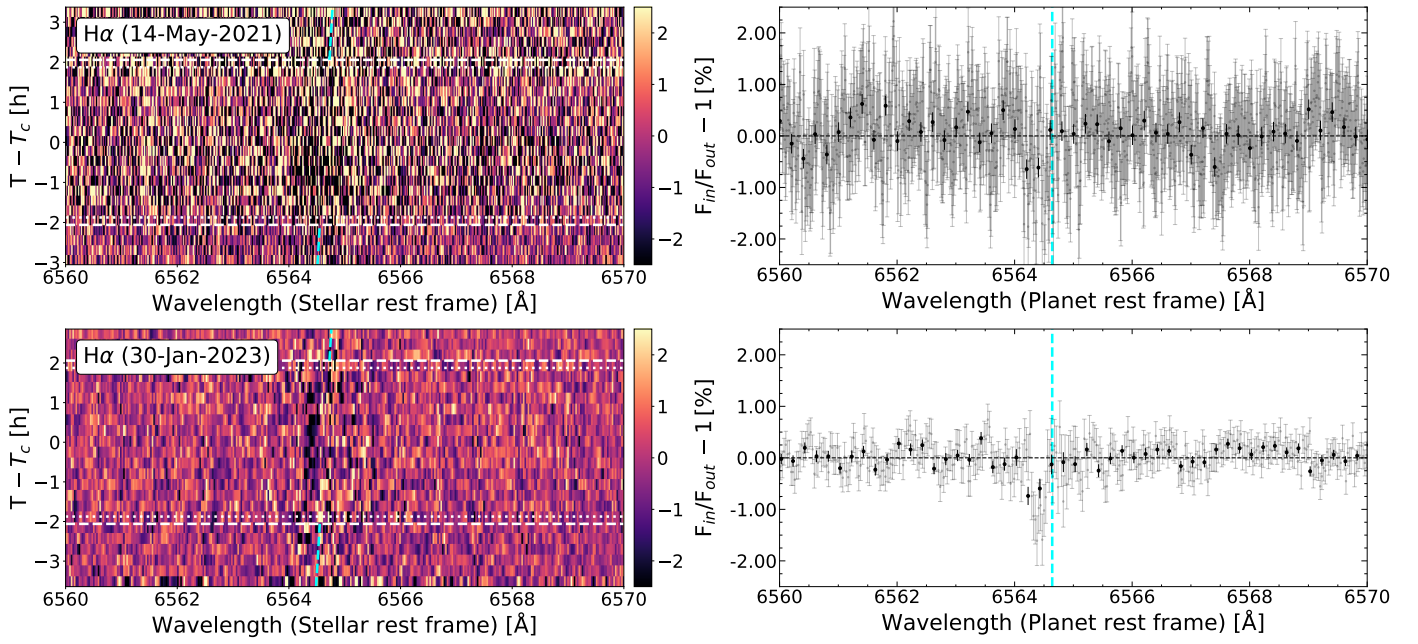


Fig. A.13: Same as Fig. 1 for TOI-1136 d $H\alpha$ observations with HARPS-N (14-May-2021) and CARMENES VIS (30-Jan-2023).

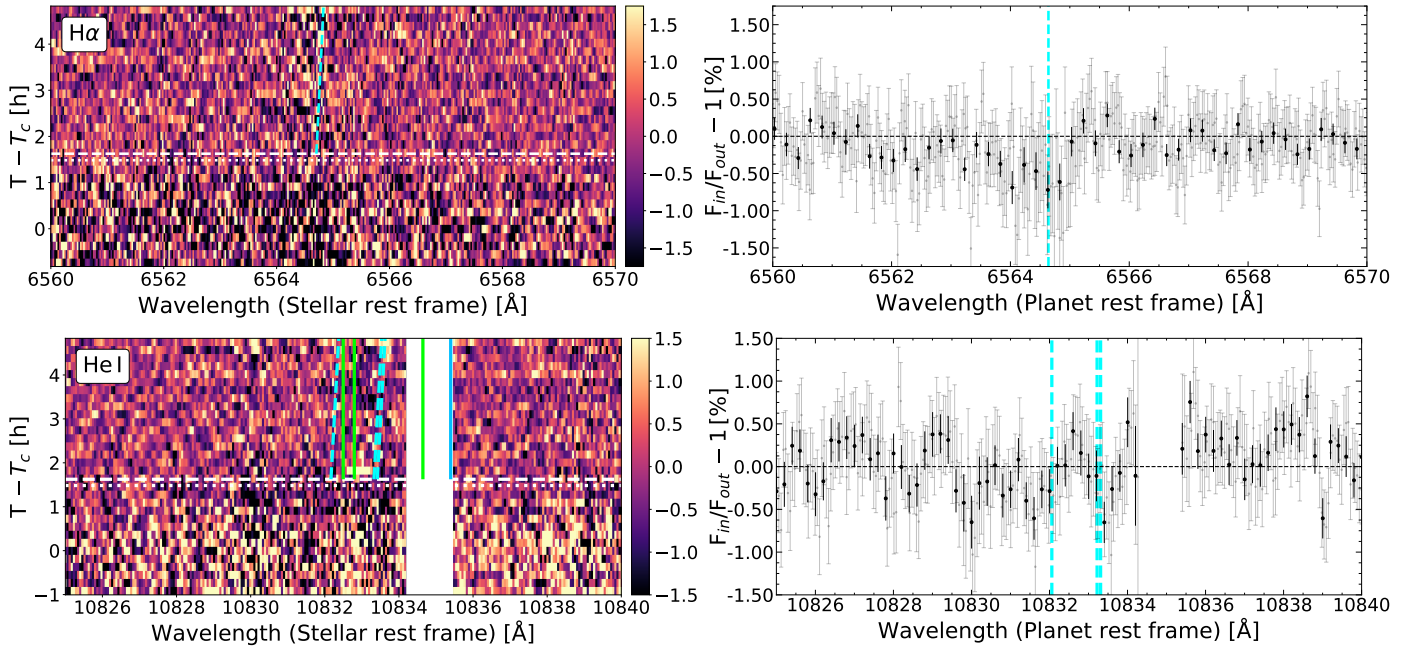


Fig. A.14: Same as Fig. 1, but for TOI-2076 b observations with CARMENES.

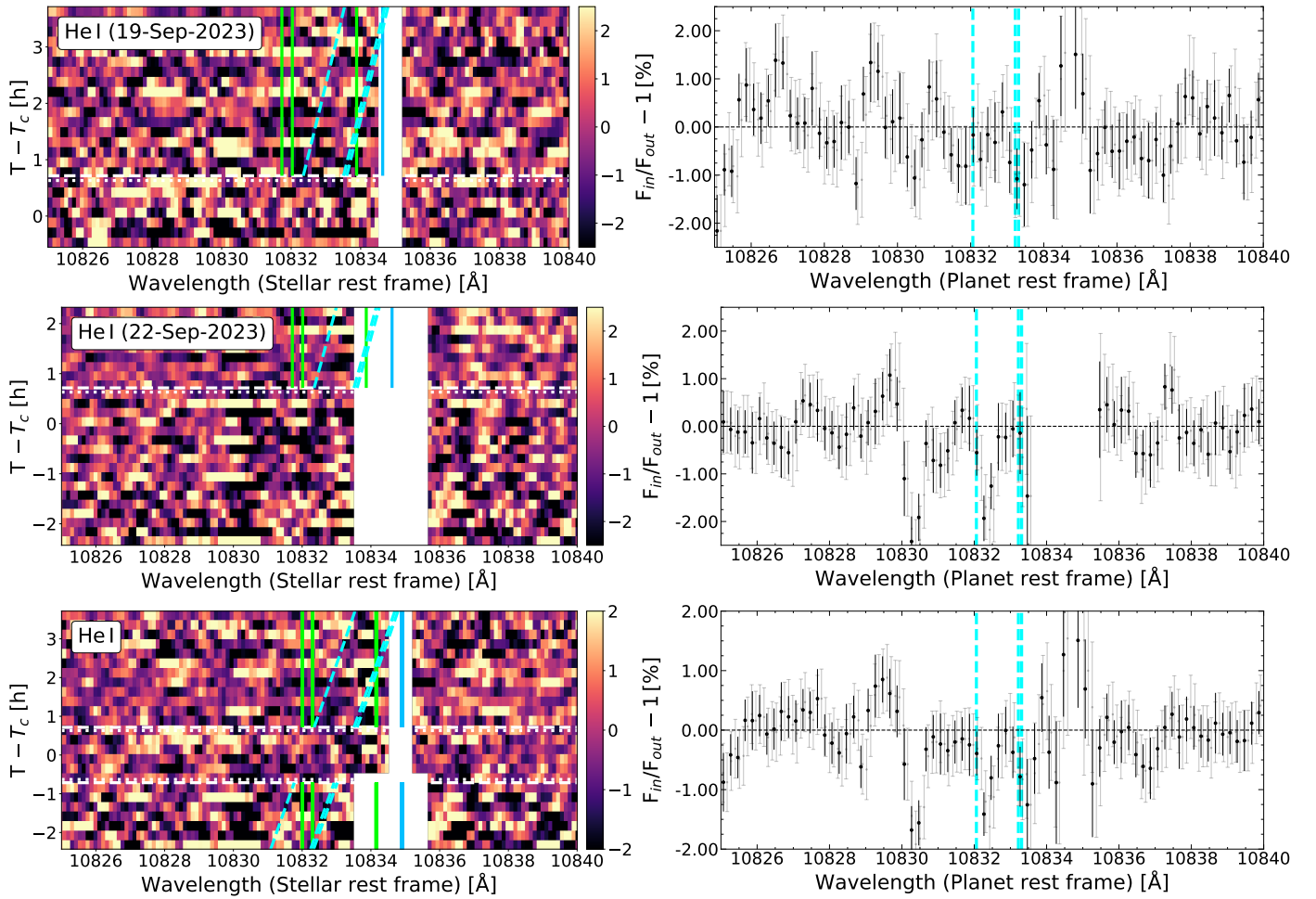


Fig. A.15: Same as Fig. 1, but for TOI-1683 b observations with GIANO-B.

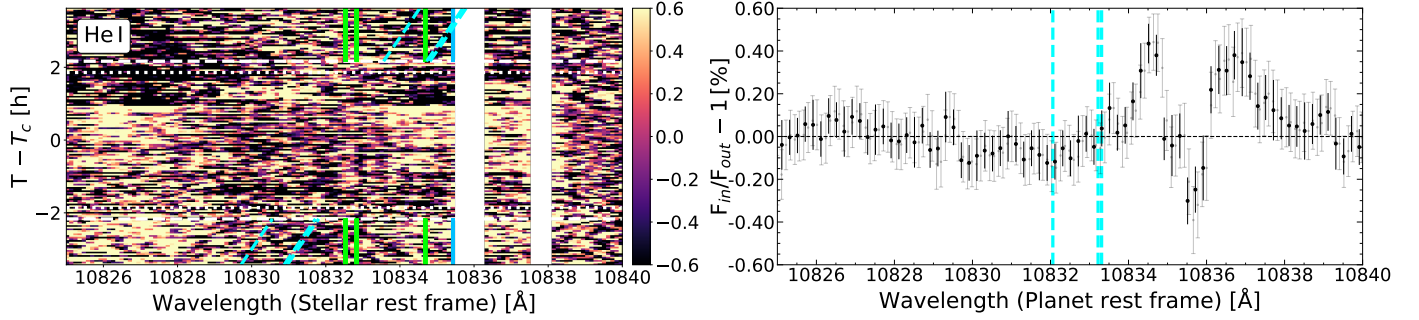


Fig. A.16: Same as Fig. 1, but for WASP-189 b observations with GIANO-B.

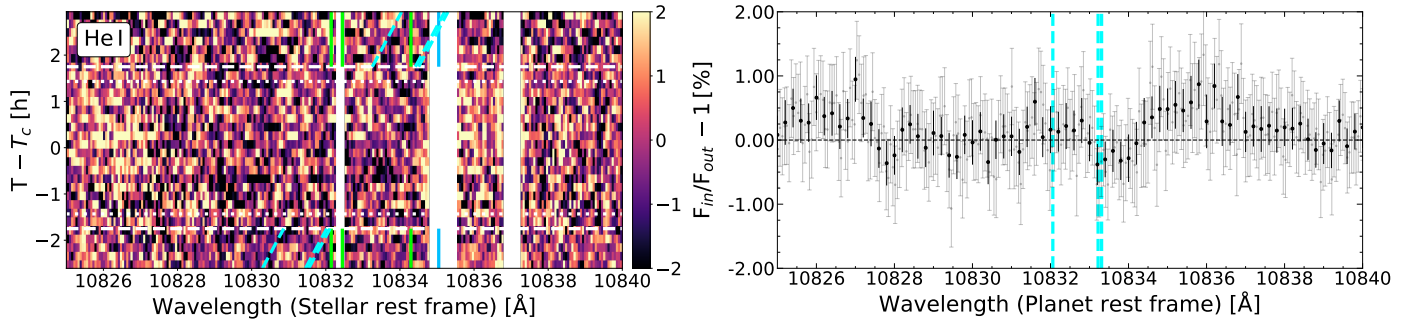


Fig. A.17: Same as Fig. 1, but for HAT-P-57 b observations with CARMENES.

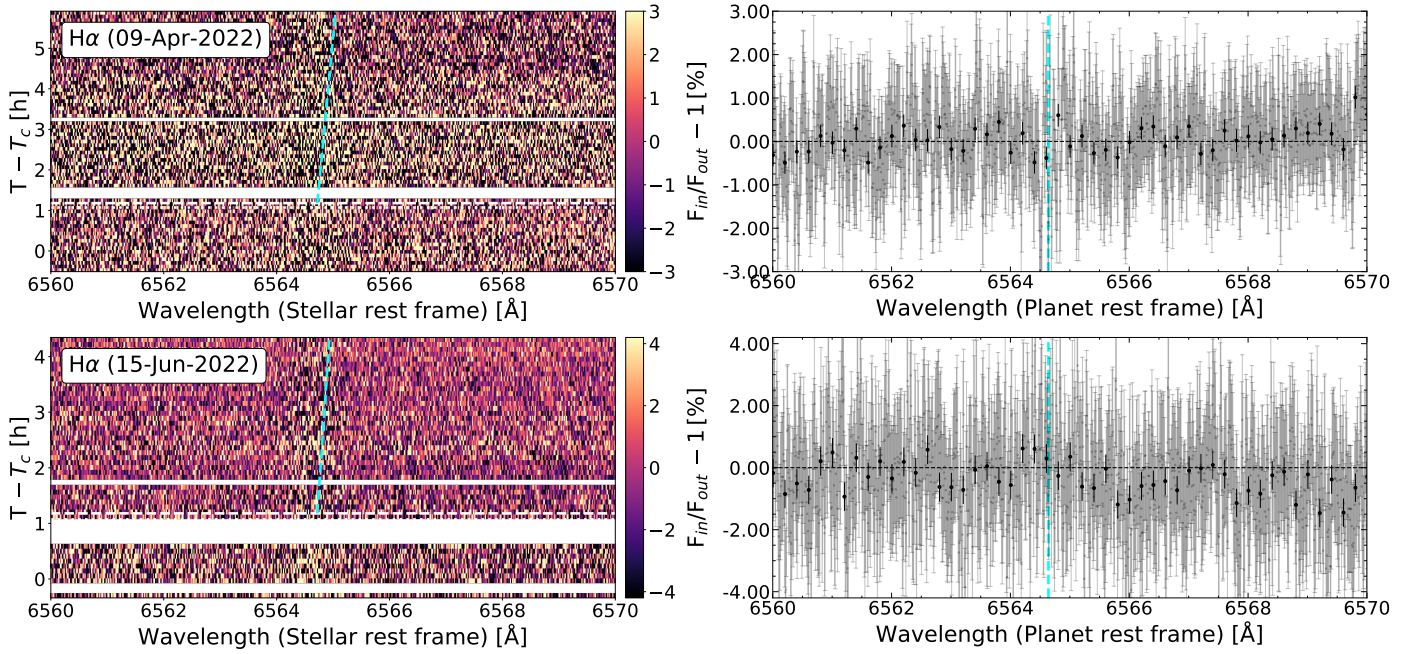


Fig. A.18: Same as Fig. 1, but for TOI-218 b individual observations of H α with HARPS-N.

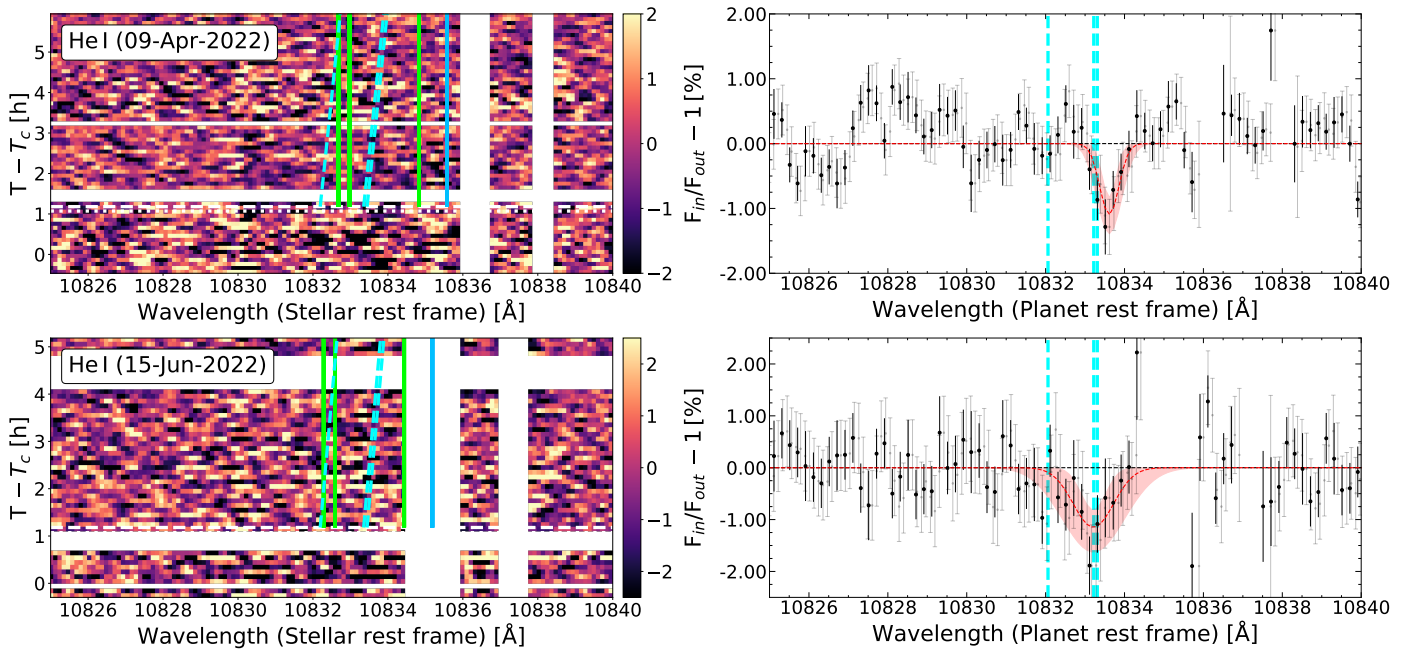


Fig. A.19: Same as Fig. 1, but for TOI-218 b individual observations of He I triplet with GIANO-B.

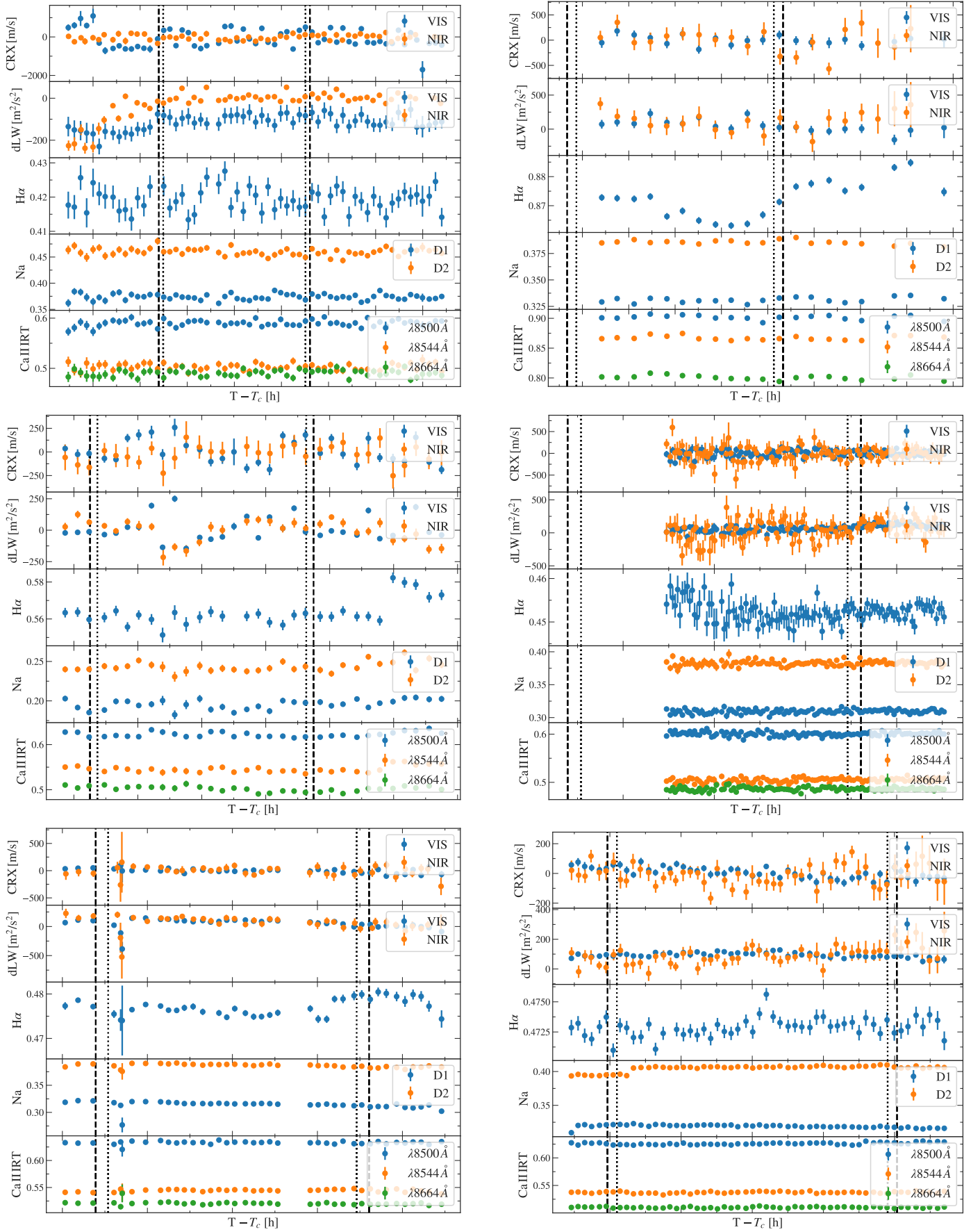


Fig. A.20: Time evolution of the activity indicators for K2-100 b (top left), V1298 Tau c (top right), TOI-2048 b (middle left), HD 63433 b (1 November 2021, middle right; and 27 November 2022, bottom left), and HD 63433 c (bottom right). The vertical dashed and dotted lines represent the different contacts during the transit.

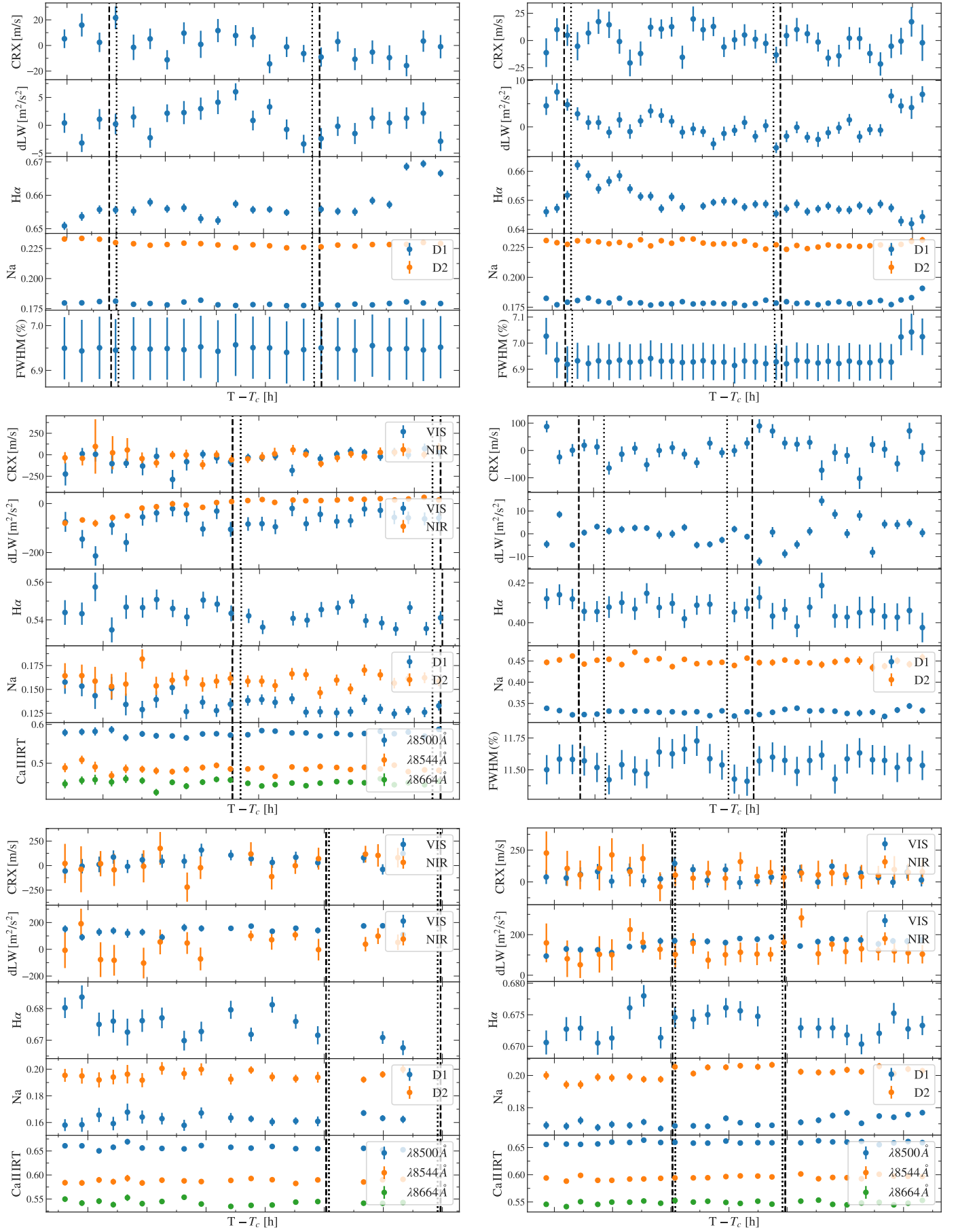


Fig. A.21: Same as Fig. A.20, but for HD 73583 b (top left), HD 73583 b (top right), K2-77 b (middle left), TOI-2046 b (middle right), and TOI-1807 b (16 December 2021, bottom left; and 23 December 2022, bottom right).

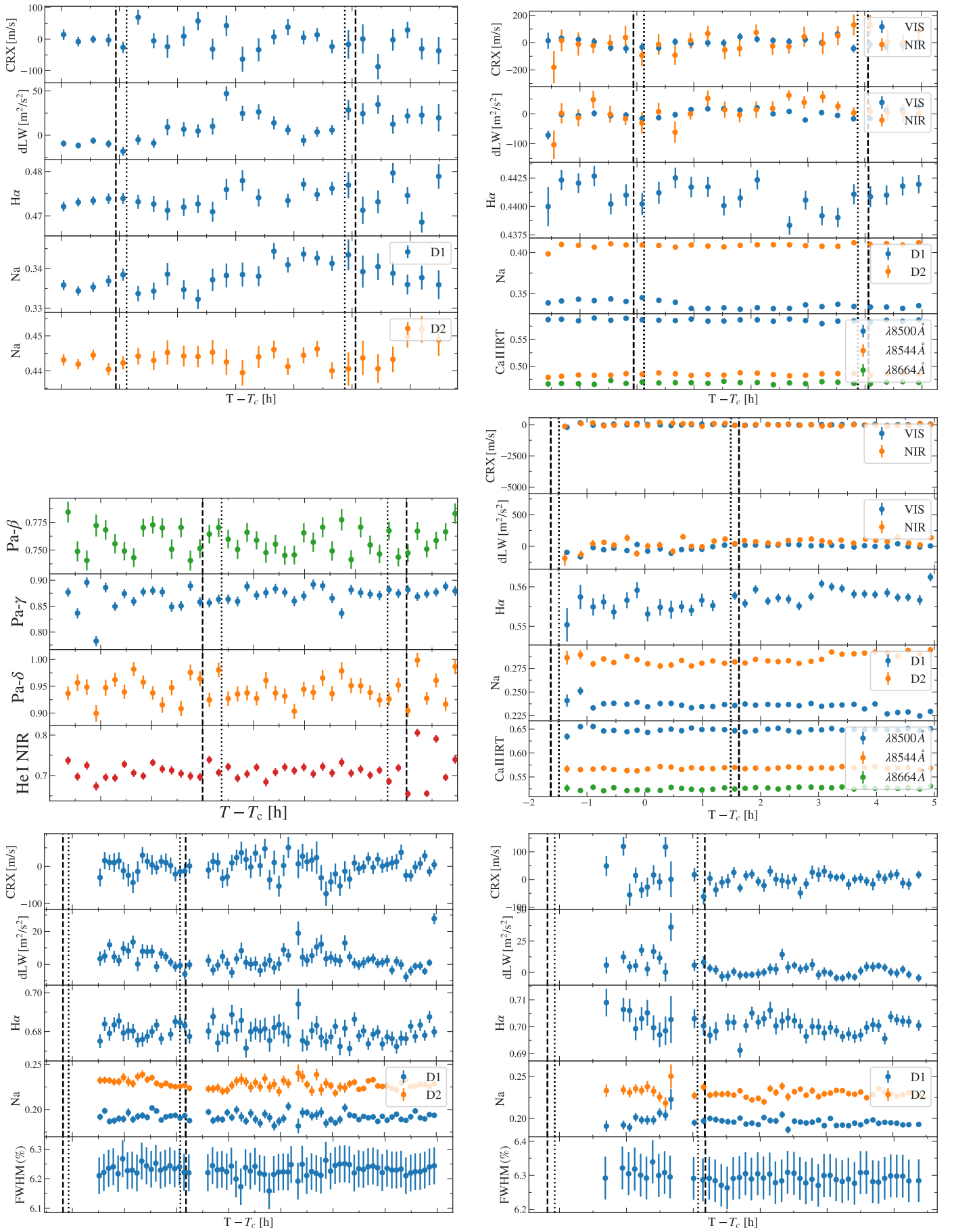


Fig. A.22: Same as Fig. A.20, but for TOI-1136 d (14 May 2021, top left; and 30 January 2023, top right), TOI-1268 b (middle left), and TOI-2076 b (middle right), and TOI-1818 b (9 April 2022, bottom left; and 15 June 2022, bottom right).

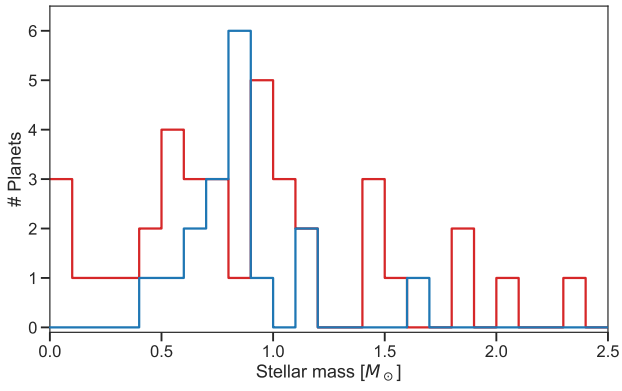


Fig. A.23: Histogram of He I triplet observations (detections: blue, non-detections: red) as a function of stellar mass.

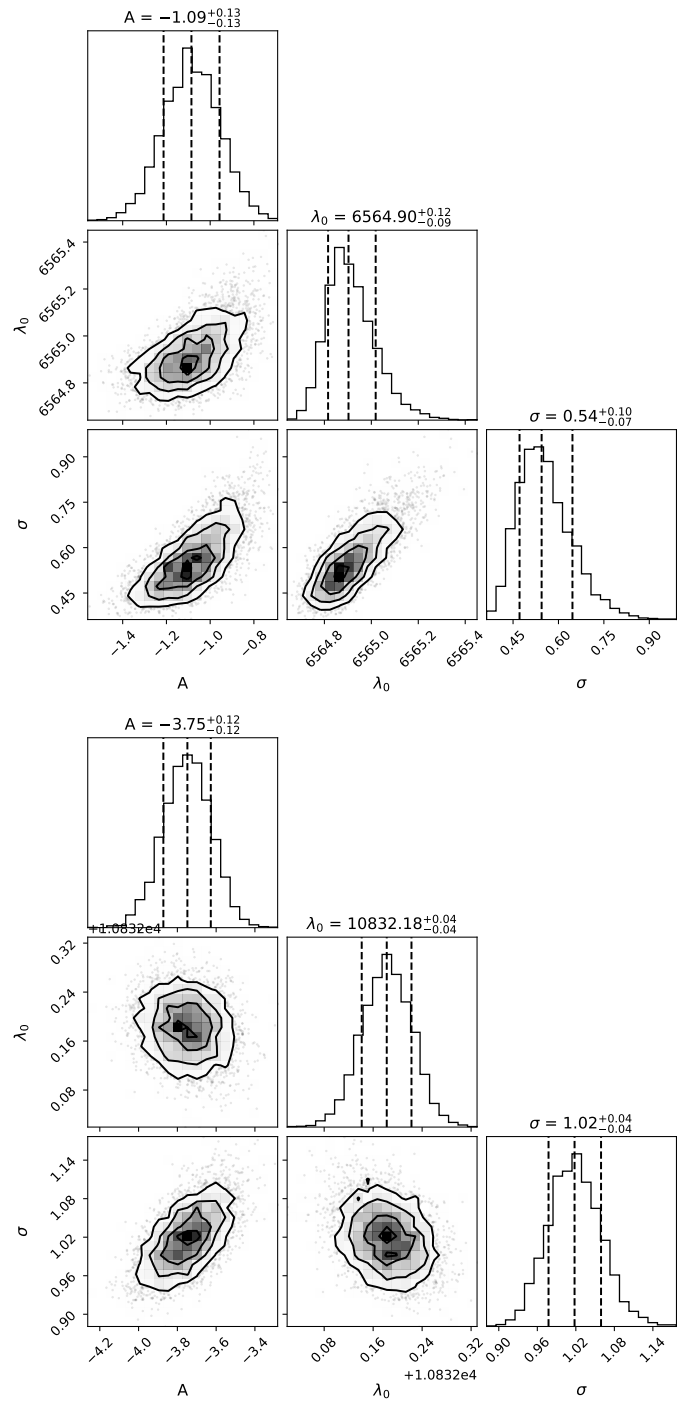


Fig. B.1: Corner plot for the nested sampling posterior distribution of V1298 Tau c H α (left) and He I (right) feature.

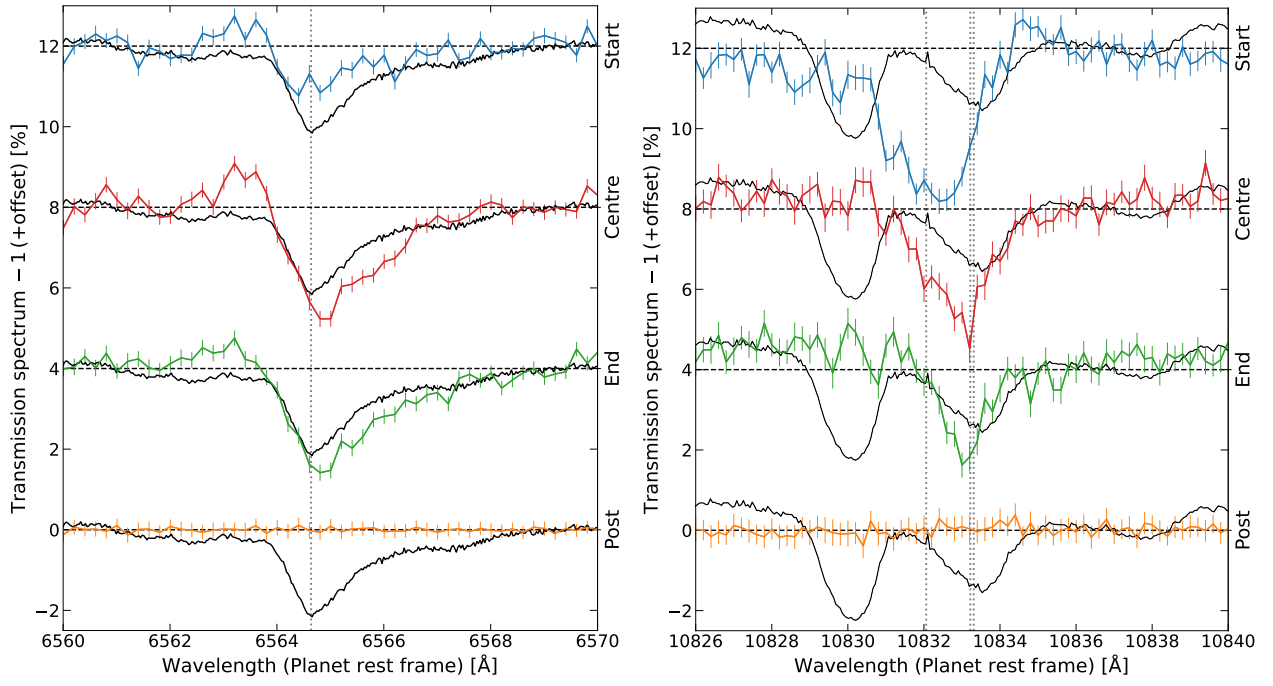


Fig. B.2: TS around the $H\alpha$ (left) and $He\ I$ triplet (right) lines for the transit phases from top to bottom (consecutively offset): start (blue), centre (red), end (green), and post-transit (orange). Master-Out spectrum is overplotted in black along with the individual TS for comparison. The dotted vertical lines indicate the lines positions. The wavelengths in this figure are given in vacuum.

Appendix C: TOI-2048 extra material

We analysed the TESS data from Sectors 16, 23, 24, 50, and 51 with the procedure described in Sect. 2.2. We used the `celerite` GP quasi-periodic kernel to account for the young star variability and we adopted the stellar parameters from [Newton et al. \(2022\)](#) for a proper comparison.

The fitted parameters with their prior and posterior values, and the derived parameters for TOI-2048 b are shown in Table C.1. The TESS data along with the best transiting and GP models is shown in Fig. C.1 and TOI-2048 b phase folded transit is shown in Fig. C.2. We obtained similar results using the `celerite` GP exponential kernel.

To derive an estimation of TOI-2048 b’s semi-amplitude K_* , first we forecasted its mass using the probabilistic mass-radius relationship for sub-Neptune-sized planets ($R_p < 4 R_\oplus$) of [Wolfgang et al. \(2016\)](#). We predicted a planetary mass of $\sim 9 \pm 2 M_\oplus$, which is translated into $K_* \simeq 2.8 \pm 0.6 \text{ m s}^{-1}$ using the equation

$$K_* = 28.4 \text{ m s}^{-1} (P_{\text{pl}}/\text{year})^{-1/3} (M_{\text{pl}}/M_{\text{Jup}}) (M_*/M_\odot)^{-2/3} \quad (\text{C.1})$$

Table C.1: Prior and posterior distributions from the `juliet` fitting for TOI-2048 b. Prior labels \mathcal{U} , \mathcal{N} , \mathcal{F} , and \mathcal{J} represents uniform, normal, fixed, and Jeffrey’s distribution, respectively.

| Parameter | Prior | Posterior |
|-------------------------------------|--------------------------------|---|
| P [d] | $\mathcal{N}(13.7905, 0.0001)$ | 13.790546 (55) |
| $t_0^{(a)}$ | $\mathcal{N}(1739.11, 0.01)$ | 1739.1123 (27) |
| ecc | $\mathcal{F}(0)$ | – |
| ω (deg) | $\mathcal{F}(90)$ | – |
| r_1 | $\mathcal{U}(0, 1)$ | 0.54±0.12 |
| r_2 | $\mathcal{U}(0, 1)$ | 0.0306±0.0018 |
| ρ_* [kg m^{-3}] | $\mathcal{N}(2367.0, 500.0)$ | 2552 ⁺³⁵⁰ ₋₄₂₀ |
| μ_{TESS} (ppm) | $\mathcal{N}(0.0, 0.1)$ | –100 ⁺²⁰⁰ ₋₁₈₀ |
| σ_{TESS} (ppm) | $\mathcal{J}(10^{-6}, 10^6)$ | 5600 ⁺¹⁴⁰⁰⁰ ₋₅₆₀₀ |
| $q_{1,TESS}$ | $\mathcal{U}(0, 1)$ | 0.51±0.28 |
| $q_{2,TESS}$ | $\mathcal{U}(0, 1)$ | 0.46±0.30 |
| GP_B (ppm) | $\mathcal{J}(10^{-6}, 10^6)$ | 33 ⁺¹⁶ ₋₁₀ |
| GP_L [d] | $\mathcal{J}(10^{-3}, 10^3)$ | 43.5 ⁺²⁰ ₋₁₂ |
| GP_C (ppm) | $\mathcal{J}(10^{-6}, 10^6)$ | 200 ⁺⁴⁰⁰⁰⁰ ₋₁₈₀ |
| GP_{rot} [d] | $\mathcal{N}(8, 2)$ | 7.48±0.12 |
| <i>Derived planetary parameters</i> | | |
| $p = R_p/R_*$ | | 0.0306±0.0018 |
| $b = (a_p/R_*) \cos i_p$ | | 0.30 ^{+0.16} _{-0.18} |
| i_p (deg) | | 89.41±0.35 |
| T_{14} [h] | | 3.5±0.1 |
| T_{12} [min] | | 6.9 ^{+1.2} _{-0.7} |
| R_p [R_\oplus] | | 2.60±0.20 |
| a_p [AU] | | 0.1078±0.0080 |
| T_{eq} [K] ^(b) | | 675 ⁺²² ₋₁₆ |

Notes. ^(a) Central time of transit (t_0) units are BJD – 2 457 000. ^(b) Equilibrium temperatures were calculated assuming zero Bond albedo.

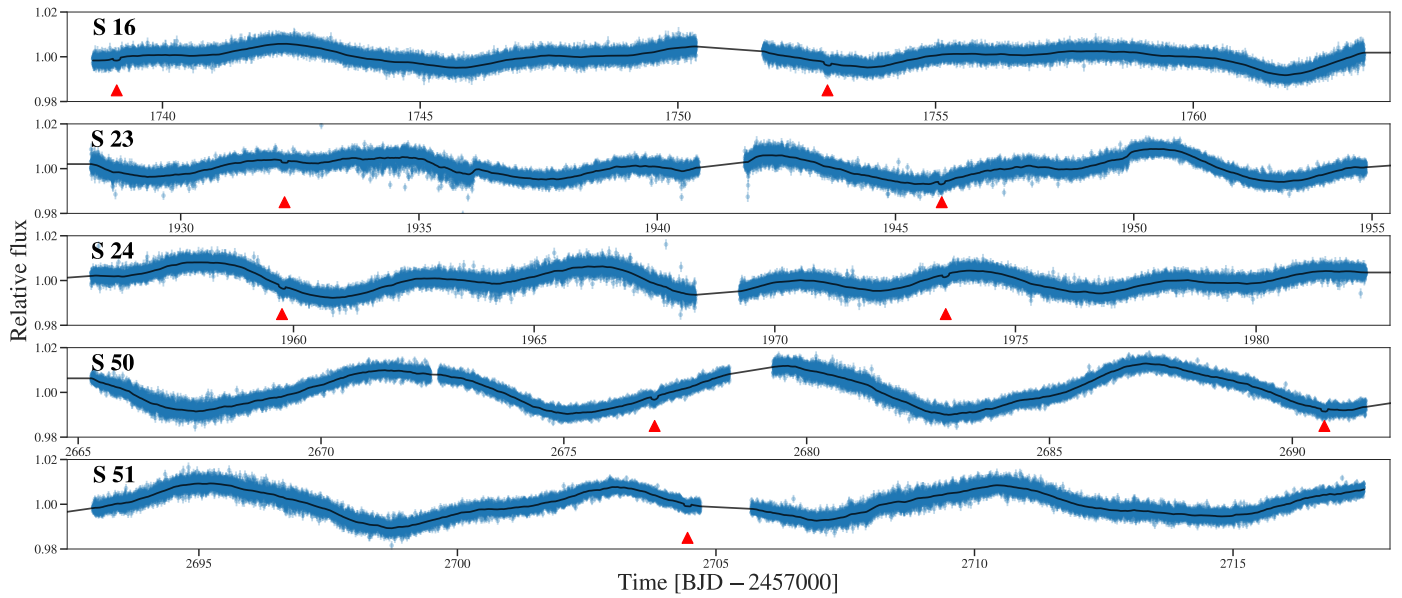


Fig. C.1: TOI-2048 two-minute cadence SAP TESS photometry from Sectors 16, 23, 24, 50, and 51 along with the transit plus GP model. The upward-pointing red triangles mark the transits for TOI-2048 b.

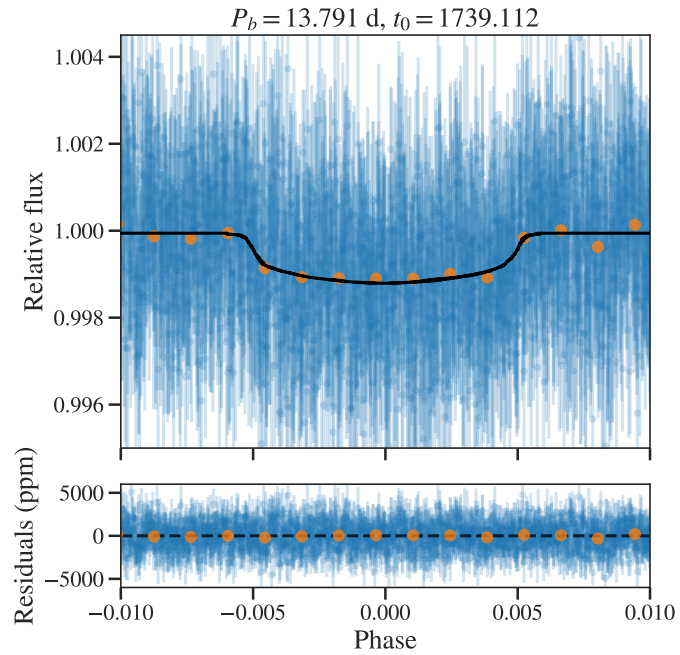


Fig. C.2: TOI-2048 TESS photometry (blue dots with error bars) phase-folded to the period P and central time of transit t_0 (shown above the panel, t_0 units are BJD - 2457 000) derived from the *juliet* fit. The black line is the best transit model for TOI-2048 b. The orange points show binned photometry for visualisation.

Appendix D: HD 63433 system extra material

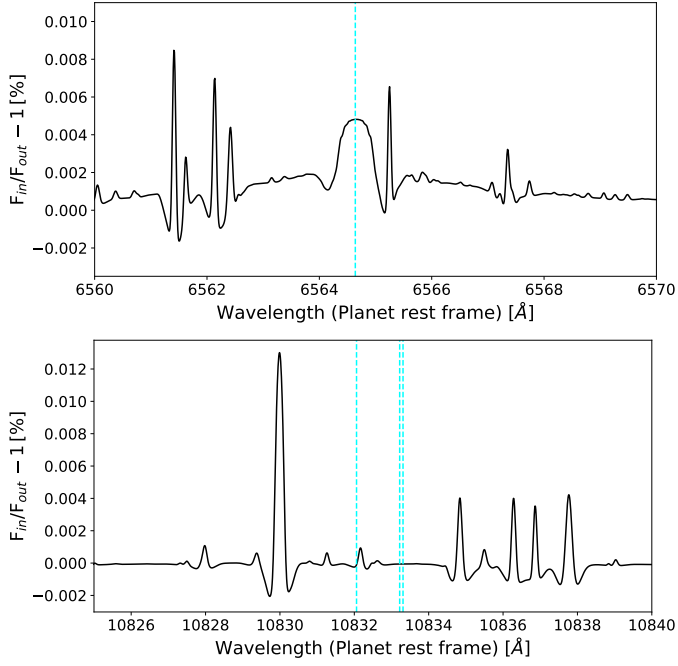


Fig. D.1: Contribution of the RM and CLV effects to the HD 63433 b transmission spectra around the $H\alpha$ (top) and $He\ I$ NIR triplet (bottom) lines. The vertical cyan lines mark the position of the lines of interest.

Table D.1: Prior and posterior distributions from the nested sampling fitting for HD 63433 b $H\alpha$ feature (see Fig. A.5). Prior label \mathcal{U} represents uniform distribution.

| Parameter | Prior | Posterior |
|-----------------------------------|-------------------------------|-------------------------|
| Absorption [%] | $\mathcal{U}(-3, 3)$ | $-1.21^{+0.22}_{-0.24}$ |
| λ_0 [\AA] | $\mathcal{U}(6560.0, 6570.0)$ | 6564.60 ± 0.03 |
| σ [\AA] | $\mathcal{U}(0.01, 0.5)$ | $0.15^{+0.04}_{-0.03}$ |
| Δv [km s^{-1}] | – | -2.0 ± 1.5 |
| FWHM [\AA] | – | $0.35^{+0.09}_{-0.07}$ |
| EW [m\AA] | – | 4.6 ± 0.8 |

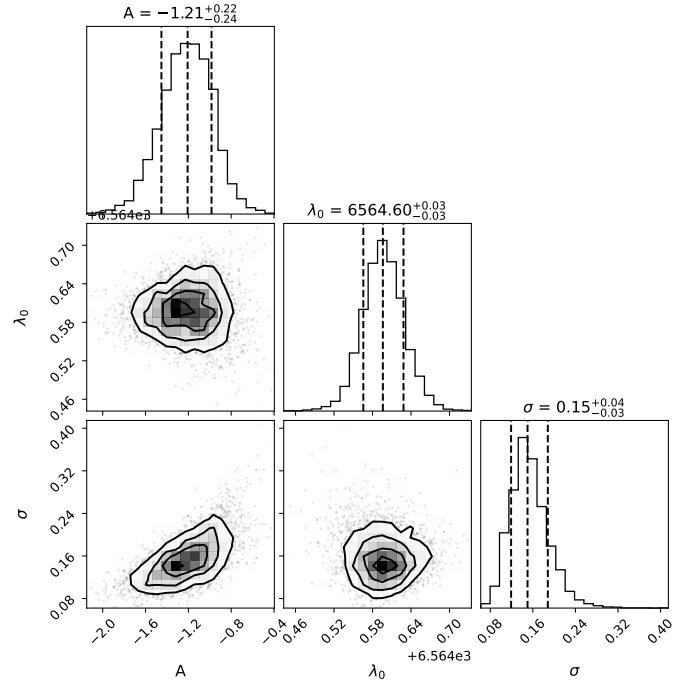


Fig. D.2: Corner plot for the nested sampling posterior distribution of HD 63433 b $H\alpha$ feature from partial transit.

Appendix E: HD 73583 system extra material

We analysed HD 73583 TESS data from Sectors 8, 34, and 61. Because our purpose for this system is not to study the young stellar activity but derive precise ephemeris, we used the *celerite* GP exponential kernel to account for the stellar variability and rotation. We adopted the stellar parameters used in Barragán et al. (2022).

The fitted parameters with their prior and posterior values, and the derived parameters for HD 73583 b and c are shown in Table E.1. The TESS data along with the best transiting and GP models is shown in Fig. E.2 and HD 73583 b and c phase folded transits are shown in Fig. E.1.

Table E.1: Prior and posterior distributions from the *juliet* fitting for HD 73583 b and c. Prior labels \mathcal{U} , \mathcal{N} , \mathcal{F} , and \mathcal{J} represents uniform, normal, fixed, and Jeffrey’s distribution, respectively.

| Parameter | Prior | Posterior |
|--|------------------------------|------------------------------------|
| P_b [d] | $\mathcal{N}(6.398, 0.01)$ | 6.3980580 (26) |
| $t_{0,b}^{(a)}$ | $\mathcal{N}(2592.55, 0.1)$ | $2592.56287^{+0.00025}_{-0.00022}$ |
| ecc_b | $\mathcal{F}(0)$ | – |
| ω_b (deg) | $\mathcal{F}(90)$ | – |
| $r_{1,b}$ | $\mathcal{U}(0, 1)$ | $0.718^{+0.009}_{-0.012}$ |
| $r_{2,b}$ | $\mathcal{U}(0, 1)$ | 0.0387 ± 0.0004 |
| P_c [d] | $\mathcal{N}(18.8797, 0.01)$ | 18.879300 (48) |
| $t_{0,c}^{(a)}$ | $\mathcal{N}(2949.6, 0.1)$ | $2949.58243^{+0.00077}_{-0.00094}$ |
| ecc_c | $\mathcal{F}(0)$ | – |
| ω_c (deg) | $\mathcal{F}(90)$ | – |
| $r_{1,c}$ | $\mathcal{U}(0, 1)$ | $0.353^{+0.015}_{-0.012}$ |
| $r_{2,c}$ | $\mathcal{U}(0, 1)$ | 0.03301 ± 0.00077 |
| ρ_\star [kg m^{-3}] | $\mathcal{N}(3500.0, 500.0)$ | 3750^{+160}_{-110} |
| μ_{TESS} (ppm) | $\mathcal{N}(0.0, 0.1)$ | $2.0^{+1.6}_{-1.4} \times 10^3$ |
| σ_{TESS} (ppm) | $\mathcal{J}(10^{-6}, 10^6)$ | 436.3 ± 2.2 |
| $q_{1,TESS}$ | $\mathcal{U}(0, 1)$ | $0.12^{+0.06}_{-0.04}$ |
| $q_{2,TESS}$ | $\mathcal{U}(0, 1)$ | $0.54^{+0.24}_{-0.27}$ |
| GP_σ (ppm) | $\mathcal{J}(10^{-6}, 10^6)$ | $8.5^{+1.2}_{-0.9} \times 10^3$ |
| GP_ρ [d] | $\mathcal{J}(10^{-3}, 10^3)$ | $2.04^{+0.20}_{-0.17}$ |
| <i>Derived planetary parameters for HD 73583 b</i> | | |
| $p_b = R_p/R_\star$ | | 0.0387 ± 0.0004 |
| $b_b = (a_p/R_\star) \cos i_p$ | | $0.577^{+0.013}_{-0.018}$ |
| $i_{p,b}$ (deg) | | $88.35^{+0.07}_{-0.05}$ |
| $T_{14,b}$ [h] | | $2.100^{+0.015}_{-0.013}$ |
| $T_{12,b}$ [min] | | $6.93^{+0.17}_{-0.22}$ |
| $R_{p,b}$ [R_\oplus] | | 2.78 ± 0.09 |
| $a_{p,b}$ [AU] | | 0.0618 ± 0.0020 |
| $T_{\text{eq},b}$ [K] ^(b) | | 710 ± 18 |
| <i>Derived planetary parameters for HD 73583 c</i> | | |
| $p_c = R_p/R_\star$ | | 0.0330 ± 0.0008 |
| $b_c = (a_p/R_\star) \cos i_p$ | | $0.030^{+0.022}_{-0.017}$ |
| $i_{p,c}$ (deg) | | 89.96 ± 0.03 |
| $T_{14,c}$ [h] | | $3.60^{+0.03}_{-0.05}$ |
| $T_{12,c}$ [min] | | 6.90 ± 0.20 |
| $R_{p,c}$ [R_\oplus] | | 2.38 ± 0.09 |
| $a_{p,c}$ [AU] | | 0.1270 ± 0.0040 |
| $T_{\text{eq},c}$ [K] ^(b) | | 495 ± 12 |

Notes. ^(a) Central time of transit (t_0) units are BJD – 2 457 000. ^(b) Equilibrium temperatures were calculated assuming zero Bond albedo.

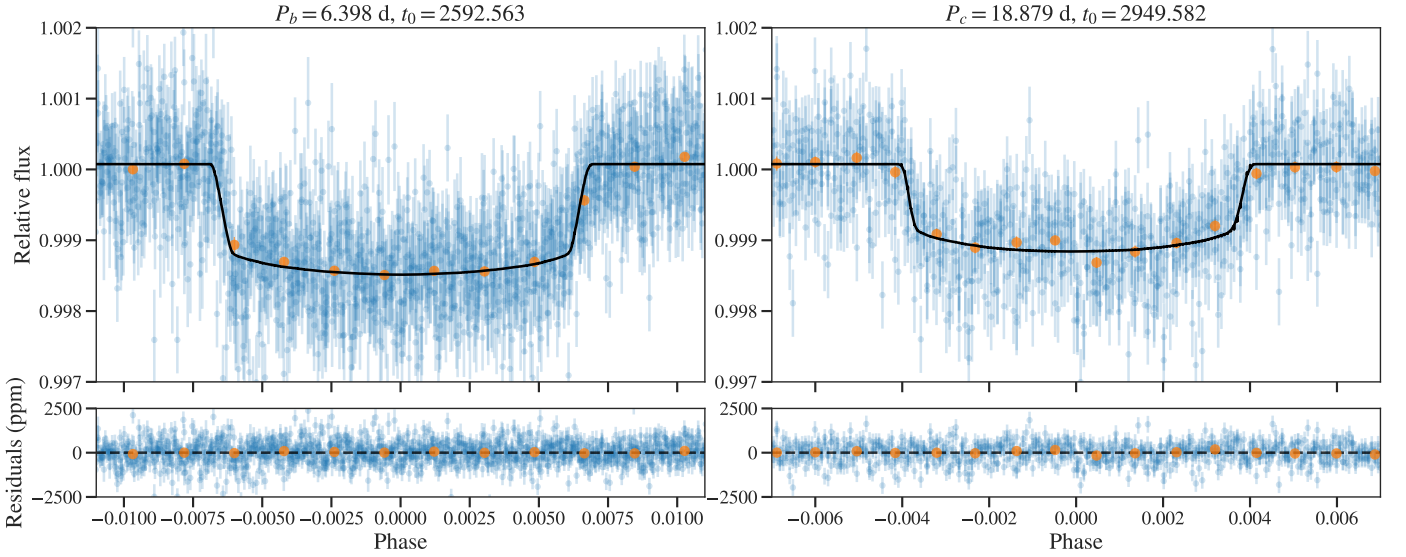


Fig. E.1: HD 73583 TESS photometry (blue dots with error bars) phase-folded to the period P and central time of transit t_0 (shown above each panel, t_0 units are BJD $- 2\,457\,000$) derived for planet b (left), and c (right) from the `juliet` fit. The black line is the best transit model for each planet. The orange points show binned photometry for visualisation.

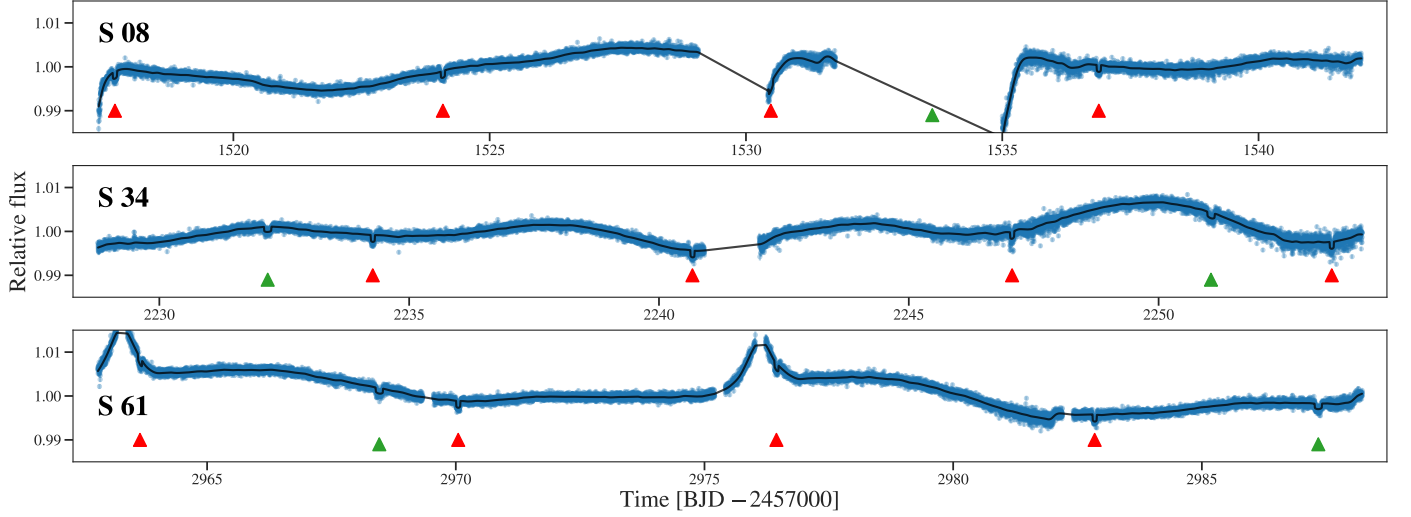


Fig. E.2: HD 73583 2 min cadence TESS photometry from Sectors 8, 34, and 61 along with the transit plus GP model. The upward-pointing red and green triangles mark the transit times for HD 73583 b and c, respectively.

Table E.2: Prior and posterior distributions from the nested sampling fitting for HD 73583 b $H\alpha$ feature (see Fig. A.7). Prior label \mathcal{U} represents uniform distribution.

| Parameter | Prior | Posterior |
|-----------------------------------|---------------------------|---------------------------|
| Absorption [%] | $\mathcal{U}(-3, 3)$ | -0.46 ± 0.16 |
| λ_0 [\AA] | $\mathcal{U}(6562, 6566)$ | $6564.51^{+0.07}_{-0.06}$ |
| σ [\AA] | $\mathcal{U}(0, 1)$ | $0.18^{+0.11}_{-0.06}$ |
| Δv [km s^{-1}] | – | $-6.1^{+3.2}_{-2.5}$ |
| FWHM [\AA] | – | $0.43^{+0.26}_{-0.14}$ |
| EW [m\AA] | – | $2.1^{+0.7}_{-0.6}$ |

Table E.3: Prior and posterior distributions from the nested sampling fitting for HD 73583 c $H\alpha$ feature (see Fig. A.8). Prior label \mathcal{U} represents uniform distribution.

| Parameter | Prior | Posterior |
|-----------------------------------|---------------------------|---------------------------|
| Absorption [%] | $\mathcal{U}(-3, 3)$ | $-0.54^{+0.13}_{-0.14}$ |
| λ_0 [\AA] | $\mathcal{U}(6562, 6566)$ | $6564.65^{+0.07}_{-0.08}$ |
| σ [\AA] | $\mathcal{U}(0.12, 1)$ | $0.30^{+0.10}_{-0.09}$ |
| Δv [km s^{-1}] | – | 0.6 ± 3.4 |
| FWHM [\AA] | – | $0.68^{+0.22}_{-0.21}$ |
| EW [m\AA] | – | $3.8^{+1.0}_{-0.9}$ |

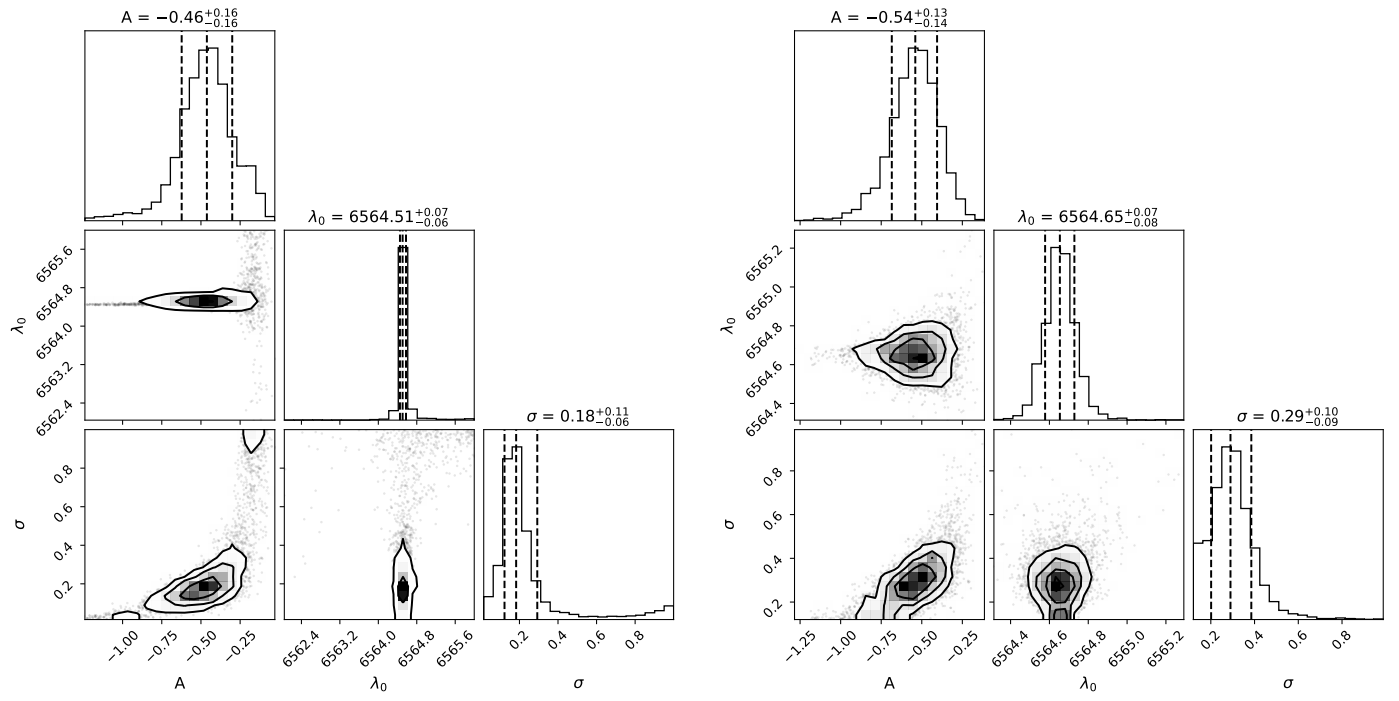


Fig. E.3: Corner plot for the nested sampling posterior distribution of HD 73583 b (left) and HD 73583 c (right) $H\alpha$ features.

Appendix F: K2-77 b planetary parameters

We analysed the K2-77 b TESS data from Sectors 5, 42, 43, and 44. Because we did not see a clear rotation modulation in the light curves, we used the *celerite* GP exponential kernel to account for the stellar variability. We adopted the stellar parameters used in [Gaidos et al. \(2017\)](#).

The fitted parameters with their prior and posterior values, and the derived parameters for K2-77 b are shown in Table F.1. The TESS data along with the best transiting and GP models is shown in Fig. F.2 and K2-77 b phase folded transit is shown in Fig. F.1.

As we did in App. C, we forecasted K2-77 b mass and we computed the estimated K_\star using Eq. C.1. We predicted a planetary mass of $\sim 9 \pm 2 M_\oplus$, and a semi-amplitude K_\star of $\sim 3.4 \pm 0.8 \text{ m s}^{-1}$. [Gaidos et al. \(2017\)](#) only reported an upper limit to K2-77 b's mass of $1.9 M_J$.

Table F.1: Prior and posterior distributions from the *juliet* fitting for K2-77 b. Prior labels \mathcal{U} , \mathcal{N} , \mathcal{F} , and \mathcal{J} represents uniform, normal, fixed, and Jeffrey's distribution, respectively.

| Parameter | Prior | Posterior |
|-------------------------------------|------------------------------|----------------------------------|
| P [d] | $\mathcal{N}(8.2, 0.01)$ | 8.200139 (60) |
| t_0 ^(a) | $\mathcal{N}(2522.6, 0.1)$ | $2522.6338^{+0.0037}_{-0.0033}$ |
| ecc | $\mathcal{F}(0)$ | – |
| ω (deg) | $\mathcal{F}(90)$ | – |
| r_1 | $\mathcal{U}(0, 1)$ | $0.66^{+0.09}_{-0.17}$ |
| r_2 | $\mathcal{U}(0, 1)$ | $0.0309^{+0.0022}_{-0.0025}$ |
| ρ_\star [kg m^{-3}] | $\mathcal{N}(2577.0, 500.0)$ | 2700^{+450}_{-460} |
| μ_{TESS} (ppm) | $\mathcal{N}(0.0, 0.1)$ | 300^{+810}_{-770} |
| σ_{TESS} (ppm) | $\mathcal{J}(10^{-6}, 10^6)$ | $4.5^{+1700}_{-4.5} \times 10^3$ |
| $q_{1,TESS}$ | $\mathcal{U}(0, 1)$ | $0.55^{+0.30}_{-0.34}$ |
| $q_{2,TESS}$ | $\mathcal{U}(0, 1)$ | $0.52^{+0.31}_{-0.33}$ |
| GP_σ (ppm) | $\mathcal{J}(10^{-6}, 10^6)$ | $4.2^{+0.5}_{-0.4} \times 10^3$ |
| GP_ρ [d] | $\mathcal{J}(10^{-3}, 10^3)$ | $1.65^{+0.17}_{-0.15}$ |
| <i>Derived planetary parameters</i> | | |
| $p = R_p/R_\star$ | | $0.0309^{+0.0022}_{-0.0025}$ |
| $b = (a_p/R_\star) \cos i_p$ | | $0.50^{+0.13}_{-0.25}$ |
| i_p (deg) | | $88.7^{+0.7}_{-0.4}$ |
| T_{14} [h] | | 2.68 ± 0.22 |
| T_{12} [min] | | $6.3^{+1.5}_{-1.1}$ |
| R_p [R_\oplus] | | 2.55 ± 0.20 |
| a_p [AU] | | $0.0751^{+0.0045}_{-0.0050}$ |
| T_{eq} [K] ^(b) | | 760^{+25}_{-21} |

Notes. ^(a) Central time of transit (t_0) units are BJD – 2 457 000. ^(b) Equilibrium temperatures were calculated assuming zero Bond albedo.

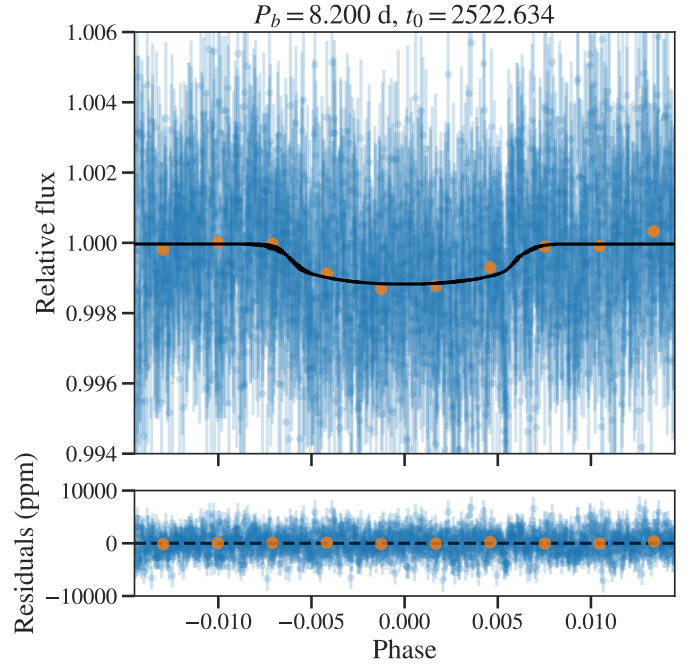


Fig. F.1: K2-77 TESS photometry (blue dots with error bars) phase-folded to the period P and central time of transit t_0 (shown above the panel, t_0 units are BJD – 2 457 000) derived from the *juliet* fit. The black line is the best transit model for K2-77 b. The orange points show binned photometry for visualisation.

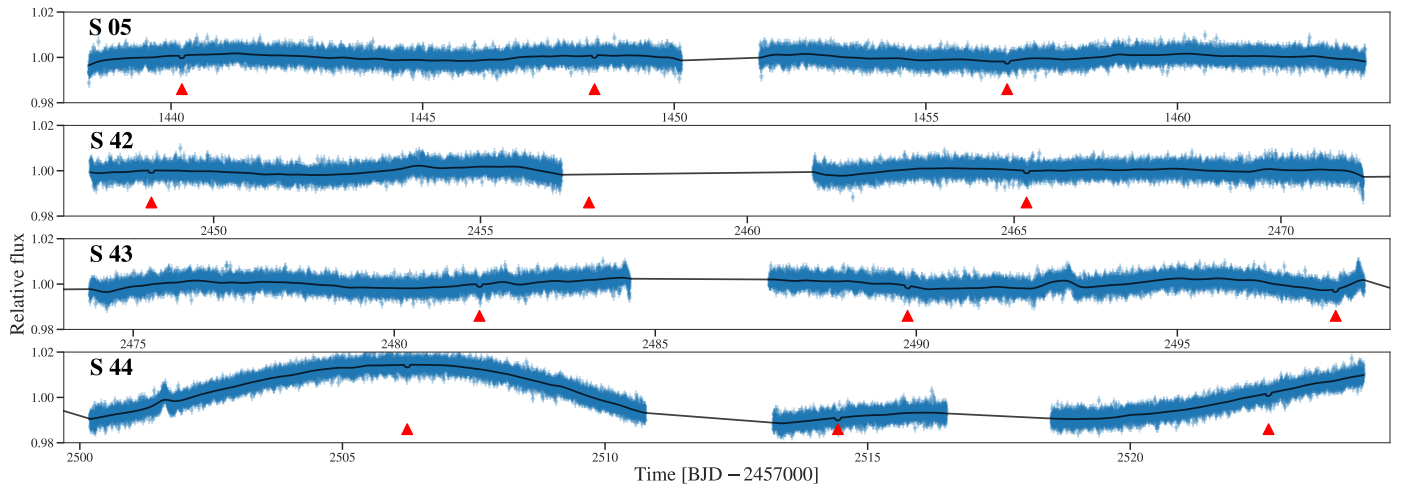


Fig. F.2: K2-77 2 min cadence TESS photometry from Sectors 5, 42, 43, and 44 along with the transit plus GP model. The upward-pointing red triangles mark the transits for K2-77 b.

Appendix G: TOI-1807 b extra material

We analysed TOI-1807 TESS data from Sectors 22, 23, and 49. Because our purpose is not to model the young stellar activity, but derive precise ephemerides, we used the unspecific celerite GP exponential kernel to account for the stellar variability and rotation. We adopted the stellar parameters used in Nardiello et al. (2022) for a proper comparison.

The fitted parameters with their prior and posterior values, and the derived parameters for TOI-1807 b are shown in Table G.1. The TESS data along with the best transiting and GP models is shown in Fig. G.2 and TOI-1807 b phase folded transit is shown in Fig. G.1.

Table G.1: Prior and posterior distributions from the *juliet* fitting for TOI-1807 b. Prior labels \mathcal{U} , \mathcal{N} , \mathcal{F} , and \mathcal{J} represents uniform, normal, fixed, and Jeffrey’s distribution, respectively.

| Parameter | Prior | Posterior |
|-------------------------------------|-------------------------------|--|
| P [d] | $\mathcal{N}(0.54929, 0.001)$ | 0.54937084 (65) |
| t_0 ^(a) | $\mathcal{N}(2664.07, 0.1)$ | 2664.06930 ^{+0.00073} _{-0.00075} |
| ecc | $\mathcal{F}(0)$ | – |
| ω (deg) | $\mathcal{F}(90)$ | – |
| r_1 | $\mathcal{U}(0, 1)$ | 0.70 ^{+0.05} _{-0.06} |
| r_2 | $\mathcal{U}(0, 1)$ | 0.01776 ^{+0.00045} _{-0.00052} |
| ρ_\star [kg m ⁻³] | $\mathcal{N}(3300.0, 600.0)$ | 3430 ⁺⁵³⁰ ₋₅₅₀ |
| μ_{TESS} (ppm) | $\mathcal{N}(0.0, 0.1)$ | -0.6 ^{+2.0} _{-2.0} × 10 ³ |
| σ_{TESS} (ppm) | $\mathcal{J}(10^{-6}, 10^6)$ | 500 ^{+4.3} _{-4.1} |
| $q_{1,TESS}$ | $\mathcal{U}(0, 1)$ | 0.15 ^{+0.24} _{-0.11} |
| $q_{2,TESS}$ | $\mathcal{U}(0, 1)$ | 0.26 ^{+0.36} _{-0.20} |
| GP_σ (ppm) | $\mathcal{J}(10^{-6}, 10^6)$ | 8.7 ^{+1.5} _{-1.1} × 10 ³ |
| GP_ρ [d] | $\mathcal{J}(10^{-3}, 10^3)$ | 2.30 ^{+0.28} _{-0.25} |
| <i>Derived planetary parameters</i> | | |
| $p = R_p/R_\star$ | | 0.01776 ^{+0.00045} _{-0.00052} |
| $b = (a_p/R_\star) \cos i_p$ | | 0.550 ^{+0.077} _{-0.100} |
| i_p (deg) | | 81.7 ± 0.18 |
| T_{14} [h] | | 0.970 ± 0.022 |
| T_{12} [min] | | 1.45 ^{+0.25} _{-0.18} |
| R_p [R_\oplus] | | 1.33 ± 0.08 |
| a_p [AU] | | 0.0121 ± 0.0009 |
| T_{eq} [K] ^(b) | | 1720 ⁺⁵⁵ ₋₅₀ |

Notes. ^(a) Central time of transit (t_0) units are BJD – 2 457 000. ^(b) Equilibrium temperatures were calculated assuming zero Bond albedo.

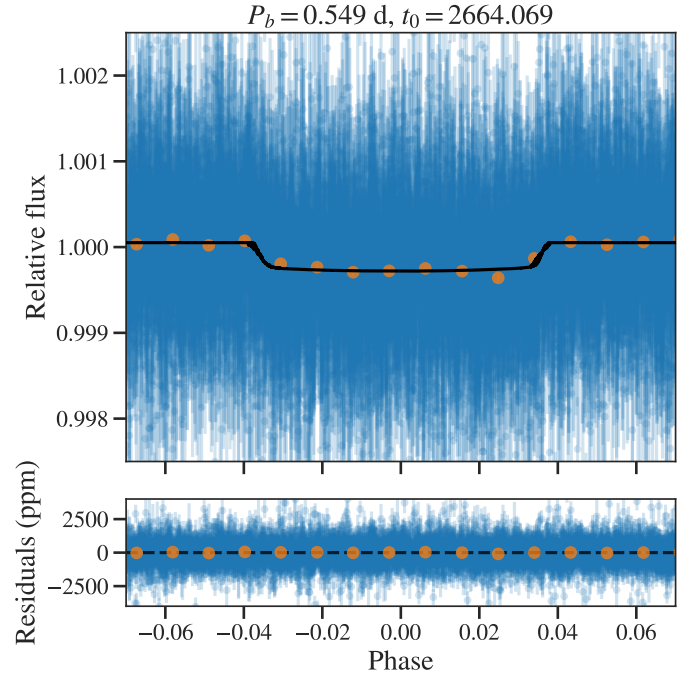


Fig. G.1: TOI-1807 TESS photometry (blue dots with error bars) phase-folded to the period P and central time of transit t_0 (shown above the panel, t_0 units are BJD – 2 457 000) derived from the *juliet* fit. The black line is the best transit model for TOI-1807 b. The orange points show binned photometry for visualisation.

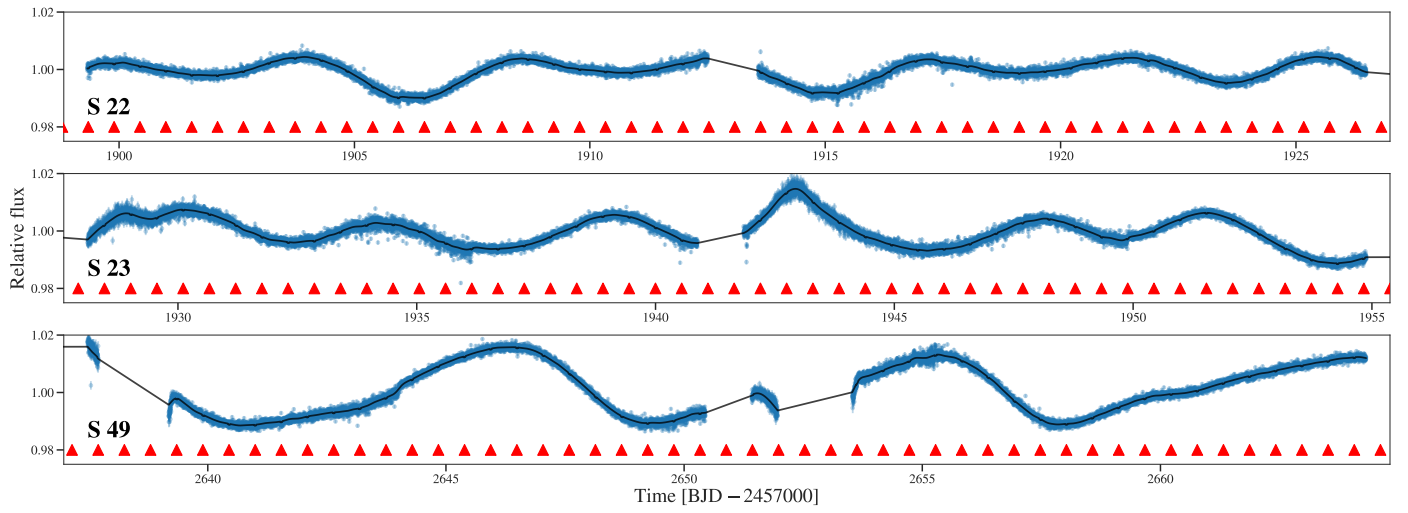


Fig. G.2: TOI-1807 2 min cadence TESS photometry from Sectors 22, 23, and 49 along with the transit plus GP model. The upward-pointing red triangles mark the transit times for the ultra-short period TOI-1807 b.

Appendix H: TOI-1136 d extra material

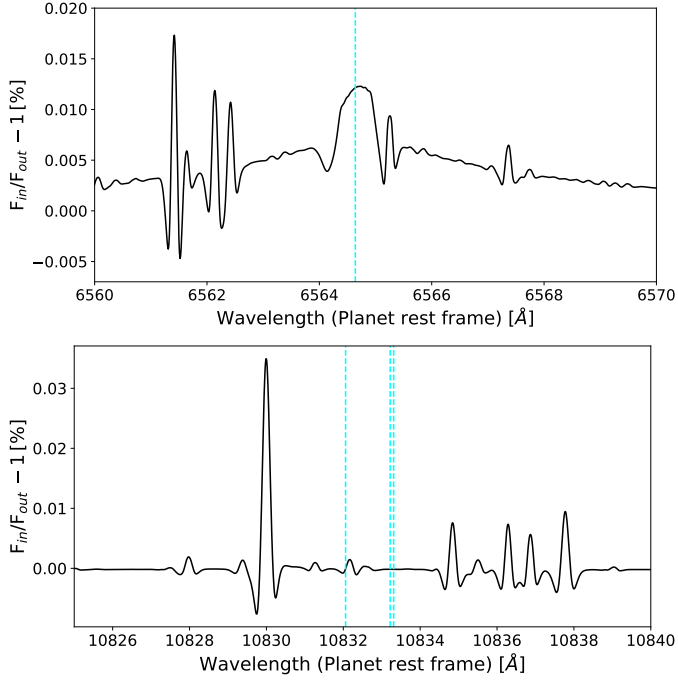


Fig. H.1: Contribution of the RM and CLV effects to the TOI-1136 d transmission spectra around the H α (top) and He I NIR triplet (bottom) lines. The vertical cyan lines mark the position of the lines of interest.

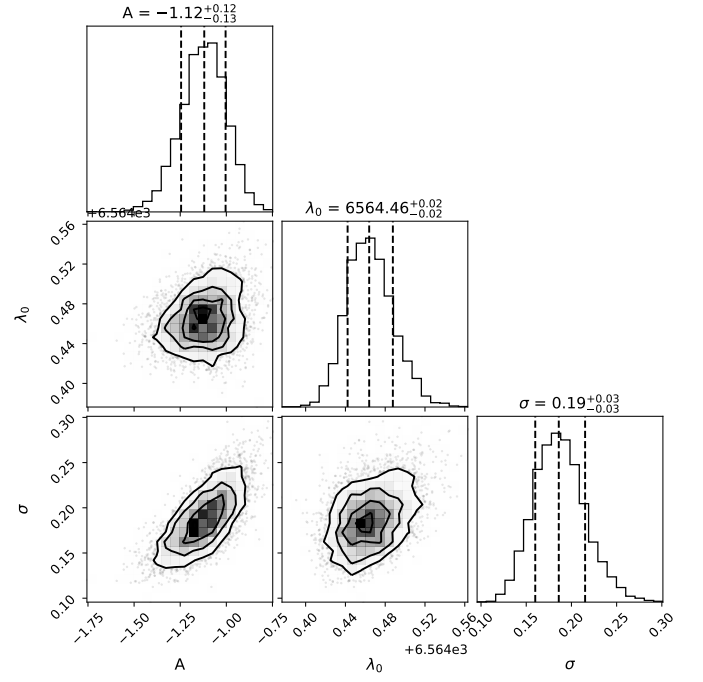


Fig. H.2: Corner plot for the nested sampling posterior distribution of TOI-1136 d H α feature.

Table H.1: Prior and posterior distributions from the nested sampling fitting for TOI-1136 d H α feature (see Fig. 2). Prior label \mathcal{U} represents uniform distribution.

| Parameter | Prior | Posterior |
|----------------------------|---------------------------|------------------------------|
| Absorption [%] | $\mathcal{U}(-3, 3)$ | $-1.12^{+0.12}_{-0.13}$ |
| λ_0 [Å] | $\mathcal{U}(6562, 6566)$ | $6564.464^{+0.024}_{-0.022}$ |
| σ [Å] | $\mathcal{U}(0, 1)$ | $0.186^{+0.030}_{-0.025}$ |
| Δv [km s $^{-1}$] | – | -8.0 ± 1.0 |
| FWHM [Å] | – | $0.45^{+0.07}_{-0.06}$ |
| EW [mÅ] | – | $5.20^{+0.57}_{-0.53}$ |

Appendix I: TOI-1268 b extra material

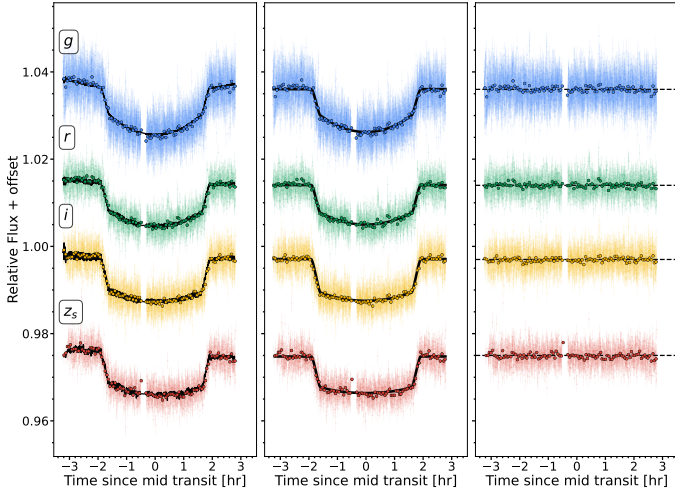


Fig. I.1: MuSCAT2 ground-based transit observation of TOI-1268 b. Raw light curve (left panel), detrended light curve (centre panel), and residuals (right panel) for the Sloan g (blue), r (green), i (yellow), z_s (red) filters. The points show the individual observations, the circles represent binned data points, and the best-fit model is shown by the black line.

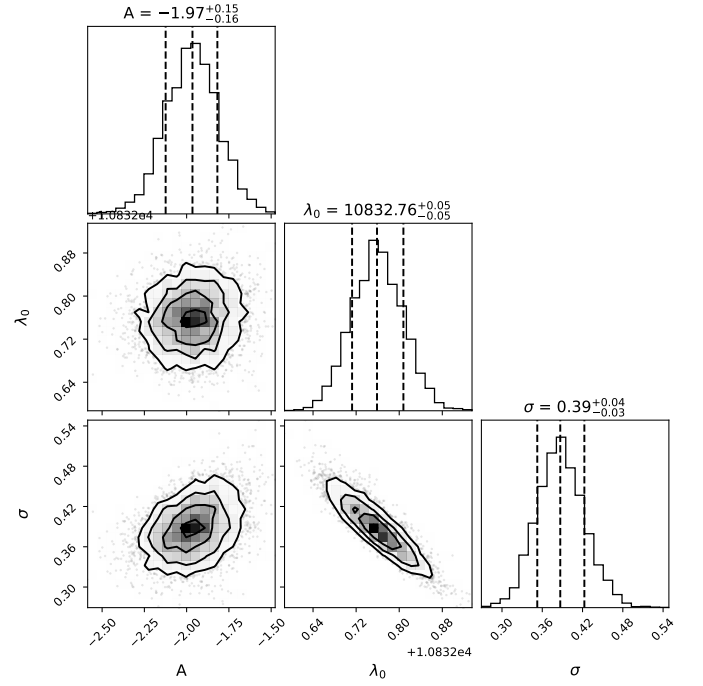


Fig. I.2: Corner plot for the nested sampling posterior distribution of TOI-1268 b He I signal.

Table I.1: Prior and posterior distributions from the nested sampling fitting for TOI-1268 b He I signal (see Fig. 4). Prior label \mathcal{U} represents uniform distribution.

| Parameter | Prior | Posterior |
|----------------------------------|-----------------------------|--------------------------|
| Absorption [%] | $\mathcal{U}(-3, 3)$ | $-2.00^{+0.15}_{-0.16}$ |
| λ_0 [Å] | $\mathcal{U}(10831, 10834)$ | 10832.76 ± 0.050 |
| σ [Å] | $\mathcal{U}(0, 1.5)$ | $0.39^{+0.036}_{-0.034}$ |
| Δv [km s ⁻¹] | – | -12.8 ± 1.3 |
| FWHM [Å] | – | $0.91^{+0.9}_{-0.08}$ |
| EW [mÅ] | – | $19.1^{+1.8}_{-1.9}$ |

Appendix J: TOI-2076 b extra material

Table J.1: Prior and posterior distributions from the `juliet` fitting for TOI-2076 b data from LCO (see Fig. J.1). Prior labels \mathcal{U} , \mathcal{N} , \mathcal{F} , and \mathcal{J} represents uniform, normal, fixed, and Jeffrey’s distribution, respectively.

| Parameter | Prior | Posterior |
|-------------------------------------|------------------------------------|---------------------------------|
| P [d] | $\mathcal{N}(10.355183, 0.000065)$ | 10.355184 (58) |
| $t_0^{(a)}$ | $\mathcal{U}(3079.47, 3079.62)$ | $3079.5495^{+0.0061}_{-0.0045}$ |
| ecc | $\mathcal{F}(0)$ | – |
| ω (deg) | $\mathcal{F}(90)$ | – |
| $b = (a_p/R_\star) \cos i_p$ | $\mathcal{N}(0.149, 0.089)$ | $0.158^{+0.071}_{-0.074}$ |
| $p = R_p/R_\star$ | $\mathcal{N}(0.02998, 0.00035)$ | 0.03003 (30) |
| ρ_\star [kg m^{-3}] | $\mathcal{N}(2544, 120)$ | 2535 ± 100 |
| μ_{LCO} (ppm) | $\mathcal{N}(0.0, 0.1)$ | $-0.6^{+11}_{-25} \times 10^3$ |
| σ_{LCO} (ppm) | $\mathcal{J}(10^{-6}, 10^6)$ | 1175^{+76}_{-72} |
| $q_{1,LCO}$ | $\mathcal{U}(0, 1)$ | $0.57^{+0.30}_{-0.35}$ |
| GP_σ (ppm) | $\mathcal{J}(10^{-6}, 10^6)$ | $13^{+80}_{-12} \times 10^3$ |
| GP_ρ [d] | $\mathcal{J}(10^{-3}, 10^3)$ | $2.5^{+25}_{-2.3}$ |
| <i>Derived planetary parameters</i> | | |
| i_p (deg) | | 89.63 ± 0.18 |
| T_{14} [h] | | 3.31 ± 0.06 |
| R_p [R_\oplus] | | 2.523 ± 0.032 |

Notes. ^(a) Central time of transit (t_0) units are BJD – 2 457 000. ^(b) Equilibrium temperatures were calculated assuming zero Bond albedo.

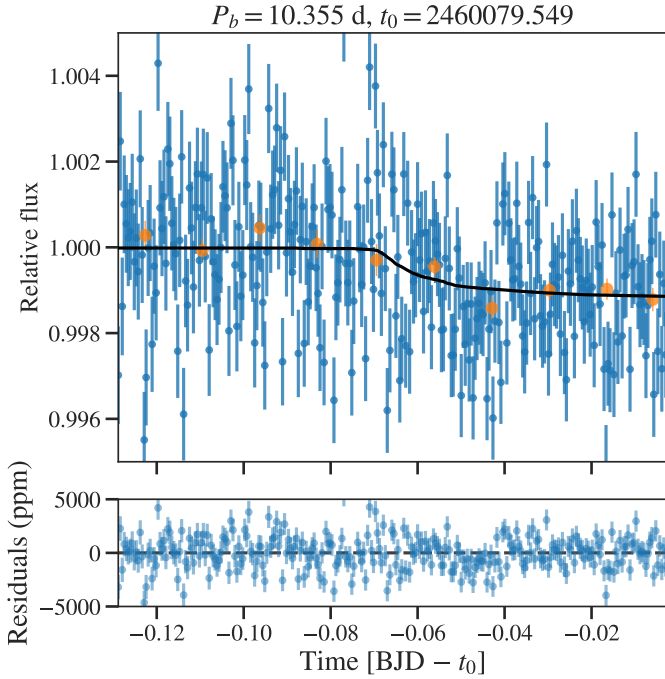


Fig. J.1: TOI-2076 LCO photometric data (blue dots with error bars). The period P and central time of transit t_0 derived from the `juliet` fit are shown above the panel. The black line is the best transit model for TOI-2076 b. The orange points show binned photometry for visualisation. The GP contribution was removed from the data.

Appendix K: TOI-1683 b extra material

Table K.1: Prior and posterior distributions from the *juliet* fitting for TOI-1683 b. Prior labels \mathcal{U} , \mathcal{N} , \mathcal{F} , and \mathcal{J} represents uniform, normal, fixed, and Jeffrey’s distribution, respectively.

| Parameter | Prior | Posterior |
|-------------------------------------|------------------------------|------------------------------------|
| P [d] | $\mathcal{N}(3.057, 0.001)$ | $3.057541^{+0.000014}_{-0.000010}$ |
| t_0 ^(a) | $\mathcal{N}(2522.7, 0.1)$ | $2522.7001^{+0.0012}_{-0.0010}$ |
| ecc | $\mathcal{F}(0)$ | – |
| ω (deg) | $\mathcal{F}(90)$ | – |
| r_1 | $\mathcal{U}(0, 1)$ | $0.799^{+0.030}_{-0.040}$ |
| r_2 | $\mathcal{U}(0, 1)$ | 0.0319 ± 0.0014 |
| ρ_\star [kg m ⁻³] | $\mathcal{N}(3800.0, 600.0)$ | 3900^{+570}_{-580} |
| μ_{TESS} (ppm) | $\mathcal{N}(0.0, 0.1)$ | 510 ± 3900 |
| σ_{TESS} (ppm) | $\mathcal{J}(10^{-6}, 10^6)$ | 334^{+11}_{-12} |
| $q_{1,TESS}$ | $\mathcal{U}(0, 1)$ | 0.62 ± 0.25 |
| $q_{2,TESS}$ | $\mathcal{U}(0, 1)$ | 0.56^{+28}_{-34} |
| GP _B (ppm) | $\mathcal{J}(10^{-6}, 10^6)$ | 62^{+60}_{-25} |
| GP _L [d] | $\mathcal{J}(10^{-3}, 10^3)$ | 100^{+100}_{-42} |
| GP _C (ppm) | $\mathcal{J}(10^{-6}, 10^6)$ | 500^{+33000}_{-500} |
| GP _{rot} [d] | $\mathcal{U}(1, 50)$ | 20.0 ± 1.0 |
| <i>Derived planetary parameters</i> | | |
| $p = R_p/R_\star$ | | 0.0319 ± 0.0014 |
| $b = (a_p/R_\star) \cos i_p$ | | $0.70^{+0.05}_{-0.06}$ |
| i_p (deg) | | 86.80 ± 0.38 |
| T_{14} [h] | | $1.43^{+0.07}_{-0.05}$ |
| T_{12} [min] | | $5.0^{+0.8}_{-0.6}$ |
| R_p [R_\oplus] | | 2.21 ± 0.13 |
| a_p [AU] | | 0.0368 ± 0.0023 |
| T_{eq} [K] ^(b) | | 910 ± 30 |

Notes. ^(a) Central time of transit (t_0) units are BJD – 2 457 000. ^(b) Equilibrium temperatures were calculated assuming zero Bond albedo.

We analysed TOI-1683 TESS data from Sectors 19, 43, and 44. Because our purpose is to model the stellar rotation, we used the *celerite* GP quasi-periodic kernel. We adopted the stellar parameters used in [Zhang et al. \(2023b\)](#) for a proper comparison. The fitted parameters with their prior and posterior values, and the derived parameters for the planet candidate TOI-1683 b are shown in Table K.1. The TESS data along with the best transiting and GP models is shown in Fig. K.2 and TOI-1683 b phase folded transit is shown in Fig. K.1.

We computed the GLS periodogram ([Zechmeister & Kürster 2009](#), generalised Lomb-Scargle) in the light curve of the three available TESS Sectors. We derived a stellar rotation period of 22.5 ± 5.2 days, which is consistent with the GP_{rot} value from the photometric fit (GP_{rot} 20 ± 1 d). We estimated TOI-1683’s age using the gyrochronology methods from [Mamajek & Hillenbrand \(2008, Eq. 12, 13, 14 and parameters from Table 10\)](#), [Schlaufman \(2010, Eq. 1\)](#), and [Bouma et al. \(2023, python package gyro-interp⁸\)](#), and the derived ages are 1450^{+700}_{-550} Myr, 2300^{+1300}_{-900} Myr, and 2600 ± 1200 Myr, respectively. All the three methods are consistent with an age older than 1 Gyr. Figure K.3

⁸ <https://gyro-interp.readthedocs.io/en/latest/index.html>

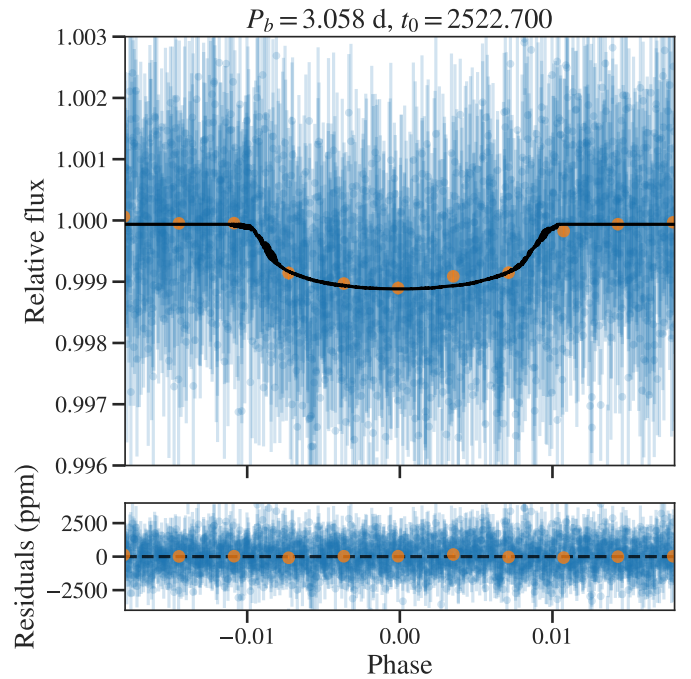


Fig. K.1: TOI-1683 TESS photometry (blue dots with error bars) phase-folded to the period P and central time of transit t_0 (shown above the panel, t_0 units are BJD – 2 457 000) derived from the *juliet* fit. The black line is the best transit model for TOI-1683 b. The orange points show binned photometry for visualisation.

shows the distribution of rotation periods as a function of the $G - J$ colour for various young clusters. From this qualitative analysis, it is evident that TOI-1683 appears to be older than the NGC 6811 cluster (which has an age ~ 1 Gyr), and it is positioned above the sequence of NGC 6774 (~ 2.5 Gyr).

On the other hand, the presence of atmospheric absorption lines, such as Li I at 6709.61 \AA , can serve as a valuable age indicator for the stars. We searched for the presence of Li I in the co-added spectrum generated by the *serval* from the CARMENES spectra. However, no clear Li I feature was detected in the spectrum. Therefore, we set an upper limit for the Li I equivalent width of 1 m\AA at 3σ . As Figure K.4 shows, this upper limit suggests that the star is older than the Hyades or Praesepe clusters, which have ages between 590–650 Myr. Lastly, to investigate the kinematic properties of TOI-1683 and to determine if it shares any characteristics with known clusters, moving groups, or associations, we calculated the UVW galactocentric space velocities using the astrometry and systemic velocity data from *Gaia*. Figure K.5 places TOI-1683 outside of any shown young moving group or cluster. Additionally, we conducted a search in the literature of cluster catalogs, and TOI-1683 was not found to be associated with any of these known stellar groups. These results suggest that it is not part of any well-established stellar association or cluster. Based on our analysis, we adopt an age older than 1 Gyr for TOI-1683 and, therefore, it is not a young object in terms of planet formation and evolution.

The age resulting of combining the three gyrochronology methods is 2000^{+1300}_{-900} Myr, which is the age used in this work. However, [Zhang et al. \(2023b\)](#) claim that TOI-1683 is a young star (< 1 Gyr) with an age of 500 ± 150 Myr based on its gyrochronology analysis. The main difference with our analyses

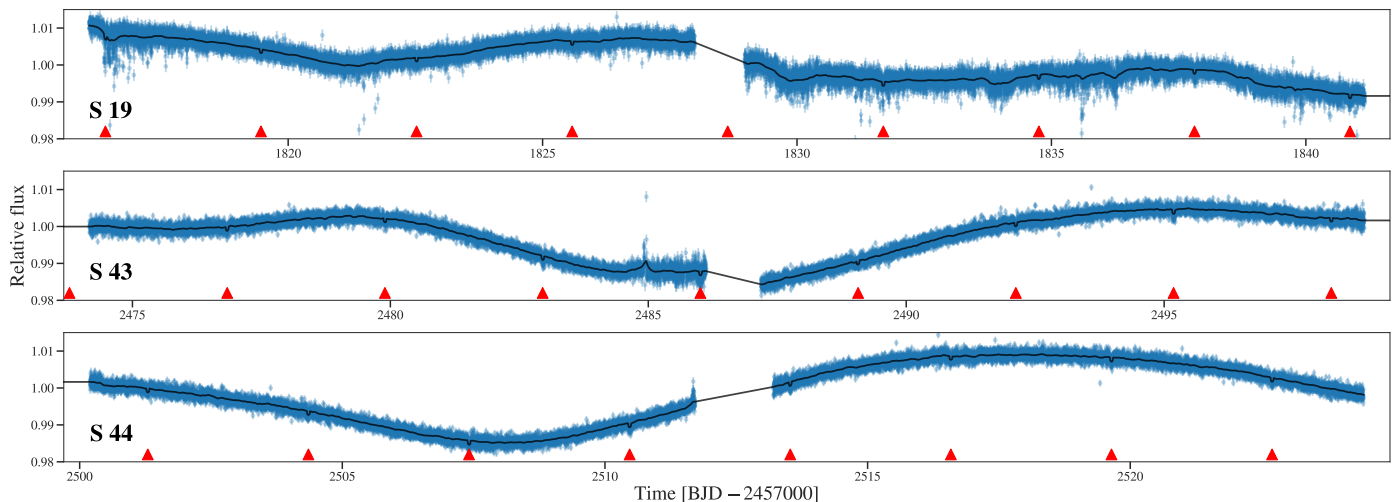


Fig. K.2: TOI-1683 2 min cadence TESS photometry from Sectors 19, 43, and 44 along with the transit plus GP model. The upward-pointing red triangles mark the transit times for the TOI-1683 b.

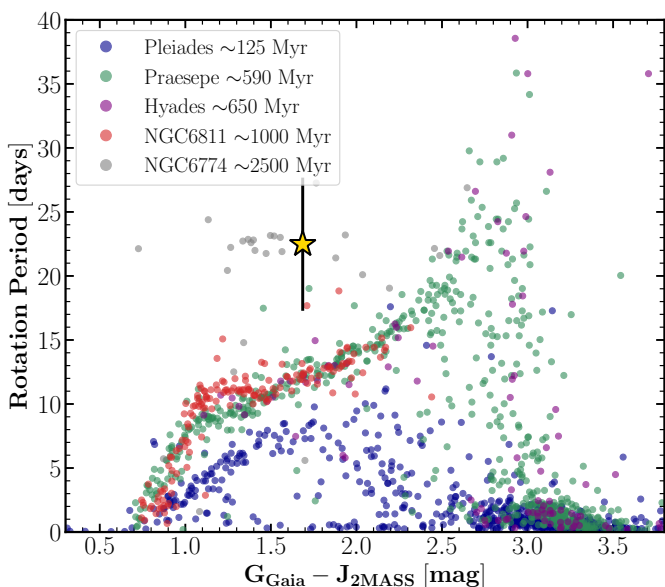


Fig. K.3: Rotation period distribution as a function of colour $G-J$ for the Pleiades (~ 125 Myr; [Rebull et al. 2016](#)), Praesepe (~ 590 Myr; [Douglas et al. 2017](#)), Hyades (~ 650 Myr; [Douglas et al. 2019](#)), NGC 6811 (~ 1000 Myr; [Curtis et al. 2019](#)), and NGC 6774 (~ 2500 Myr; [Gruner & Barnes 2020](#)) clusters. The gold star represents TOI-1683.

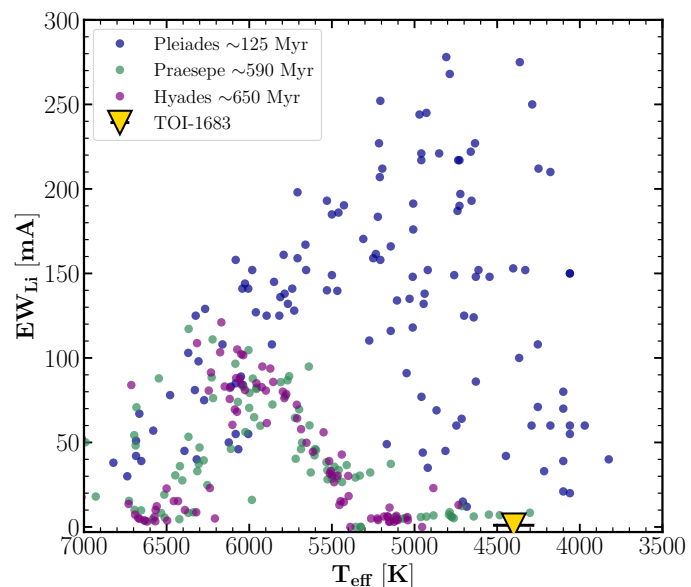


Fig. K.4: Equivalent width distribution of Li I as a function of the effective temperature for the Pleiades (~ 125 Myr; [Bouvier et al. 2018](#)), Praesepe (~ 590 Myr), and Hyades (~ 650 Myr; [Cummings et al. 2017](#)). The gold triangle represents TOI-1683.

is that they derived a rotation period of 11.3 ± 1.5 days, which is consistent with the half of the rotation period that we derived. Looking at a single TESS sector it is possible to confuse the stellar rotation period with one of its harmonics when it is of the order of the duration of the TESS sector (~ 28 days). This could be the case of TOI-1683 Sector 19. However, the consecutive Sectors 43 and 44 make it clear that the stellar rotation period of TOI-1683 is greater than 11.3 days.

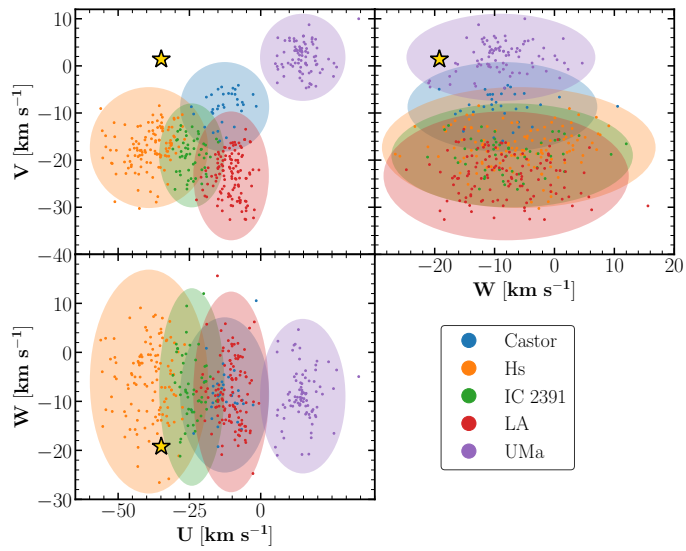


Fig. K.5: UVW velocity diagram for TOI-1683 (gold star). The members of the Castor moving group, Hyades supercluster (Hs), IC 2391 supercluster, Local Association (LA), and Ursa Major group (UMa) from Montes et al. (2001) are included. The ellipses represent the 3σ values of the UVW for each Young Moving Group.

Table L.1: Prior and posterior distributions from the nested sampling fitting for TOI-2018 b He I signal from the first night. Prior label \mathcal{U} represents uniform distribution.

| Parameter | Prior | Posterior |
|----------------------------------|-----------------------------|-------------------------|
| Absorption [%] | $\mathcal{U}(-3, 3)$ | $-1.10^{+0.26}_{-0.30}$ |
| λ_0 [Å] | $\mathcal{U}(10831, 10834)$ | 10833.61 ± 0.07 |
| σ [Å] | $\mathcal{U}(0, 1.5)$ | $0.24^{+0.07}_{-0.06}$ |
| Δv [km s ⁻¹] | – | 8.4 ± 1.9 |
| FWHM [Å] | – | $0.57^{+0.17}_{-0.15}$ |
| EW [mÅ] | – | $6.6^{+1.6}_{-1.5}$ |

Table L.2: Prior and posterior distributions from the nested sampling fitting for TOI-2018 b He I signal from the second night. Prior label \mathcal{U} represents uniform distribution.

| Parameter | Prior | Posterior |
|----------------------------------|-----------------------------|----------------------------|
| Absorption [%] | $\mathcal{U}(-3, 3)$ | $-1.15^{+0.33}_{-0.50}$ |
| λ_0 [Å] | $\mathcal{U}(10831, 10834)$ | $10833.21^{+0.14}_{-0.20}$ |
| σ [Å] | $\mathcal{U}(0, 1.5)$ | $0.50^{+0.30}_{-0.20}$ |
| Δv [km s ⁻¹] | – | $-0.2^{+4.0}_{-5.5}$ |
| FWHM [Å] | – | $1.20^{+0.65}_{-0.45}$ |
| EW [mÅ] | – | $14.7^{+4.9}_{-4.5}$ |

Appendix L: TOI-2018 b extra material

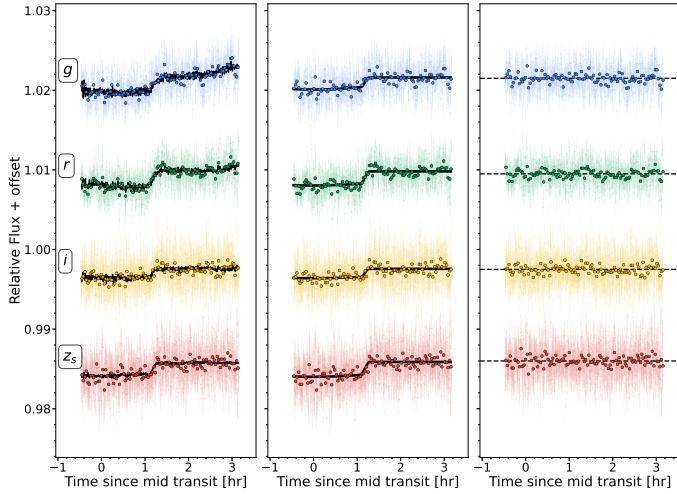


Fig. L.1: MuSCAT2 ground-based transit observation of TOI-2018 b. Raw light curve (left panel), detrended light curve (centre panel), and residuals (right panel) for the Sloan g (blue), r (green), i (yellow), z_s (red) filters. The points show the individual observations, the circles represent binned data points, and the best-fit model is shown by the black line.

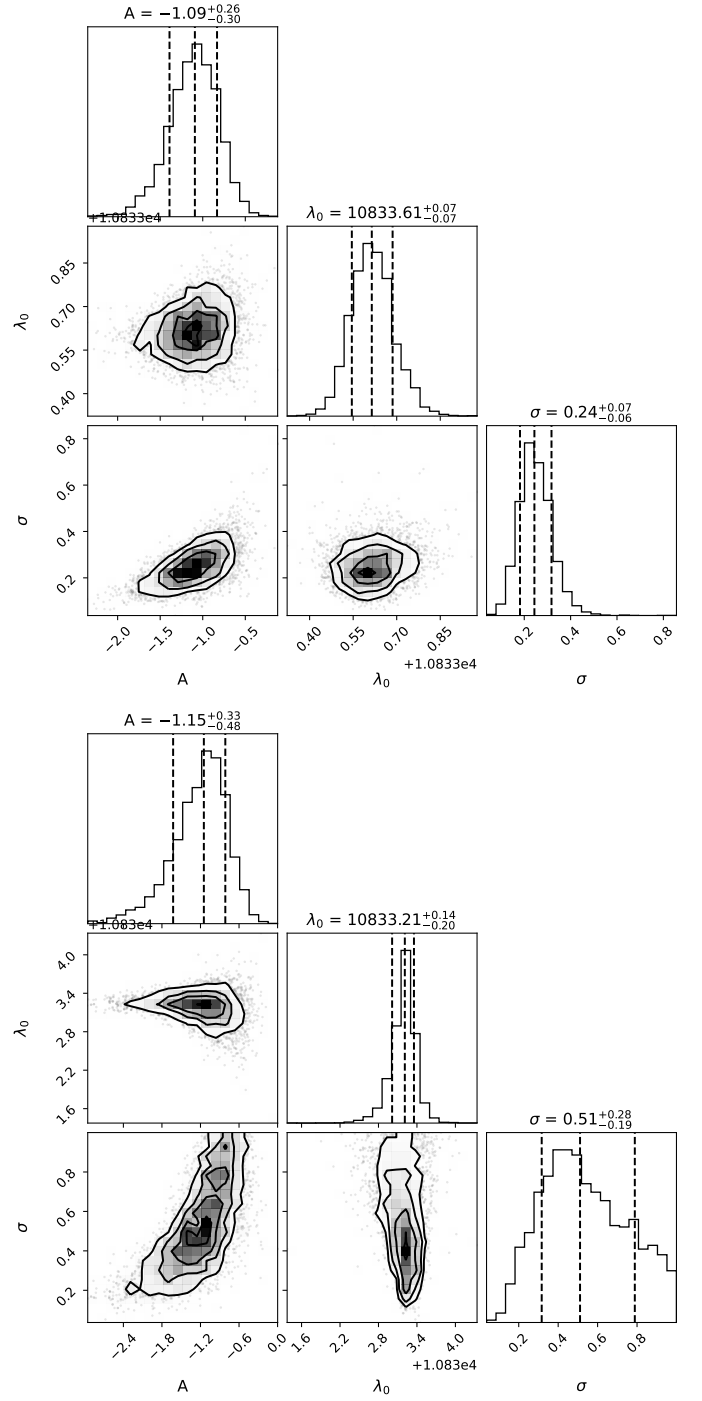


Fig. L.2: Corner plot for the nested sampling posterior distribution of TOI-2018 b He I signals for first (top) and second (bottom) nights.

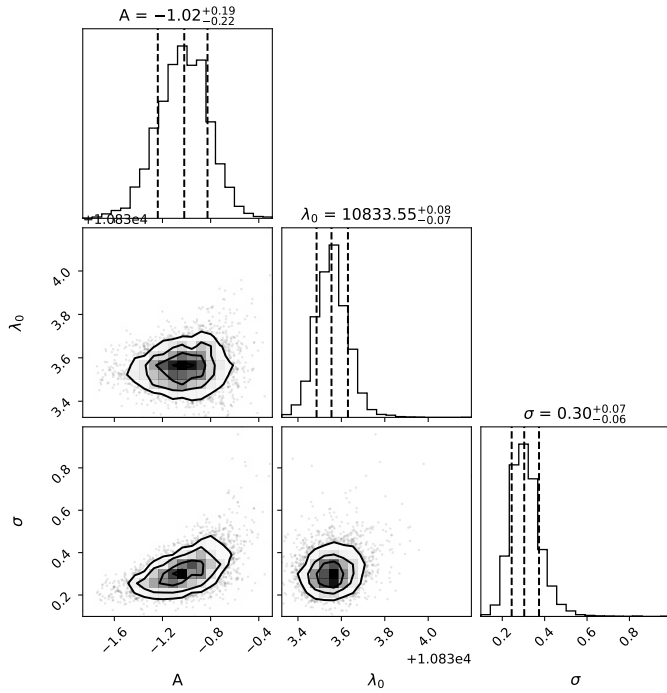


Fig. L.3: Corner plot for the nested sampling posterior distribution of TOI-2018 b He I signals from the combined nights.

Table L.3: Prior and posterior distributions from the nested sampling fitting for TOI-2018 b He I signal from the combined nights. Prior label \mathcal{U} represents uniform distribution.

| Parameter | Prior | Posterior |
|-----------------------------------|-----------------------------|----------------------------|
| Absorption [%] | $\mathcal{U}(-3, 3)$ | $-1.02^{+0.19}_{-0.22}$ |
| λ_0 [\AA] | $\mathcal{U}(10831, 10834)$ | $10833.55^{+0.08}_{-0.07}$ |
| σ [\AA] | $\mathcal{U}(0, 1.5)$ | $0.30^{+0.07}_{-0.06}$ |
| Δv [km s^{-1}] | – | $6.8^{+2.1}_{-1.9}$ |
| FWHM [\AA] | – | $0.71^{+0.17}_{-0.14}$ |
| EW [m\AA] | – | 7.8 ± 1.5 |

Appendix M: He I database information

As Zhang et al. (2023a) remarked, the compilation of consistent parameters and study the He I triplet is a challenging work. We thank the effort done by Zhang et al. (2023a) to construct Table 3 therein. We based our He I database (Table M.1) on the compilations by Kirk et al. (2022), Czesla et al. (2022), Fossati et al. (2022, 2023), Guilluy et al. (2023), Zhang et al. (2023a), and J. Sanz-Forcada, priv. comm., which we further complemented.

Because the He I results are given in terms of the equivalent width (EW) or absorption peak of the line, we firstly needed a relation between both magnitudes to convert one to the other. The EW for a spectral line is the width of a rectangle, with a height of the continuum level, such that the area of the spectral line is equal to the area of the rectangle. Usually, the planetary spectral lines are fitted using a Gaussian profile as $G(\lambda) = A \exp(-(\lambda - \lambda_0)^2 / (2\sigma^2))$ where A is the amplitude of the signal, λ_0 is the central position of the line, and σ is the standard deviation. Thus, the area under the curve described by $G(\lambda)$ can be computed as

$$\int_{-\infty}^{+\infty} G(\lambda) d\lambda = A \sqrt{2\pi\sigma^2} \quad (\text{M.1})$$

If the spectra are normalised to 1, we can calculate $\text{EW} = |A| \sqrt{2\pi\sigma^2}$, where A is in units of normalised flux. EW is in the units of σ . Then, we calculated from the papers where EW and absorption values are reported (e.g. Guilluy et al. 2020; Casasayas-Barris et al. 2021a; Zhang et al. 2022b, 2023b; Orell-Miquel et al. 2022, 2023) a master- σ as the mean value. We obtained master- $\sigma = 0.43 \text{ m\AA}$.

Table M.1: Exoplanet database of He I observation by means of high-resolution spectroscopy from this work and the literature (possibly incomplete). We complemented the planets inspected for He I with information about H α and/or Ly α studies (H flag column). F_{XUV} wavelength range is $\lambda = 5\text{--}504 \text{ \AA}$.

| Planet | P [d] | R_p [R_{\oplus}] | M_p [M_{\oplus}] | T_{eq} [K] | Age [Gyr] | M_* [M_{\odot}] | R_* [R_{\odot}] | T_{eff} [K] | H flag ^a | He I flag ^a | D_{He} [%] | EW_{He} [mÅ] | F_{XUV}^b [W m^{-2}] |
|-------------|---------|----------------------------|--------------------------|---------------------|-------------------------|-----------------------|-----------------------|-----------------------|---------------------|------------------------|------------------------|------------------------|--|
| 55 Cnc e | 0.7365 | 1.875 \pm 0.029 | 7.99 $^{+0.32}_{-0.33}$ | 1958 \pm 15 | 10.2 \pm 2.5 | 0.905 \pm 0.015 | 0.943 \pm 0.01 | 5172 \pm 18 | – | ND | <0.025 | <0.27 | 4.57 ¹ |
| AU Mic b | 8.463 | 4.16 \pm 0.18 | 11.7 \pm 5.0 | 593 \pm 21 | 0.022 \pm 0.003 | 0.5 \pm 0.03 | 0.75 \pm 0.03 | 3700 \pm 100 | – | ND | <0.34 | <3.7 | 22.9 ¹ |
| GJ436 b | 2.6441 | 4.19 \pm 0.1 | 23.14 \pm 0.76 | 686 \pm 10 | 6.0 $^{+4.0}_{-3.0}$ | 0.445 \pm 0.044 | 0.449 \pm 0.019 | 3479 \pm 60 | Y ^L | ND | <0.41 | <1.45 | 0.145 ¹ |
| GJ806 b | 0.9263 | 1.331 \pm 0.023 | 1.9 \pm 0.17 | 940 \pm 10 | 4.0 $^{+4.0}_{-3.0}$ | 0.413 \pm 0.011 | 0.4144 \pm 0.0038 | 3600 \pm 16 | ND ^H | ND | <0.7 | <7.4 | 1.62 ¹ |
| GJ1214 b | 1.5804 | 2.742 $^{+0.05}_{-0.053}$ | 8.17 \pm 0.43 | 596 \pm 19 | 3.0 $^{+7.0}_{-0.0}$ | 0.178 \pm 0.01 | 0.215 \pm 0.008 | 3250 \pm 100 | – | ND | <2.1 $^{+0.45}_{-0.5}$ | <28.9 $^{+9.4}_{-8.5}$ | 0.2951 ¹ |
| GJ3470 b | 3.3366 | 4.04 \pm 0.11 | 11.44 \pm 0.64 | 733 \pm 23 | 1.65 \pm 1.4 | 0.476 \pm 0.019 | 0.474 \pm 0.014 | 3725 \pm 54 | Y ^L | Y | 1.5 \pm 0.3 | 20.72 \pm 1.3 | 1.44 ² |
| GJ9827 b | 1.209 | 1.529 \pm 0.058 | 4.87 \pm 0.37 | 1114 $^{+44}_{-26}$ | 10.0 $^{+3.0}_{-5.0}$ | 0.593 \pm 0.018 | 0.579 \pm 0.018 | 4294 \pm 52 | ND ^B | ND | <0.21 | <1.86 | 0.72 ¹ |
| GJ9827 d | 6.2018 | 1.955 \pm 0.075 | 3.42 \pm 0.62 | 646 $^{+26}_{-15}$ | 10.0 $^{+3.0}_{-5.0}$ | 0.593 \pm 0.018 | 0.579 \pm 0.018 | 4294 \pm 52 | ND ^B | ND | <0.3 | <1.24 | 0.081 ¹ |
| HD63433 b | 7.1079 | 2.141 $^{+0.09}_{-0.067}$ | 5.5 \pm 2.3 | 967 $^{+19}_{-16}$ | 0.414 \pm 0.023 | 0.956 \pm 0.022 | 0.934 \pm 0.029 | 5553 \pm 56 | ND ^B | ND | <0.34 | <2.0 | 10.3 ³ |
| HD63433 c | 20.5438 | 2.69 $^{+0.11}_{-0.09}$ | 15.5 $^{+3.9}_{-3.8}$ | 679 $^{+13}_{-11}$ | 0.414 \pm 0.023 | 0.956 \pm 0.022 | 0.934 \pm 0.029 | 5553 \pm 56 | Y ^L | ND | <0.4 | <4.2 | 2.5 ³ |
| HD73583 b | 6.398 | 2.79 \pm 0.1 | 10.2 $^{+3.4}_{-3.1}$ | 721 \pm 21 | 0.49 \pm 0.19 | 0.71 \pm 0.02 | 0.66 \pm 0.02 | 4511 \pm 110 | ND ^H | Y | 0.72 \pm 0.08 | 8.6 \pm 0.6 | 3.1 ³ |
| HD73583 c | 18.8797 | 2.39 \pm 0.1 | 9.7 $^{+1.8}_{-1.7}$ | 503 \pm 15 | 0.49 \pm 0.19 | 0.71 \pm 0.02 | 0.66 \pm 0.02 | 4511 \pm 110 | ND ^H | ND | <0.5 | <5.3 | 0.7 ³ |
| HD89345 b | 11.8144 | 6.86 \pm 0.14 | 35.6 \pm 3.2 | 1053 \pm 14 | 9.4 $^{+0.4}_{-1.3}$ | 1.12 \pm 0.04 | 1.657 \pm 0.02 | 5499 \pm 73 | – | NC | <0.7 | <7.4 | 0.244 ⁴ |
| HD97658 b | 9.4893 | 2.247 $^{+0.098}_{-0.095}$ | 7.55 $^{+0.83}_{-0.79}$ | 757 $^{+12}_{-13}$ | 6.0 \pm 1.0 | 0.77 \pm 0.05 | 0.741 \pm 0.024 | 5170 \pm 50 | – | ND | <0.21 | <0.9 | 0.128 ¹ |
| HD189733 b | 2.2186 | 12.76 \pm 0.3 | 357.0 \pm 14.0 | 1200 \pm 20 | 6.8 \pm 5.2 | 0.806 \pm 0.048 | 0.756 \pm 0.018 | 5040 \pm 50 | Y ^B | Y | 0.75 \pm 0.03 | 12.76 \pm 0.4 | 16.75 ⁵ |
| HD209458 b | 3.5247 | 15.23 $^{+0.16}_{-0.21}$ | 217.7 $^{+4.8}_{-4.4}$ | 1449 \pm 12 | 4.0 \pm 2.0 | 1.119 \pm 0.033 | 1.155 \pm 0.015 | 6065 \pm 50 | Y ^B | Y | 0.91 \pm 0.1 | 5.252 \pm 0.5 | 1.004 ⁶ |
| HD235088 b | 7.4341 | 2.045 \pm 0.075 | 7.0 \pm 2.0 | 805 $^{+13}_{-12}$ | 0.65 $^{+0.15}_{-0.05}$ | 0.843 \pm 0.05 | 0.789 \pm 0.021 | 5037 \pm 14 | – | Y | 0.91 $^{+0.11}_{-0.1}$ | 9.5 $^{+1.1}_{-1.0}$ | 1.854 ⁷ |
| HAT-P-3 b | 2.8997 | 10.2 \pm 0.4 | 189.1 \pm 7.6 | 1170 \pm 17 | 2.9 $^{+4.9}_{-2.7}$ | 0.925 \pm 0.046 | 0.85 \pm 0.021 | 5190 \pm 80 | – | ND | <1.9 | <20.2 | 7.968 ⁴ |
| HAT-P-11 b | 4.8878 | 4.36 \pm 0.06 | 27.7 \pm 3.1 | 832 \pm 10 | 6.5 $^{+5.9}_{-4.1}$ | 0.802 \pm 0.028 | 0.683 \pm 0.009 | 4780 \pm 50 | Y ^L | Y | 1.08 \pm 0.05 | 12.4 \pm 2.4 | 2.109 ⁸ |
| HAT-P-18 b | 5.508 | 11.15 \pm 0.58 | 62.6 \pm 4.1 | 852 \pm 28 | 12.4 $^{+1.4}_{-6.4}$ | 0.77 \pm 0.031 | 0.749 \pm 0.037 | 4803 \pm 80 | – | Y | 0.7 \pm 0.16 | 29.21 \pm 1.0 | 0.7 ⁹ |
| HAT-P-32 b | 2.15 | 20.05 \pm 0.28 | 185.9 \pm 9.9 | 1786 \pm 26 | 2.7 \pm 0.8 | 1.16 \pm 0.041 | 1.219 \pm 0.016 | 6269 \pm 64 | Y ^H | Y | 5.3 \pm 0.1 | 114.0 \pm 4.0 | 163.0 ¹⁰ |
| HAT-P-33 b | 3.4745 | 18.9 \pm 0.5 | 229.0 $^{+41.0}_{-38.0}$ | 1782 \pm 28 | 2.3 \pm 0.3 | 1.42 \pm 0.15 | 1.91 \pm 0.26 | 6460 $^{+300}_{-290}$ | – | ND | <1.4 | <14.9 | 6.195 ⁴ |
| HAT-P-49 b | 2.6916 | 15.84 $^{+1.4}_{-0.86}$ | 550.0 \pm 65.0 | 2131 $^{+69}_{-42}$ | 1.5 \pm 0.2 | 1.543 \pm 0.051 | 1.833 \pm 0.138 | 6820 \pm 52 | – | ND | <0.6 | <6.4 | 14.51 ⁴ |
| HAT-P-57 b | 2.4653 | 15.84 \pm 0.61 | <590 | 2200 \pm 26 | 1.0 $^{+0.67}_{-0.51}$ | 1.47 \pm 0.12 | 1.5 \pm 0.05 | 7500 \pm 250 | NC ^H | NC | <1.0 | <10.6 | – |
| HAT-P-67 b | 4.8101 | 23.37 $^{+1.1}_{-0.8}$ | 108.0 $^{+79.0}_{-60.0}$ | 1903 \pm 35 | 1.24 $^{+0.24}_{-0.22}$ | 1.642 \pm 0.1 | 2.65 \pm 0.12 | 6406 $^{+65}_{-61}$ | NC ^L | Y | 10.0 \pm 0.1 | 140.0 \pm 10.0 | – |
| HAT-P-70 b | 2.7443 | 21.0 $^{+1.7}_{-1.1}$ | <2155 | 2562 \pm 50 | 0.60 $^{+0.38}_{-0.2}$ | 1.890 \pm 0.013 | 1.86 \pm 0.12 | 8450 \pm 540 | Y ^H | – | – | – | – |
| LTT9779 b | 0.7920 | 4.72 \pm 0.23 | 28.32 $^{+0.78}_{-0.81}$ | 1978 \pm 19 | 2 $^{+1.3}_{-0.9}$ | 1.02 \pm 0.03 | 0.949 \pm 0.006 | 5443 \pm 14 | – | ND | <0.2 | <3.79 | 4.8 ¹⁵ |
| MASCARA-2 b | 3.4741 | 20.51 \pm 0.78 | <1075 | 2262 \pm 73 | 0.2 $^{+0.1}_{-0.05}$ | 1.89 \pm 0.06 | 1.6 \pm 0.06 | 8980 $^{+90}_{-130}$ | Y ^H | ND | <0.5 | <5.3 | – |

Table M.1: continued.

| Planet | P [d] | R_p [R_\oplus] | M_p [M_\oplus] | T_{eq} [K] | Age [Gyr] | M_* [M_\odot] | R_* [R_\odot] | T_{eff} [K] | H flag ^a | He I flag ^a | D_{He} [%] | EW_{He} [mÅ] | F_{XUV}^b [W m^{-2}] |
|--------------|----------|---------------------------|-------------------------|------------------------|------------------------|------------------------|------------------------|-------------------------|------------------------|---------------------------|-------------------------|--------------------------|---|
| TOI-1136 d | 12.5194 | $4.626^{+0.076}_{-0.072}$ | $8.0^{+2.4}_{-1.9}$ | 840±12 | 0.7±0.15 | 1.022±0.027 | 0.968±0.036 | 5770±50 | Y ^H | ND | <0.5 | <5.4 | – |
| TOI-1235 b | 3.4447 | $1.694^{+0.088}_{-0.077}$ | $5.9^{+0.62}_{-0.61}$ | 775^{+14}_{-13} | $5.0^{+5.0}_{-4.4}$ | 0.63 ± 0.024 | 0.619 ± 0.019 | 3997±51 | – | ND | <0.09 | <1.44 | – |
| TOI-1268 b | 8.1577 | 9.1±0.6 | 96.0±13.0 | 919±30 | 0.245±0.14 | 0.96±0.04 | 0.92±0.06 | 5300±100 | – | Y | $1.97^{+0.16}_{-0.15}$ | $19.1^{+1.9}_{-1.8}$ | 7.2 ¹ |
| TOI-1431 b | 2.6502 | 16.7 ± 0.56 | 992.0 ± 57.0 | 2370±70 | $0.29^{+0.32}_{-0.19}$ | 1.895 ± 0.1 | 1.923 ± 0.068 | 7690^{+600}_{-250} | ND ^H | ND | <0.4 | <4.2 | – |
| TOI-1683 b | 3.0575 | 2.3±0.3 | 8.0±3.0 | 927±35 | $2.0^{+1.3}_{-0.9}$ | 0.69±0.09 | 0.636±0.03 | 4539±100 | – | Y | 0.84±0.17 | 8.5±1.6 | 7.4 ³ |
| TOI-1728 b | 3.4914 | 4.62 ± 0.09 | $26.8^{+5.4}_{-5.1}$ | 757^{+16}_{-15} | 7.1±4.6 | 0.646 ± 0.023 | 0.6243 ± 0.01 | 3980^{+31}_{-32} | – | ND | <1.1 | <11.7 | – |
| TOI-1807 b | 0.5494 | 1.37 ± 0.09 | 2.57 ± 0.5 | 2100^{+39}_{-40} | 0.3±0.08 | 0.75 ± 0.025 | 0.68 ± 0.015 | 4757^{+51}_{-50} | ND ^H | ND | <0.38 | <4.0 | 3.05 ¹ |
| TOI-2018 b | 7.4356 | 2.268 ± 0.069 | 9.2 ± 2.1 | 642±12 | $2.4^{+0.2}_{-0.8}$ | 0.57 ± 0.02 | 0.62 ± 0.01 | 4174^{+34}_{-42} | NC ^H | Y | $1.02^{+0.19}_{-0.22}$ | 7.8 ± 1.5 | 1.56 ¹ |
| TOI-2046 b | 1.4972 | 16.1±1.2 | 731.0±89.0 | 2000±55 | $0.4^{+0.22}_{-0.3}$ | 1.13±0.19 | 1.21±0.07 | 6200±100 | NC ^H | NC | <2.9 | <30.5 | 22.45 ¹ |
| TOI-2048 b | 13.7905 | 2.6±0.2 | 9.0±3.0 | 675^{+22}_{-16} | 0.3±0.05 | 0.83±0.03 | 0.79±0.04 | 5185±60 | NC ^H | NC | <1.0 | <10.2 | – |
| TOI-2076 b | 10.3557 | 2.52 ± 0.056 | 9.0±3.0 | 800±13 | 0.34±0.08 | 0.824 ± 0.036 | 0.77 ± 0.006 | 5200±70 | ND ^H | Y | 1.01±0.05 | 10.0±0.7 | 6.7 ³ |
| TOI-2134 b | 9.2292 | 2.69 ± 0.16 | $9.13^{+0.78}_{-0.76}$ | 666±8 | $3.8^{+5.5}_{-2.7}$ | 0.744 ± 0.027 | 0.709±0.017 | 4580±54 | – | Y | 0.38±0.05 | 3.3±0.3 | 0.46 ³ |
| TOI-2136 b | 7.8519 | 2.2±0.07 | $4.7^{+3.1}_{-2.6}$ | 378±13 | 4.6±1.0 | 0.3272 ± 0.0082 | 0.344 ± 0.0099 | 3373±108 | – | ND | <1.44 | <7.8 | – |
| TOI-3757 b | 3.4388 | $12.0^{+0.4}_{-0.5}$ | $85.3^{+8.8}_{-8.7}$ | 759±13 | 7.1±4.5 | 0.64 ± 0.02 | 0.62 ± 0.01 | 3913±56 | – | NC | <6.9 | <73.0 | – |
| TRAPPIST-1 b | 1.5109 | 1.086 ± 0.035 | 0.85 ± 0.072 | 400±7 | 7.6±2.2 | 0.0802 ± 0.0073 | 0.117 ± 0.0036 | 2550±50 | – | ND | <0.33 | <3.467 | 0.7244 ¹ |
| TRAPPIST-1 e | 6.0996 | 0.918 ± 0.039 | 0.62 ± 0.058 | 251±4 | 7.6±2.2 | 0.0802 ± 0.0073 | 0.117 ± 0.0036 | 2550±50 | – | ND | <1.07 | <10.458 | 0.112 ¹ |
| TRAPPIST-1 f | 9.2067 | 1.045 ± 0.038 | 0.68 ± 0.18 | 219±4 | 7.6±2.2 | 0.0802 ± 0.0073 | 0.117 ± 0.0036 | 2550±50 | – | ND | <0.38 | <4.143 | 0.0645 ¹ |
| NGTS-5 b | 3.357 | 12.73 ± 0.26 | 73.0 ± 12.0 | 952±24 | $5.0^{+8.0}_{-3.5}$ | 0.661 ± 0.065 | 0.739 ± 0.014 | 4987±41 | – | ND | $<1.02^{+0.48}_{-0.46}$ | $<10.8^{+5.1}_{-4.9}$ | 3.2 ⁹ |
| K2-25 b | 3.4846 | 3.43 ± 0.12 | $28.5^{+8.5}_{-8.3}$ | 345^{+8}_{-7} | 0.725 ± 0.075 | 0.294 ± 0.021 | 0.295 ± 0.02 | 3180±60 | ND ^L | ND | <1.7 | <17.0 | – |
| K2-77 b | 8.1998 | 2.3±0.16 | <600 | 770±30 | $0.12^{+0.78}_{-0.02}$ | 0.8±0.12 | 0.76±0.03 | 4970±45 | NC ^H | NC | <2.7 | <28.0 | 13.45 ¹ |
| K2-100 b | 1.6739 | 3.88 ± 0.16 | 21.8 ± 6.2 | 1841±41 | 0.7±0.1 | 1.15±0.05 | 1.24±0.05 | 5945±110 | ND ^H | ND | <1.3 | <5.7 | 141.253 ¹ |
| K2-105 b | 8.267 | $3.59^{+0.11}_{-0.07}$ | 30.0 ± 19.0 | 814±12 | $5.0^{+8.0}_{-4.4}$ | 1.05 ± 0.02 | 0.97 ± 0.01 | 5636^{+49}_{-52} | – | NC | <2.33 | <24.7 | 14.69 ⁴ |
| K2-136 c | 17.307 | 3.0±0.13 | $18.1^{+1.8}_{-1.9}$ | 425^{+10}_{-33} | 0.65 ± 0.07 | 0.742 ± 0.02 | 0.677 ± 0.027 | 4500±50 | – | NC | <2.3 | <25.0 | 0.5888 ¹ |
| KELT-9 b | 1.4811 | 21.701 ± 0.053 | 920.0 ± 110.0 | 3900^{+182}_{-174} | $0.45^{+0.14}_{-0.13}$ | 2.32 ± 0.16 | 2.418 ± 0.058 | 9600±400 | Y ^H | ND | <0.33 | <1.17 | 0.15 ⁵ |
| Kepler-25 c | 12.7204 | $5.217^{+0.07}_{-0.065}$ | $15.2^{+1.3}_{-1.6}$ | 992±8 | 2.75±0.3 | 1.26±0.03 | 1.34±0.01 | 6354±27 | – | NC | <1.86 | <19.8 | 1.019 ⁴ |
| Kepler-68 b | 5.3988 | $2.31^{+0.06}_{-0.09}$ | $8.3^{+2.2}_{-2.4}$ | 1280±90 | 6.3±1.7 | 1.079 ± 0.051 | 1.243 ± 0.019 | 5793±74 | – | NC | <0.72 | <7.6 | 1.176 ⁴ |
| V1298Tau c | 8.2489 | 5.2±0.39 | <76 | 968±31 | 0.023 ± 0.004 | 1.17 ± 0.06 | 1.278 ± 0.07 | 5050±100 | NC ^H | NC | <3.75 | <95.8 | 151.356 ¹ |
| V1298Tau b | 24.1399 | 9.77±0.65 | 203.0 ± 60.0 | 677±22 | 0.023 ± 0.004 | 1.17 ± 0.06 | 1.278 ± 0.07 | 5050±100 | – | NC | <1.7 | <19.0 | 87.09 ¹ |
| WASP-11 b | 3.7225 | 11.1 ± 0.25 | 156.0 ± 8.0 | 992±14 | $7.6^{+6.0}_{-3.5}$ | 0.81 ± 0.04 | 0.772 ± 0.015 | 4900±65 | – | NC | <1.56 | <16.6 | 1.9 ¹¹ |

Table M.1.: continued.

| Planet | P | R_p [R_\oplus] | M_p [M_\oplus] | T_{eq} [K] | Age [Gyr] | M_* [M_\odot] | R_* [R_\odot] | T_{eff} [K] | H flag ^a | He I flag ^a | D_{He} [%] | EW_{He} [mÅ] | F_{XUV}^b [$W m^{-2}$] |
|------------|--------|---|---|------------------------------------|-------------------------------------|------------------------|------------------------|--------------------------------------|------------------------|---------------------------|-----------------|-------------------|-------------------------------|
| WASP-12 b | 1.0914 | 21.71±0.63 | 466.0±25.0 | 2592±57 | 2.0 ^{+0.8} _{-1.0} | 1.434±0.11 | 1.657±0.046 | 6300 ⁺²⁰⁰ ₋₁₀₀ | Y ^H | ND | <0.5 | <5.3 | 3.18 ¹² |
| WASP-39 b | 4.0553 | 14.34±0.45 | 89.0±10.0 | 1166±14 | 8.5 ^{+4.0} _{-3.4} | 0.913±0.047 | 0.939±0.022 | 5485±50 | – | NC | <2.04 | <21.7 | 1.2 ¹¹ |
| WASP-47 d | 9.0305 | 3.567±0.045 | 14.2±1.3 | 919±13 | 6.5 ^{+2.6} _{-1.2} | 1.04±0.031 | 1.137±0.013 | 5552±75 | – | NC | <3.29 | <34.9 | 0.577 ⁴ |
| WASP-48 b | 2.1436 | 18.7±1.1 | 328.0 ^{+15.0} _{-14.0} | 2035±52 | 7.9 ^{+2.0} _{-1.6} | 1.19±0.05 | 1.75±0.09 | 6000±150 | – | ND | <0.25±0.21 | <2.7±2.2 | – |
| WASP-52 b | 1.7498 | 14.04±0.3 | 137.9±7.6 | 1315±26 | 0.4 ^{+0.3} _{-0.2} | 0.804±0.05 | 0.786±0.016 | 5000±100 | Y ^H | Y | 3.44±0.31 | 39.583±1.4 | 24.8 ¹³ |
| WASP-69 b | 3.8681 | 11.85±0.53 | 82.6±5.4 | 963±18 | 2.0±0.5 | 0.826±0.029 | 0.813±0.028 | 4700±50 | NC ^H | Y | 3.59±0.19 | 28.31±0.9 | 4.17 ⁵ |
| WASP-76 b | 1.8099 | 20.78 ^{+0.86} _{-0.85} | 284.1 ^{+4.4} _{-4.1} | 2160±40 | 5.3 ^{+6.1} _{-2.9} | 1.458±0.021 | 1.756±0.071 | 6329±25 | Y ^H | ND | <0.88 | <1.7 | 112.2018 ¹ |
| WASP-77 b | 1.36 | 13.79 ^{+0.35} _{-0.33} | 530.0 ^{+22.0} _{-20.0} | 1715 ⁺²⁶ ₋₂₅ | 6.2 ^{+4.0} _{-3.5} | 0.903±0.06 | 0.91±0.025 | 5617±72 | ND ^H | ND | <0.8 | <8.4 | 13.182 ¹ |
| WASP-80 b | 3.0679 | 11.2 ^{+0.35} _{-0.34} | 171.0±11.0 | 825±19 | ≤0.2 | 0.577±0.05 | 0.586±0.018 | 4143 ⁺⁹² ₋₉₄ | – | ND | <0.85 | <2.48 | 1.6595 ¹ |
| WASP-107 b | 5.7215 | 10.54±0.22 | 35.0±3.2 | 770±60 | 8.3±4.3 | 0.69±0.05 | 0.66±0.02 | 4430±120 | – | Y | 7.26±0.24 | 87.152±7.6 | 2.664 ¹ |
| WASP-127 b | 4.1781 | 15.36±0.45 | 57.2±6.4 | 1400±24 | 11.41±1.8 | 1.08±0.03 | 1.39±0.03 | 5620±85 | ND ^H | ND | <0.48 | <6.8 | 0.058 ¹⁴ |
| WASP-177 b | 3.0717 | 17.7 ^{+7.4} _{-4.0} | 161.0±12.0 | 1142±32 | 9.7±3.9 | 0.876±0.038 | 0.885±0.046 | 5017±70 | – | ND | <1.28±0.30 | <6.8±1.6 | 3.5 ¹³ |
| WASP-189 b | 2.724 | 18.15±0.24 | 632.0 ^{+60.0} _{-44.0} | 2641±34 | 0.75±0.13 | 2.03±0.066 | 2.36±0.03 | 8000±80 | NC ^H | ND | <0.3 | <3.2 | – |

Notes. ^a Y: Detection, ND: Non Detection, NC: Non Conclusive, For H, we indicate if the detection/non-detection comes from H α (H), Ly α (L), or both (B). ^b F_{XUV} from: ¹ Sanz-Forcada in prep., ² Palle et al. (2020a), ³ Zhang et al. (2023a), ⁴ Guilluy et al. (2023), ⁵ Nortmann et al. (2018), ⁶ Alonso-Floriano et al. (2019), ⁷ Orell-Miquel et al. (2023), ⁸ Allart et al. (2018), ⁹ Vissapragada et al. (2022b), ¹⁰ Czesla et al. (2022), ¹¹ Allart et al. (2022), ¹² Czesla et al. (2024), ¹³ Kirk et al. (2024), ¹⁴ dos Santos et al. (2020), and ¹⁵ Vissapragada et al. (2024b)

References. Data compilation from NASA Exoplanet Archive and ExoAtmospheres database. Some references in particular are as follows. 55 Cnc e: von Braun et al. (2011); Zhang et al. (2021); AU Mic b: Playchan et al. (2020); Zicher et al. (2022); Palle et al. (2020); Hranro et al. (2020); Rockcliffe et al. (2023); GJ436 b: Nortmann et al. (2018); Cauley et al. (2017); Kulow et al. (2014); Ehrenreich et al. (2015); GJ806 b: Palle et al. (2023); GJ1214 b: Kasper et al. (2020); Orell-Miquel et al. (2022); Spake et al. (2023); GJ3470 b: Bourrier et al. (2018); Palle et al. (2020a); Ninan et al. (2020); GJ9827 b: Krishnamurthy et al. (2023); Carleo et al. (2021); Kasper et al. (2020); HD63433 b: Mann et al. (2020); Mallorquin et al. (2023); Zhang et al. (2022c); HD63433 c: Mann et al. (2020); Mallorquin et al. (2022c); Zhang et al. (2022); Barragán et al. (2022); Zhang et al. (2022b, 2023b); HD73583 c: Barragán et al. (2022); HD89345 b: Guilluy et al. (2023); HD97658 b: Kasper et al. (2020); HD189733 b: Jensen et al. (2012); Salz et al. (2018); Guilluy et al. (2020); Zhang et al. (2022a); Allart et al. (2023); Dos Santos et al. (2023); HD209458 b: Vidal-Madjar et al. (2003); Alonso-Floriano et al. (2019); HD235088 b: Orell-Miquel et al. (2023); HAT-P-3 b: Guilluy et al. (2023); HAT-P-11 b: Allart et al. (2018); Ben-Jaffel et al. (2022); Allart et al. (2023); Fu et al. (2022); Fourmier-Tondreau et al. (2024); HAT-P-32 b: Czesla et al. (2022); Zhang et al. (2023c); HAT-P-33 b: Guilluy et al. (2023); HAT-P-49 b: Guilluy et al. (2023); HAT-P-57 b: Hartman et al. (2015); Stangret et al. (2022); HAT-P-67 b: Bello-Arufe et al. (2023); Gully-Santiago et al. (2024); HAT-P-70 b: Bello-Arufe et al. (2022); LTT9779 b: Jenkins et al. (2020); Vissapragada et al. (2024b); MASCARA-2 b: Lund et al. (2017); Talens et al. (2018); Casasayas-Barris et al. (2019); TOI-1136 d: Dai et al. (2023a); TOI-1235 b: Krishnamurthy et al. (2020); TOI-1268 b: Šubjak et al. (2022); TOI-1431 b: Addison et al. (2021); Stangret et al. (2022); TOI-1683 b: Zhang et al. (2023b); TOI-1728 b: Kanodia et al. (2020); TOI-1807 b: Nardiello et al. (2022); Gaidos et al. (2023); TOI-2018 b: Dai et al. (2023b); TOI-2046 b: Kabáth et al. (2022); TOI-2048 b: Newton et al. (2022); TOI-2076 b: Osborn et al. (2022); Zhang et al. (2023b); Gaidos et al. (2023); TOI-2134 b: Zhang et al. (2023a); TOI-2136 b: Kawachi et al. (2022); TOI-3757 b: Kanodia et al. (2022); TRAPPIST-1 b: Gillon et al. (2017); Krishnamurthy et al. (2021); TRAPPIST-1 e: Gillon et al. (2017); Krishnamurthy et al. (2021); TRAPPIST-1 f: Gillon et al. (2017); Krishnamurthy et al. (2021); NGTS-5 b: Vissapragada et al. (2022b); K2-25 b: Mann et al. (2016); Gaidos et al. (2020b); Rockcliffe et al. (2021); K2-77 b: Gaidos et al. (2017); K2-100 b: Stefanson et al. (2018); Barragán et al. (2019); Gaidos et al. (2020a); K2-105 b: Guilluy et al. (2023); K2-136 c: Mann et al. (2018); Gaidos et al. (2021); Mayo et al. (2023); KELT-9 b: Yan & Henning (2018); Nortmann et al. (2018); Kepler-25 c: Guilluy et al. (2023); Kepler-68 b: Guilluy et al. (2023); V1298Tau c: David et al. (2019); Suárez Mascareño et al. (2021); Feinstein et al. (2021); Vissapragada et al. (2021); Schlawin et al. (2022); V1298Tau b: David et al. (2019); Suárez Mascareño et al. (2021); Vissapragada et al. (2021); Gaidos et al. (2022); WASP-11 b: Allart et al. (2023); WASP-12 b: Jensen et al. (2018); Kreidberg & Oklopčić (2018); Czesla et al. (2024); WASP-39 b: Allart et al. (2023); WASP-47 d: Guilluy et al. (2023); WASP-48 b: Bennett et al. (2023); WASP-52 b: Chen et al. (2020); Kirk et al. (2020); Vissapragada et al. (2020); WASP-69 b: Nortmann et al. (2018); WASP-76 b: West et al. (2016); Casasayas-Barris et al. (2021a); WASP-77 b: Cortés-Zuleta et al. (2020); Khalafinejad et al. in prep.; WASP-80 b: Salz et al. (2015); Fossati et al. (2022); WASP-107 b: Spake et al. (2018); Allart et al. (2019); Kirk et al. (2020); Spake et al. (2021); Hejazi et al. (2023); WASP-127 b: Lam et al. (2017); dos Santos et al. (2020); Allart et al. (2020, 2023); WASP-177 b: Turner et al. (2019); Kirk et al. (2022); Vissapragada et al. (2022b); WASP-189 b: Anderson et al. (2018); Lendl et al. (2020); Stangret et al. (2022).